First-principles phonon-spectral analysis and deformation response of MOFs: Boson Peak, Amorphization and Generalized Flexibility

A Thesis

Submitted For the Degree of

DOCTOR OF PHILOSOPHY

in the Faculty of Science

by

Meha Bhogra

THEORETICAL SCIENCES UNIT
JAWAHARLAL NEHRU CENTRE FOR ADVANCED SCIENTIFIC RESEARCH
Bangalore – 560 064

APRIL 2021

To my parents and my brother

DECLARATION

I hereby declare that the matter embodied in the thesis entitled "***First-principles* phonon-spectral analysis and deformation response of MOFs: Boson Peak, Amorphization and Generalized Flexibility**" is the result of investigations carried out by me at the Theoretical Sciences Unit, Jawaharlal Nehru Centre for Advanced Scientific Research, Bangalore, India under the supervision of Prof. Umesh V. Waghmare and that it has not been submitted elsewhere for the award of any degree or diploma.

In keeping with the general practice in reporting scientific observations, due acknowledgement has been made whenever the work described is based on the findings of other investigators.

Meha Bhogra

CERTIFICATE

I hereby certify that the matter embodied in this thesis entitled "***First-principles* phonon-spectral analysis and deformation response of MOFs: Boson Peak, Amorphization and Generalized Flexibility**" has been carried out by Ms. Meha Bhogra at the Theoretical Sciences Unit, Jawaharlal Nehru Centre for Advanced Scientific Research, Bangalore, India under my supervision and that it has not been submitted elsewhere for the award of any degree or diploma.

Prof. Umesh V. Waghmare
(Research Supervisor)

Acknowledgements

First and foremost, I would like to convey my deepest sense of gratitude towards my advisor, Prof. Umesh V. Waghmare, for his guidance and constant encouragement throughout the M.S. and Ph.D. duration, and for introducing me to a sound analytical outlook crucial for a career in research.

Through this section of my thesis, I take this opportunity to thank my collaborators, Prof. Anthony Cheetham, Prof. Andrew Goodwin, Prof. G. U. Kulkarni and Dr. Chaitali Sow for the insightful discussions and their guidance.

I would like thank Prof. Kavita Jain, Prof. Ramesh Hariharan and Prof. Ravi Kannan for the courses they offered during my Ph.D. duration, and Prof. Subir K. Das for the fruitful discussion on one of the projects.

I am obliged to the Centre for Computational Materials Science for providing the computational resources. Special thanks to Prof. Bala, Anoop and Suresh for all their co-operation.

It's my pleasure to thank my lab-mates, Anjali, Suchitra, Pawan, Lakshay, Narendra, Shashank, Koyendrila, Raagya, Arijit, Prasad, Meghna, Prashant and Anuja for technical and non-technical discussions.

I would like to thank my friends in JNC for the enjoyable times on-campus: Kiruthika, Anjali, Croor, Nishant, Prateek, Mahaan, Shazia, Saumya and Viveka. And a few off-campus friends who have been there with me all along: Ankita, Sneha, Trapti, Mariam, Aalo and Sarada.

It's been a pleasure knowing Aruna ma'am and Kruti. The times spent with them will always be cherished. I would like to thank them for their care and affection.

A special thanks to Dr. Archana for timely advice and support.

Lastly, I thank my parents and my brother for their eternal support, encouragement and freedom for pursuing a career of my interest.

Contents

List of Figures

List of Tables

Chapter 1

Introduction

Understanding the propagation of sound waves in three states of matter has attracted active research interests for more than a century now [7, 8]. With strengths of inter-atomic/molecular interacting forces varying in many orders of magnitude, energy-transfer in gas, liquid and solid medium subjected to pressure due to sound waves occurs *via* two different modes. Highly discordant atomic movements in gases allow absorption of sound waves at low-frequencies through large collisional excitations [9], while in solids, restrained motion of atoms result in vibratory oscillations [10, 11]. Depending on the viscosity of liquids, their response to sound waves may manifest as collisional or vibrational [12]. Collective vibrational excitations or quanta of vibrational energy are termed as phonons [11], viz. acoustic phonons that are linked with the elasticity, and optical phonons, emerging from *harmonious* conformity of atomic arrangements in a solid. Liquids transmit only longitudinal acoustic waves at low-frequencies in the long-wavelength limit, but *absorb* transverse acoustic waves since they lack rigidity [13].

A crystalline solid **C** in Eucledian space, a structure possessing long-range atomic positional order is a consequence of spontaneously broken continuous symmetries of macroscopic disordered state (liquid or gas), and belongs to a space group containing a discrete set of symmetry elements. The broken continuous symmetries manifest as branches of acoustic (one longitudinal and two transverse) phonons which exhibit vanishing energy (or frequency $\omega \to 0$) in the long-wavelength limit ($\vec{q} \to 0$). The three acoustic phonon branches show linear dispersion of frequency with wave-vector ($\omega \propto |q|$) at $\vec{q} \to 0$, and are the Nambu-Goldstone (NG) bosons [14,15]. Linear dispersion with a positive slope of transverse acoustic phonons is a characteristic feature of solids, and a vibrational signature of their elastic rigidity [16].

The symmetry of a crystal **C** is represented by its space group that contains discrete translational and rotational transformations under which **C** is invariant, and belongs to a crystallographic point-group $\mathbf{G} = \mathrm{Sym}(\mathbf{C})$. Atomic positions in **C** are identified by the site-symmetry groups ($\mathrm{S}_i's$) or Wyckoff symbols, which are subsets of **G**. Group-theoretical principles allow correlation of each site S_i to irreducible representations (irreps) of the group **G**. This enables decomposition of any set of atomic displacements (or an arbitrary elastic vibration) as a superposition of identifiable normal modes (collective excitations) of a primitive cell of the crystal **C** [17]. The correlation method is widely used to obtain the precise number of IR, Raman and hyper-Raman active modes, determining the activity of vibrational modes in the crystal.

Within harmonic approximation, vibrations or normal modes at each wave-vector $\vec{q}$ form a set of NxD eigenvectors of the mass-normalized Fourier

transform of force-constant matrix $\mathcal{D}^{i,j}_{k,k'}$ of a crystal with N atoms/call in D-dimensional space, and form an orthonormal basis [18]. Positive eigenvalues of $\mathcal{D}^{i,j}_{k,k'}$ (equal to the square of vibrational frequency (ω^2)) signify local stability of a crystal. Phonon spectra or dispersion of ω with respect to $\vec{q}$ along various lines in BZ connecting the high-symmetry points, the latter being representations of family of atomic planes of the crystal in the reciprocal (momentum) space [19]. Vibrational properties of crystals in equilibrium are experimentally determined from Raman spectroscopy or inelastic neutron scattering.

Acoustic phonons in the long-wavelength limit ($\vec{q} \to 0$) capture the elastic response (non-zero stress) of a crystal to mechanical strain [20]. At wavelengths of the order of inter-atomic distances, periodicity of the crystal entails deviation from linear dispersion of ω *versus* $|q|$ of sound wave [11] and resulting in a vanishing slope $\frac{d\omega}{d|q|}$ at $\vec{q} \in$ Brillouin Zone (BZ) boundaries. In a three-dimensional crystal, the softest acoustic phonons at the BZ boundary and the optical branch with the maximum frequency represent saddle points in the $\omega(q)$ dispersion. These critical points in the BZ lead to singularities in the density of vibrational states g(ω) known as van Hove singularities [21].

Optical phonons exist in a crystal with multi-atom basis in its unit cell, and thus are signatures of atomic arrangements and inter-atomic interactions. In most crystals, optical phonons exhibit frequencies higher than the regime of linear dispersion of acoustic bands for $\vec{q} \to 0$. Unstable phonons with imaginary ω signify lattice instabilities that result in structural transitions to low-symmetry phase [22], possibly in response to external perturbations namely strain [23], magnetic [24] or electric field, temperature [25] or

chemical-doping. Low-frequency phonons result in internal structural rearrangements at low energy-cost and make dominant contributions to vibrational entropy, with enhanced plausibility of polymorphism [26] or significant conformational changes [27].

While frequencies of optical modes at special q-points are pivotal in structural phase transitions, the nature of their dispersion in momentum space is yet another interesting feature. Certain crystals host normal (optical) modes with frequencies that are independent of wave-vector $\vec{q}$, that is, $grad(\omega(\mathbf{q}))$ = 0. Such flat bands of phonons across the entire BZ too exhibit strong peaks in g(ω) or a van Hove singularity [21]. When they occur at low ω, they cause interesting emergent phenomena reminiscent to inherent disorder or anharmonicity [28, 29].

Spontaneously broken continuous symmetries of disordered state and emergent acoustic phonons in the long-wavelength limit associated with elastic rigidity, and their couplings with optical modes lead to multiscale lattice-dynamics of crystals. Understanding the relevance of these concepts to the response of complex crystals (many atoms/cell) like metal-organic frameworks (MOFs), subjected to mechanical strain (ϵ) and thermal perturbation forms the core objective of this thesis. Mechanical response of a crystal involves elastic stresses, flexibility, phase transition or amorphization. Thermal perturbations give rise to varied nature of electronic and phononic excitations, and can result in wide variation in thermodynamic properties of materials. Fundamental origins of physical phenomena viz. flexibility, crystal-to-amorphous structural transition and associated *non-linear* elasticity, and deviation of T^3-dependence of heat capacity (known as the Boson Peak) of

crystalline solids are still unclear. In this thesis, we present first-principles theoretical analysis of response of crystals to mechanical stress fields, and develop phonon-based picture of (a) flexibility, (b) amorphization, (c) Boson peak and (d) structural transitions. We show that optical phonons of specific symmetry give rise to flexibility of crystals, in contrast to acoustic phonons that represent NG modes of elastic rigidity. Coupling between optical and acoustic phonon is shown to be crucial to flexibility, amorphization, structural phase transitions of crystals induced by mechanical deformation or kinetic arrest during synthesis.

In Part A of this thesis (Chapters 3 to 6), we unravel the origin of flexibility, amorphization and Boson peak of crystals by understanding (i) the *nonlinear* couplings between volumetric and shear strains in the long-wavelength limit, (ii) coupling between relevant optical modes and acoustic phonons, (iii) geometric origin of destabilization of a crystal (MOF-5) at infinitesimally strains, (iv) contributions of distinct atomic vibrations at low-ω, both of acoustic and optical character, to a peak in $C(T)/T^3$ of crystalline materials at low-T. We have used metal-organic frameworks (MOFs) as model systems, that are *ordered, truly crystalline* porous structures with large unit-cell dimensions.

While Au is a noble metal with FCC crystal structure, incipient stress-fields in constrained geometries can stabilize its non-FCC phases. In Part B (Chapters 7 and 8), we understand the temperature-dependent stability of kinetically arrested non-*fcc* (*bc(o,t))* phases in bipyramidal Au microcrystals with penta-twinned tips. We study the evolution of elastic strains in *bc(o,t))* phases in response to prolonged ion-irradiation and thermal annealing of

microcrystals, to understand experiments carried out by our collaborators, Professor G. U. Kulkarni and group, at JNCASR.

In Chapter 2, we present an overview of two quantum-mechanical computational methods employed in theoretical study of materials, (a) first-principles density functional theory (DFT) and density functional perturbation theory (DFPT), (b) density-functional tight binding approach. The topics here include Born-Oppenheimer approximation, Hohenberg-Kohn theorems, and Kohn-Sham equations. The algorithm to solve the Kohn-Sham equations to self-consistency and determination of ground state properties are briefly discussed. Further, two approaches for the calculation of phonons in crystals viz. frozen phonon method and linear response method are explained, with a discussion on their applicability and limitations. DFTB is parametrized directly within DFT and its calculations exhibit better scalability with number of atoms. Hence, it is widely employed for calculations of atomic and electronic structures, total energies and forces of *large* systems. The details of tight-binding scheme, and procedure of parameterization, starting from second-order expansion of Kohn-Sham total energy with respect to charge fluctuations are explained.

In Part A of this thesis (Chapters 3 to 6), we understand the origin of flexibility, amorphization and Boson Peak of crystals, considering MOFs as model systems.

MOFs have emerged as technologically relevant and fundamentally interesting class of crystalline materials [30, 31] with ultra-high porosity (up to 90% free volume) [32], low crystal densities and large internal surface areas. Their synthesis involves judicious assembly of molecular building units

bonded to strong ligand groups, to provide requisite directionality in construction of pre-determined topology of the framework [33,34]. The rational design and functionalization allow high degree of structural and chemical tunability of MOFs with extensive potential applications in gas storage and separation [35,36], catalysis [37], proton-conducting membranes for fuel cells [38] and drug delivery [39].

The structural and dynamical stability of these networks in response to external perturbations depends largely on the dynamics of their intermolecular degrees of freedom [40,41] and the strength of *non-linear* couplings between them. With a plethora of MOF structures encompassing diverse topologies reported till date, the nature of their structural transformations in response to mechanical strain and temperature vary extensively; certain MOFs exhibit large *flexibility* or reversible changes in pore-dimension up to large strains, while others undergo rapid amorphization leading to a partial or complete pore-collapse.

We now discuss the atomic structures of crystals studied in this thesis: (a) porous MOFs: MOF-5 and ZIF-8, and (b) non-porous crystals considered for understanding the concept of structural flexibility: ZrW_2O_8 and ZnO.

MOF-5

MOF-5 ($Zn_4O(BDC)_3$, $(BDC)^{2-}$=1,4-benzodicarboxylate) has a cubic structure (space group: $Fm\bar{3}m$) that consists of $Zn_4O(CO_2)_6$ units each containing four ZnO_4 tetrahedra with a common O-vertex [33], and remaining O-atoms

of each tetrahedra bound pairwise to C atoms (Figure 1.1a) to form carboxylate groups. These octahedral secondary building units (SBU) are linked to benzene rings along ⟨001⟩ direction. The benzene rings lie in {110} planes, with adjacent rings in mutually perpendicular orientations. This arrangement results in directionally constrained SBU imparting a high degree of stiffness to the MOF-5 crystal.

ZIF-8

ZIF-8 (Zn-$(MeIm)_2$, Me=CH_3-, IM=Imidazole group) has a sodalite structure (space group: $P2_13$) with Zn-N_4 tetrahedra corner-sharing with four five-membered Methyl-substituted Imidazole (Me-IM- or CH_3-$C_3N_2H_2$) linkers. The resulting three-dimensional network shows six-membered rings along [111] and four-membered rings along [001] (Figure 1.1b), and enclose a cube-octahedron pore. The IM linkers are oriented on {112} planes, and aligned alternately in out-of-plane direction.

ZrW_2O_8

ZrW_2O_8 crystallizes in a cubic structure (space group: $P2_13$) that is similar to NaCl, but lacking the inversion centre. Each face-centred Zr atom serves as a hinge to two WO_4 tetrahedra. W atom and one O-atom of each of the tetrahedra are aligned along the three-fold [111] axis (Figure 1.1c) [42]. Since the two WO_4 tetrahedra are not symmetric with respect to each other, these form crystallographically distinct entities and can undergo independent rotations. The presence of singly-coordinated O-atom to W and

a large inter-tetrahedral distance ($\sim$2.41 $\mathring{A}$) invokes displacements of rigid-tetrahedra along the [111] or orientational disorder about [111]. A significant difference between the lengths of 4 W-O bonds of WO_4 tetrahedra ($\sim$1.83 $\mathring{A}$ and $\sim$1.73 $\mathring{A}$) augments the tendency of these entities to undergo structural distortion in response to perturbations namely temperature, pressure or homogeneous strains. Liberational modes of tetrahedra have been linked to bond shortening and negative thermal expansion coefficient of ZrW_2O_8 [43].

ZnO

ZnO has a wurtzite structure formed by two inter-penetrating *hcp* lattices, consisting of Zn and O atoms respectively. The lattices have the common c-axis, with an ideal vertical distance of $3/8c$ between them. Zn (or O) at (0,0,0) are coordinated with 4 nearest O (or Zn) atoms forming a tetrahedron, which in turn has 12 tetrahedra as its nearest neighbors (Figure 1.1d).

Flexibility of MOFs is associated with their tendency to undergo cooperative structural transformation [44] in response to external stimuli, while maintaining their crystallanity and coordination network. In a broad sense, stimuli may be related to host-guest interaction, mechanical deformation, thermal, electrical or magnetic perturbations [45]. Flexibility is a property crucial to their structural tunability is ubiquitously known to emerge from framework dynamics involving breathing and swelling modes, linker rotation or sub-lattice sliding [46, 47]. While flexibility is intuitively linked to reversible response and low elastic moduli [44] or soft vibrational modes of a crystal, its quantitative measure is still lacking. In Chapter 3, we introduce

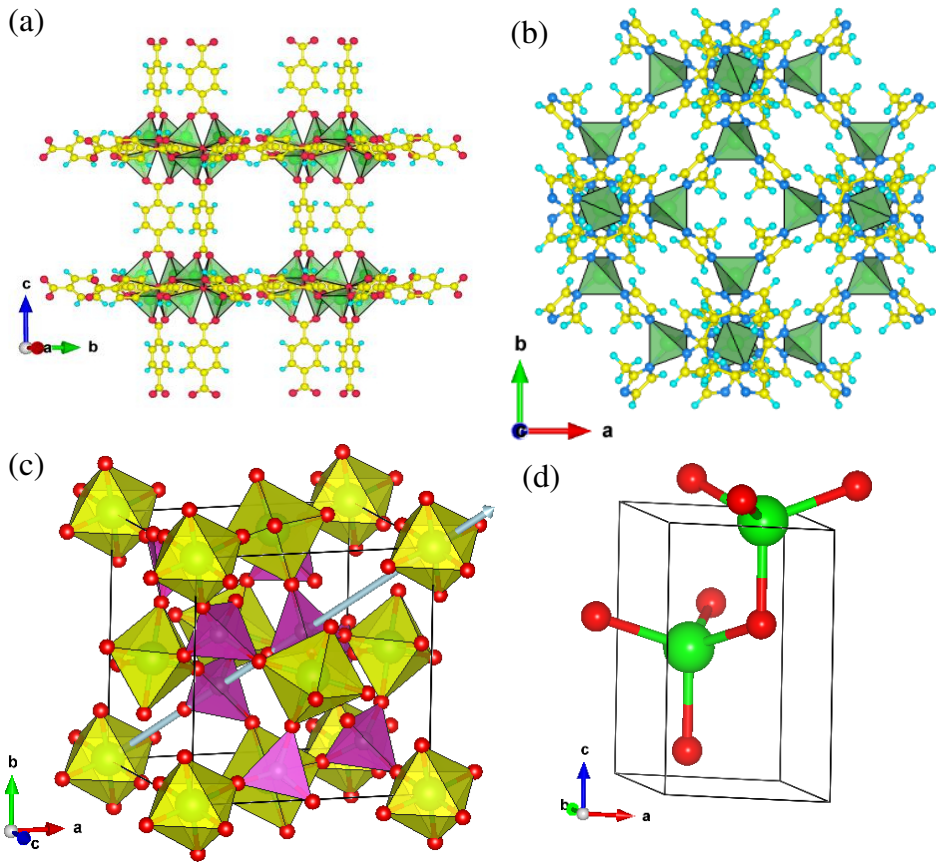

Figure 1.1: Atomic structures of crystals considered in this thesis: (a) MOF-5, (b) ZIF-8, (c) ZrW_2O_8, and (d) ZnO.

a precise measure of structural flexibility tensor ($0 < \bar{F}^s < 1$) of a crystalline material as the fractional release of elastic strain-energy or stress through symmetry-preserving internal structural rearrangements. We determine flexibility of distinct classes of crystals viz. ZnO, ZIF-8, MOF-5 and ZrW_2O_8 with respect to hydro-static (ϵ_h) and rhombohedral shear (ϵ_r) deformation using first-principles density functional theoretical analysis. Similar to the flowability of liquids, flexibility of crystals involves contributions from large structural rearrangements corresponding to soft phonons. Surprisingly however, we show that flexibility can be dominated by hard phonons that couple

strongly with strain field, highlighting its multi-scale origin. While rigidity of a system generally manifests through Goldstone modes emerging at the breaking of a continuous symmetry, flexibility causes reduction in this rigidity by symmetry-preserving internal *continuous* degrees of freedom. This concept of flexibility generalizes to any long-range ordered state emerging from continuous symmetry-breaking.

MOF-5 is a metal-organic framework (MOF) with large pore volume and exceptional thermal stability [1]. However, it undergoes irreversible amorphization at minuscule pressures, of the order of 10 MPa [48]. Earlier studies have attributed this crystal-to amorphous structural transition to rupture of the carboxylate bonds of its *rigid* secondary building unit (SBU) [3, 48], leading to complete pore-collapse. With multitude of vibrational degrees of freedom (DoFs) of MOF-5 spanning a broad range of frequencies, preferential cleavage of its strong carboxylate (C-O) bonds in response to small pressures of a few MPa is quite inconceivable. In Chapter 4, through first-principles phonon-spectral analysis, we demonstrate that a *stable* MOF-5 crystal cannot sustain hydrostatic compression, primarily due to symmetry-lowering torsional forces that distort its octahedral SBUs upon infinitesimal strain, $\epsilon_h \sim$ -0.003. Group-theoretical analysis of phonons of MOF-5 unravels the role of triply degenerate phonons with relatively higher frequencies in its destabilization leading to an order-to-disorder structural phase transition at very small compressive strains. At large strains, we show that MOF-5 structures distorted along the randomized eigenvectors of the flat, unstable phonon bands relax to lower-energy states, disrupting the long-range order

of the MOF-5 crystal and resulting in its amorphization, with colossal release of stresses. The microscopic mechanism of destabilization involving orientational disordering in SBUs of MOF-5 is generalizable to many other MOFs that encase directionally constrained rigid building units in their three-dimensional network structure [34].

Amorphization of yet another *stable* porous framework, ZIF-8 [49], on ball-milling [50] or in response to modest pressure (P $\sim$ 0.3 GPa) [51] has been a subject of active research for many years. Its crystal-to-amorphous structural transition is largely attributed to its exceptional low shear modulus [52] and occurrence of shear instability upon compression [53]. In Chapter 5, we first establish the inherent *non-linear* elastic behavior of ZIF-8 due to higher-order moduli in its elastic strain-energy with respect to hydrostatic (ϵ_h) and rhombohedral shear (ϵ_r) strains, and coupling between long-wavelength TA and LA phonons. Dynamical stability of ZIF-8 at large shear stains ($\epsilon_r \sim$ 0.07) counters the role of soft shear modulus (C_{44}) in its destabilization [52]. However, ZIF-8 undergoes a shear instability (i.e. negative C_{44}) and dynamical lattice instability at hydrostatic compressive strain $\epsilon_h \sim$ -0.035. At large compressive strains, the soft unstable modes form non-dispersive flat bands throughout the BZ. Relaxation of (2 x 2 x 2) hydro-statically strained cells of crystalline ZIF-8 distorted along random combinations of eigen-vectors of unstable modes shows disruption of its long-range order leading to amorphization. Analysis of *densified* structure obtained on ball-milling and modeled using reverse Monte-Carlo approach [50], unfolds significant distortion of ZnN_4 tetrahedra in addition to the loss of long-range order.

Amorphous MOFs largely involve collapse of the porous structure of their

crystalline counterparts in response to mechanical stains with or without guest species. This enhances their gas-storage capacity, with a potential application in irreversible long-term capture of harmful gases or molecular substances [54, 55]. Furthermore, collapse of zeolitic structures has been reported to produce inorganic glasses. Recently, amorphous MOFs have been reported to exhibit chemical versatility and efficiency in separation of ions and similar-sized molecules [56]. Quite interestingly, a Zr-based amorphous MOF, UiO-66 exhibits superior capacitance than its crystalline counterpart and hence is a promising material for supercapacitor electrode material [57].

Ubiquitous occurrence of Boson peak (BP) in glassy and amorphous phases, and its stark absence in crystals, have intrigued researchers for several decades. Lack of sharp spectroscopic signatures and appearance of broad vibrational peaks in glasses at low frequencies make it challenging to probe their atomic-structure details and microscopic structural origin. In Chapter 6, we provide evidence for BP(s) in crystalline MOFs, manifesting as (a) peak in $C(T)/T^3$ at very low-T, and (b) multiple peaks in reduced density of states $g(\omega)/\omega^2$ at low-frequencies through analysis of two model MOFs: MOF-5 and ZIF-8. Lattice vibrations that constitute BP of MOF-5 represent *composite* phonons resulting from strong coupling between quasi-localized acoustic branches at the BZ boundary and flat non-dispersive optical phonons. In ZIF-8, BP emerges from shear modes, as well as modes that involve buckling or rippling of IM-ring about metal centers. Distinct nature of these atomic vibrations highlight the role of underlying topology and chemical interactions responsible for BP in crystals, and elucidates that its origin is not quite universal. While BP was attributed to low-ω van Hove singularity in

crystals in earlier studies [58, 59], our work shows that it has contributions from soft acoustic modes ($\omega \rightarrow 0$, $|q| \rightarrow 0$) of certain crystals (ZIF-8 in the present case), coupling of flat (non-dispersive) optical phonons with LA and TA phonon branches, indicating that multiple strong discontinuities in the density of states g(ω) at low ω can, in principle, constitute BP, and give rise of deviation of C(T) with respect to the Debye model.

In Chapter 7, we understand how incipient elastic stresses stabilize the non-*fcc* (*bc(o,t)*) phases of Au in twinned bipyramidal microcrystals at ambient conditions [60]. We determine the temperature-dependent free energies of experimentally-observed (*bc(o,t)*) structures with respect to fcc Au, and attribute their stability to soft phonons. We present a soft mode-based mechanism that captures the trends in stability of non-*fcc* phases of noble metals.

A systematic study of time-dependent irradiation of corrugated bi-pyramidal Au-micro-crystals with low-energy Ar^+ ions, carried out by our experimental collaborators, has shown controlled transformation of one metastable non-*fcc* phase to another in the core of micro-crystals, *bco* $\rightarrow$ *bct* $\rightarrow$ *bct1*. These structures differ primarily in the magnitude of *locked-in* strains along the [001]-direction, resulting in the shift of (002) XRD peak of *bct*-Au to lower 2θ values. In contrast to thermal annealing that gives rise to spatially non-homogeneous elastic strains, structural changes induced by Ar^+ irradiation emerge as uniform strains across the entire microcrystallites, as characterized by narrow XRD peaks on prolonged exposure. In Chapter 8, we present a plausible mechanism of heat transfer that leads to homogeneous elastic strains in the core of micro-crystallite with a thickness of about 200-250 nm,

that is significantly larger than the mean-free path of electrons in Au crystal ($\sim$ 40 nm). We propose that a transient thermodynamic state at the collision cascade-core interface manifests as a time-lag τ between heat flux and temperature-gradient [61], invoking a non-Fourier mechanism of heat conduction by electrons on ion-irradiation of Au-microcrystallite. Electrons in *non-equilibrium* percolate into the core as a thermal wave with a finite speed that depends on time-lag. Larger the τ, slower is the wave. Additive character of structural changes provides an evidence of correlation between elastic strains at consecutive time-intervals of ion-irradiation. Emergent *hot* excited electrons in the *core* of Au-microcrystallites tune the elastic strains of non-*fcc* phases, as demonstrated by optimization of strained structures at varying width of Fermi-Dirac distribution of electrons in Au.

Finally, in Chapter 9, we summarize the ideas developed in this thesis. We suggest future research directions in the study of mechanical response of MOFs and study of generalized aspects of flexibility.

Chapter 2

Theoretical Formalism

Materials are composed of nuclei bound together by electrons. Since the typical energy scales for electrons far exceed those associated with the degrees of freedom of the massive nuclei, the lowest energy ground state of the electrons determines the structure of the nuclei, thus precisely determining the ground state material-properties viz. equilibrium crystal structure, charge density, phase transition between structures, and many others. This key concept has guided the the development of accurate, robust methods to treat electronic ground state, and hence the understanding of structure of materials at the atomic scale.

By far, the most widespread approach for 'first-principles' quantitative calculations of material-structure and properties is density functional theory (DFT). This chapter discusses the formulation of density functional theory, and the underlying independent-particle approximations to address real many-body problems of electrons in materials.

Further, the response of a material to external stimulus, namely, the displacements of nuclei about their mean positions, can be studied from their vibrational spectrum, measured experimentally by inelastic neutron scattering, infra-red absorption, etc. Theoretically, this response can be determined through changes in electronic energies (E_{total}), forces on the nuclei (F_I), and force constants (C_{IJ}) with changes in atomic positions, leading to the calculation of full phonon dispersion curves. The later part of this chapter reviews two approaches of phonon calculations, namely, frozen phonons and linear response [62].

2.1 Introduction

The fundamental Hamiltonian for a system of electrons and nuclei is given by:

$$\hat{H} = -\frac{\hbar^2}{2m_e}\sum_i \nabla_i^2 + \sum_{i,I}\frac{Z_I e^2}{|\mathbf{r}_i - \mathbf{R}_I|} + \frac{1}{2}\sum_{i\neq j}\frac{e^2}{|\mathbf{r}_i - \mathbf{r}_j|}, \\ -\sum_I \frac{\hbar^2}{2M_I}\nabla_I^2 + \frac{1}{2}\sum_{I\neq J}\frac{Z_I Z_J e^2}{|\mathbf{R}_I - \mathbf{R}_J|} \tag{2.1}$$

The terms on the right-hand side of Eq. 2.1 represent, in order, the kinetic energy of electrons, Coulomb interactions between electrons and the nuclei, the Coulomb interactions between pairs of electrons, kinetic energy of nuclei, and Coulomb interactions between pairs of nuclei. The nuclear kinetic energy can be ignored, considering the mass M_I to be infinity, relative to that of electrons. This is called the *Born-Oppenheimer or adiabatic approximation*. Within this approximation, the nuclear dynamics does not cause electronic

transitions, allowing the total wavefunction to be written as a product of electronic and nuclear wavefunctions:

$$\Psi_{ni}(\{\mathbf{r},\,\mathbf{R}\}) = \chi_{ni}(\mathbf{R})\psi_i(\{\mathbf{r},\,\mathbf{R}\}) \tag{2.2}$$

where $\chi_{ni}(\mathbf{R})$ is the nuclear wavefunction which is a function of coordinates R and depends on both vibrational and electronic quantum numbers, n and i, respectively. The electronic wavefunction, $\psi_i(\mathbf{r}, \mathbf{R})$, is a function of both the nuclear and electronic coordinates, but only depends upon the electronic quantum number or electronic state, i.

For each electronic state i, each nuclear wavefunction is determined as:

$$\left[-\sum_J \frac{\hbar^2}{2M_J}\nabla_J^2 + U_i(\{\mathbf{R}\}) - E_{ni}\right]\chi_{ni}(\mathbf{R}) = 0; \tag{2.3}$$

and the many-body wavefunction for the electrons, $\psi_i(\mathbf{r}, \mathbf{R})$ is obtained by solving time-independent Schrödinger equation:

$$\hat{H}_{elec}\psi_i(\mathbf{r},\,\mathbf{R}) = E_i\psi_i(\mathbf{r},\,\mathbf{R}) \tag{2.4}$$

Here, the electronic hamiltonian is given as:

$$\hat{H}_{elec} = \hat{T} + \hat{V}_{ext} + \hat{V}_{int} \tag{2.5}$$

with kinetic energy operator for electrons ($\hat{T}$), potential acting on electrons due to the nuclei (V_{ext}), and electron-electron interactions (V_{int}). The three

terms can be written as:

$$\hat{T} = \sum_i -\frac{\hbar^2}{2m_e}\nabla_i^2, \quad \hat{V}_{ext} = \sum_{i,I} V_I(|\mathbf{r}_i - \mathbf{R}_I|), \quad \hat{V}_{int} = \frac{e^2}{2}\sum_{i\neq j}\frac{1}{|\mathbf{r}_i - \mathbf{r}_j|} \quad (2.6)$$

The ground state wavefunction Ψ_o, the state with lowest energy, can be determined by minimizing the total energy with respect to all the parameters in $\Psi(\{\mathbf{r}_i\})$, with the constraint that Ψ must obey the particle symmetry and conservation laws. While all the other terms in Eq. 2.6 are exactly known in terms of Ψ, the exact value of electron-electron Coulomb interactions, V_{int} cannot be computed, and thus need to be approximated. Two independent-particle approaches, *effective single-particle* and *Hartree-Fock*, do not include electron correlations. Hartree-Fock approach includes electron-electron Coulomb interaction in the energy, while neglecting the correlations in wavefunctions. The 'effective single-particle' theories have an effective potential that incorporates some effect of real interaction, without an interaction term explicitly included in the effective Hamiltonian.

2.2 Density Functional Theory

Density functional theory is a theory of correlated many-body systems, having close associations with independent-particle methods. The works of Hohenberg-Kohn in 1964, and Kohn-Sham in 1965 have led to the formulation of DFT, which has now become the basis of present-day methods for treating electrons in atoms, molecules, and condensed matter.

2.2.1 Hohenberg-Kohn theorems

The two theorems proposed by Hohenberg and Kohn set the basis to formulate density functional theory as an exact theory of many-body systems.

Theorem I: For any system of interacting particle in an external potential $V_{ext}(\mathbf{r})$, the potential $V_{ext}(\mathbf{r})$ is determined uniquely by the ground state particle density, $n_o(\mathbf{r})$, except for a constant. Thus all properties of the system can be completely determined, once the ground state density $n_o(\mathbf{r})$ is known.

Theorem II: A universal functional for the energy E[n] in terms of the density $n(\mathbf{r})$ can be defined, for any external potential, $V_{ext}(\mathbf{r})$. For any particular $V_{ext}(\mathbf{r})$, the exact ground state energy of the system is the global minimum value of this functional, and the density $n(\mathbf{r})$ that minimizes the functional is the exact ground state density $n_o(\mathbf{r})$. The total energy functional, as uniquely determined by $n(\mathbf{r})$, is given by:

$$E_{HK}[n] = T[n] + \int d^3r V_{ext}(\mathbf{r}) n(\mathbf{r}) + E_{int}[n] + E_{II} \tag{2.7}$$

and E_{II} denotes the classical interactions of nuclei with one another.

A functional $F_{HK}[n]$, which includes kinetic and potential energies of interacting electron system, can be defined as:

$$F_{HK}[n] = T[n] + E_{int}[n] \tag{2.8}$$

Thus, if the functional $F_{HK}[n]$ is known, then by minimization of total energy with respect to n($\mathbf{r}$), the exact ground state density and energy can be determined.

The operational difficulty in the above formulation is that there is no known way to extract kinetic energy directly from the density . When represented in terms of a set of N wavefunctions, the derivatives of kinetic energy as a function of number of electrons are discontinuous at integer occupation numbers. This implies that the exact functional will vary in a non-analytic manner as a function of number of electrons. This leads to Kohn-Sham approach, where kinetic energy is treated in terms of orbitals and interaction terms explicitly modeled as functionals of the density.

2.2.2 Kohn-Sham Ansatz

The approach proposed by Kohn and Sham for electronic structure calculations is to replace the original many-body problem by an auxilliary independent particle problem. The density of the original system is assumed to be equal to that of non-interacting system, and the interactins are incorporated into an exchange-correlation functional of the density. The auxiliary hamiltonian of the system has a kinetic operator and an effective local potential, $V^{\sigma}_{eff}(\mathbf{r})$ acting on an electron of spin σ at a point $\mathbf{r}$. The Kohn-Sham Schrödinger-like equations can be expressed as :

$$(H^{\sigma}_{KS} - \varepsilon^{\sigma}_{i})\psi^{\sigma}_{i}(\mathbf{r}) = 0 \tag{2.9}$$

where the ε_i are the eigenvalues, and H^{σ}_{KS} is the effective hamiltonian

$$\hat{H}^{\sigma}_{KS} = -\frac{1}{2}\nabla^2 + V^{\sigma}_{KS}(\mathbf{r}), \quad \text{using Hartree atomic units} \tag{2.10}$$

The expression for the ground state energy functional can be written as:

$$V^{\sigma}_{KS} = V_{ext}(\mathbf{r}) + V_{Hartree}(\mathbf{r}) + V_{XC}(\mathbf{r}) \tag{2.11}$$

where $E_{Hartree}$ is the self-interaction energy of density $n(\mathbf{r})$. The density of the system is given by:

$$n(\mathbf{r}) = \sum_{\sigma}\sum_{i=1}^{N^{\sigma}} |\psi^{\sigma}_i(\mathbf{r})|^2 \tag{2.12}$$

and the kinetic energy T_s, as a functional of orbitals, is given by:

$$T_s = \frac{1}{2}\sum_{\sigma}\sum_{i=1}^{N^{\sigma}} \int d^3r |\psi^{\sigma}_i(\mathbf{r})|^2 \tag{2.13}$$

The total electronic energy, E_{KS} given by:

$$E_{KS} = T_s[n] + \int d\mathbf{r} V_{ext}(\mathbf{r}) n(\mathbf{r}) + \frac{1}{2}\int d^3\mathbf{r} d^3\mathbf{r}' \frac{n(\mathbf{r})n(\mathbf{r'})}{|\mathbf{r}-\mathbf{r'}|} + E_{II} + E_{XC}[n] \tag{2.14}$$

when minimized with respect to either the density $n(\mathbf{r})$, or the effective potential $V^{\sigma}_{eff}(\mathbf{r})$ leads to the ground state of the system. The only crucial ingredient that needs to be determined for obtaining the exact solution for the Kohn-Sham equations (Eq. 2.9-2.11) is the exchange-correlation functional E_{XC}, the approximations to which are discussed below.

2.2.3 Exchange-correlation functionals

In the Schrödinger equation, the motion of each electron is coupled to the motion of every other electron through Coulomb repulsions among them. This repulsion lowers the electrostatic energy, and the energy reduction is termed as the exchange-correlation energy of the system. The exchange-correlation potential, V_{XC} in the effective Hamiltonian (Eq. 2.10) is given by:

$$V_{XC} = \frac{\delta E_{XC}}{\delta n(\mathbf{r})} \tag{2.15}$$

Accurate approximations of E_{XC} are necessary to obtain ground state energy and density. Kohn and Sham proposed a non-empirical approximation using exchange-correlation energy per electron, $\varepsilon_{xc}^{uniform}(n)$ of an electron gas of uniform density n. This is called 'local density approximation (LDA)'. The real system with nonuniform density is assumed to locally consist of infinitesimal volume elements, each with a uniform electron density. This leads to the following relation for E_{XC}:

$$E_{XC}^{LDA}[n] = \int d^3r n(\vec{r}) \varepsilon_{xc}^{uniform}(n(\vec{r})) \tag{2.16}$$

This approximation is exact for uniform density and correct and accurate for systems with spatially-varying density.

To make the functional more accurate, the idea of exchange-correlation energy in terms of density, $n(\vec{r})$, can be extended to include additional exact constraints into the approximations. Adding a second element, the gradient of density, gives rise to 'generalized gradient approximation (GGA)' of the

exchange-correlation functional, which is expressed as:

$$E_{XC}^{GGA}[n] = \int d^3r n(\vec{r}) \varepsilon_{xc}^{approx}(n(\vec{r}), \nabla n(\vec{r}) \tag{2.17}$$

2.2.4 Solving Kohn-Sham equations

The set of Schrödinger-like one-electron equations i.e. Eqs 2.9-2.11, need to be solved such that the $V_{eff}(\mathbf{r})$ and density $n(\mathbf{r})$ are consistent. The steps involved in solving these equations to acheive self-consistency are as under:

1. Consider a trial electron density, $n(\mathbf{r})$.
2. Calculate $V_{eff}(\mathbf{r})$ using Eq. 2.11.
3. Solve for electron wavefunctions (Eq. 2.9 and 2.10).
4. Calculate a new electron density using Eq. 2.12.
5. Check for the convergence of $n(\mathbf{r})$. If achieved, calculate total energy E_{KS} (Eq. 2.14), forces, stresses, and eigenvalues, otherwise reiterate the calculations from Step 2.

2.3 Force and stress from electronic structure

2.3.1 Force theorem

The force theorem, derived by Feynman in 1939, states that the force on the nucleus is strictly in terms of the charge density, independent of the electron kinetic energy, exchange, and correlation. In electronic structure theory, this is termed as "Hellmann-Feynman theorem". The force $\mathbf{F}_I$ acting on a nucleus

$\mathbf{R}_I$ is given as:

$$\mathbf{F}_I = -\frac{\partial E}{\partial \mathbf{R}_I} = -\int d^3 r n(\mathbf{r}) \frac{\partial V_{ext}(\mathbf{r})}{\partial \mathbf{R}_I} - \frac{\partial E_{II}}{\partial \mathbf{R}_I} \tag{2.18}$$

It is important to note that Eq. 2.18 follows if the electron density is held constant to first order as the nucleus moves.

2.3.2 Stress calculations

In condensed matter, the state of a system is specified by the forces on each atom and the stress. The forces that act upon (or through) the surface of the element, due to the surrounding material contribute to the stresses transmitted throughout the volume of the element. Strain is deformation of a material that causes a displacement $\mathbf{u}$ of a point $\mathbf{r}_i \rightarrow \mathbf{r}'_i$, as a function of the coordinate $\mathbf{r}$. The strain tensor $\epsilon_{\alpha\beta}$, can be defined as:

$$\epsilon_{\alpha\beta} = \frac{1}{2}\left(\frac{\partial u_\alpha}{\partial r_\beta} + \frac{\partial u_\beta}{\partial r_\alpha}\right) \tag{2.19}$$

over Cartesian indices, α,β. In quantum mechanics, if a system is in equilibrium and the strain is homogeneous over macroscopic regions, the macroscopic average stress tensor $\sigma_{\alpha\beta}$ is defined in terms of energy and strain tensor $\epsilon_{\alpha\beta}$ per unit volume as:

$$\sigma_{\alpha\beta} = -\frac{1}{\Omega}\frac{\partial E}{\partial \epsilon_{\alpha\beta}} \tag{2.20}$$

The stress-strain relations describe elastic phenomena in materials. For example, the elastic constants are given by:

$$C_{\alpha\beta;\gamma\delta} = \frac{1}{\Omega}\frac{\partial^2 E_{total}}{\partial u_{\alpha\beta}\partial u_{\gamma\delta}} = -\frac{\partial \sigma_{\alpha\beta}}{\partial u_{\gamma\delta}} \tag{2.21}$$

Further, the above definition of stress (Eq. 2.20) with the assumption of homogeneous scaling of space, that include electronic wavefunctions and position of nuclei. However, to obtain the correct value of stress, one one must impose an additional requirement that the force on each atom vanishes on relaxation, $\mathbf{F}_I = 0$, in presence of the homogeneous strain $\epsilon_{\alpha,\beta}$. In other words, the system attains an energy-minumum with respect to all internal degrees of freedom. Only for simple crystal structures and certain symmetric strains, the positions of the nuclei are fixed by symmetry. In most real materials, the displacements of atoms on relaxation, at which $\mathbf{F}_I \approx 0$ is satisfied, are:

$$u_\alpha = \sum_\beta \epsilon_{\alpha\beta} u_\beta + u_\alpha^{int} \tag{2.22}$$

The first term represents uniform scaling of space, $\mathbf{R}_\alpha \rightarrow (\delta_{\alpha\beta} + \epsilon_{\alpha\beta})\mathbf{R}_\beta$. The second term shows deviation from the unrelaxed structure, or "internal strains", which are crucial for estimating stress-strain curves in low-symmetry materials. The calculation of these internal strains is one of the key areas where theoretical analysis makes precise information about the atomic structure accessible, in contrast to the difficulty in resolving the atomic positions in a strained systems through experiments.

2.4 Pseudopotentials

The idea behind construction of pseudopotentials is to replace the strong Coulomb potential of the nucleus and the effect of tightly bound core electrons by an effective ionic potential acting on the valence electrons. The aim of pseudopotential theory is to find effective potentials that represent the scattering over the desired energy range. Most present-day electronic calculations are based on '*ab initio* norm-conserving pseudopotentials' and 'ultrasoft pseudopotentials'.

2.4.1 Norm-conserving pseudopotentials (NCPPs)

The norm-conserving pseudofunctions ψ^{PS} are normalized and are solutions of model potential chosen to reproduce the valence properties of an all-electron calculations. The orthogonality condition:

$$\langle \psi_i^{\sigma,PS} | \psi_j^{\sigma',PS} \rangle = \delta_{i,j}\delta_{\sigma,\sigma'} \tag{2.23}$$

needs to be satisfied so that the Kohn-Sham equations has the same form:

$$(H_{KS}^{\sigma,PS} - \varepsilon_i^{\sigma})\psi_i^{\sigma,PS}(\mathbf{r}) = 0 \tag{2.24}$$

To be defined as a good *ab initio* pseudopotential, it is required that the NCPP equals the atomic potential outside the "core region" of radius R_c, the logarithmic derivatives of the all-electron and pseudo wavefunctions agree at R_c, the first energy derivative of the logarithmic derivatives of the pseudo- and 'real' wave functions agree at R_c, and the norm-conservation condition

is satisfied.

2.4.2 Ultrasoft pseudopotentials

Ultrsoft pseudopotentials accurately calculate the effective potential by a transformation that re-defines the problem in terms of a smooth function, and an auxilliary function around each ion core that represents the rapidly varying part of the density. The condition of norm-conservation is generalized. Thus, the critical radius R_c much larger than for the norm-conserving pseudopotential can be chosen, while maintaining the desired accuracy.

2.5 Calculation of Phonons

Vibrational spectra provide wealth of information about the lattice-dynamical behavior of solids. Accurate information on the force constants, static dielectric constants, piezoelectric constants, electron-phonon interactions etc. can be provided by theory of phonons, which is ultimately a part of electronic structure. The total energy, within Born-Oppenheimer approximation, can be viewed as a function of the positions of the nuclei $E(\{\mathbf{R}_i\})$. The two approaches in the calculation of phonons using first-principles theory are:
(1) Direct calculation of total energy as a function of the positions of the atoms (frozen phonon method)
(2) Perturbative approach involving calculations of the derivative of energy (response function method)

2.5.1 Frozen phonons

In frozen phonon method, a small, but finite perturbation is frozen in the system, and the total energy and forces are calculated with nuclei "frozen" at positions $\{\mathbf{R}_I\}$. The forces on atoms can be calculated within the framework of density functional theory, which makes it a direct approach for phonon calculations. Then, the force constant matrix elements defined by numerical dervatives of displacements are calculated as :

$$C_{I,\alpha;J,\beta} \approx -\frac{\Delta F_{I,\alpha}}{\Delta \mathbf{R}_{J,\beta}} \tag{2.25}$$

and dynamical matrix $\tilde{D}_{I,\alpha;J,\beta}$ is computed from the force constant matrix as:

$$\tilde{D}_{I,\alpha;J,\beta} = C_{I,\alpha;J,\beta}\frac{1}{\sqrt{M_I M_J}} \tag{2.26}$$

Phonon frequencies and eigenvectors are obtained by diagonalization of the dynamical matrix. However, this technique determines phonon dispersion curves for a crystal only with large "supercell" calculations, whose size depends on commensurability of perturbation, hence increasing the computational cost of phonon calculations at lower **q**-points.

2.5.2 Density Functional Perturbation Theory

Perturbative theory involves systematic expansion of hamiltonian $\hat{H}^o + \lambda\Delta\hat{H}$ in the powers of the perturbation. The first order expressions depending on unperturbed wavefunctions and $\Delta\hat{H}$ to the first-order are given as the "generalized force" on an atom. To obtain the interatomic force constants

(IFCs), we need to compute second derivatives of ground state energy of a system of spin-less electrons with respect to the perturbation i.e. nuclear displacements, which can be calculated using efficient electronic structure methods. This is given by:

$$\frac{\partial^2 E(\{\mathbf{R}\})}{\partial \mathbf{R}_I \partial \mathbf{R}_J} = \int \frac{\partial n(\mathbf{r})}{\partial \mathbf{R}_J} \frac{\partial V_{[R]}(\mathbf{r})}{\partial \mathbf{R}_I} d\mathbf{r} + \delta_{IJ} \int n(\mathbf{r}) \frac{\partial^2 V_{[\mathbf{R}]}(\mathbf{r})}{\partial \mathbf{R}_I \partial \mathbf{R}_J} d\mathbf{r} + \frac{\partial^2 E_N(\{\mathbf{R}\})}{\partial \mathbf{R}_I \partial \mathbf{R}_J} \tag{2.27}$$

The linear response of the charge density with respect to atomic positions can be calculated as:

$$\frac{\partial n(\mathbf{r})}{\partial \mathbf{R}_I} = 4Re \sum_{n=1}^{N/2} \psi_n^*(\mathbf{r}) \frac{\partial \psi_n(\mathbf{r})}{\partial \mathbf{R}_I} \tag{2.28}$$

The derivatives of KS orbitals, $\frac{\partial \psi_n(\mathbf{r})}{\partial \mathbf{R}_I}$ are calculated as:

$$(H_{SCF} - \epsilon_n) \frac{\partial \psi_n(\mathbf{r})}{\partial \mathbf{R}_I} = - \left(\frac{\partial V_{SCF}(\mathbf{r})}{\partial \mathbf{R}_I} - \frac{\partial \epsilon_n}{\partial \mathbf{R}_I} \right) \psi_n(\mathbf{r}) \tag{2.29}$$

with first-order derivative of self-consistent potential given as:

$$\frac{\partial V_{SCF}(\mathbf{r})}{\partial \mathbf{R}_I} = \frac{\partial V_{[\mathbf{R}]}(\mathbf{r})}{\partial \mathbf{R}_I} + e^2 \int \frac{1}{|\mathbf{r} - \mathbf{r}'|} \frac{\partial n(\mathbf{r}')}{\partial \mathbf{R}_I} d\mathbf{r}' + \int \frac{\delta \upsilon_{xc}(\mathbf{r})}{\delta n(\mathbf{r}')} \frac{\partial n(\mathbf{r}')}{\partial \mathbf{R}_I} d\mathbf{r}' \tag{2.30}$$

and first-order derivative of the KS eigenvalue, ϵ_n, expressed as:

$$\frac{\partial \epsilon_n}{\partial \mathbf{R}_I} = \left\langle \psi_n \left| \frac{\partial V_{SCF}}{\partial \mathbf{R}_I} \right| \psi_n \right\rangle \tag{2.31}$$

The Eqs. (2.28-2.31) form a set of self-consistent equations for calculation of second-order derivatives of ground state energy. Solution of the linear system

of equations can be obtained by employing efficient iterative techniques such as conjugate gradient or the steepest descent. Fourier transform of the matrix of inter-atomic force constants, $C_{I,\alpha;J,\beta}(\mathbf{R})$ is denoted as $\tilde{C}_{I,\alpha;J,\beta}(\mathbf{q})$, and represents the second derivative of energy with respect to atomic displacements $\mathbf{u}$ at a wave-vector $\mathbf{q}$:

$$\tilde{C}_{I,\alpha;J,\beta}(\mathbf{q}) = \sum_{\mathbf{R}} exp^{-\mathbf{q}.\mathbf{R}} C_{I,\alpha;J,\beta}(\mathbf{R}) \tag{2.32}$$

Phonon frequencies $\omega(\mathbf{q})$ are the solution of secular equation:

$$det \left| \frac{1}{\sqrt{M_I M_J}} \tilde{C}_{I,\alpha;J,\beta}(\mathbf{q}) - \omega^2(\mathbf{q})\mathbf{I} \right| = 0 \tag{2.33}$$

where M_I, M_J are the atomic masses and $\mathbf{I}$ is the identity matrix. The dispersion of frequencies $\omega(\mathbf{q})$ at $\mathbf{q}$-points along various high-symmetry lines in the first Brillouin Zone is often used to view the vibrational spectrum of a crystalline solid. Other information derived from the phonon calculations includes phonon density of states and electron-phonon coupling.

2.6 Density Functional Tight Binding approach

The standard tight-binding method involves representation of eigenstates of Hamiltonian in orthogonalized basis of atom-like orbitals, and expressing the inter-atomic charge fluctuations or short-range repulsive interactions as a parameterized Hamiltonian matrix, where the matrix elements are fitted to the electronic properties of a reference structure. Density functional tight-binding (DFTB) is a quantum-mechanical approach, parameterized directly

from DFT [63]. It is used for calculation of total energies, and derived properties, of *large* systems primarily because of its simplicity and better scaling with respect to DFT [64]. This requires the availability of accurate parameters for constituent entities, akin to tight binding method.

In DFTB, the Hamiltonian matrix elements are explicitly determined within a non-orthogonal basis of atomic orbitals, and charge distribution in the chemical bonds of multi-atom systems is treated in a self-consistent manner [65]. Tightly bound electrons of atoms are treated perturbatively to incorporate the effect of inter-atomic interactions, particularly the short-range repulsion.

The total energy E[n] within DFT (Equation 2.8) expressed as a functional of electron density n($\mathbf{r}$), and the energy of the Kohn-Sham system of non-interacting electrons as in Equation 2.14, form the basis of DFTB formulation. Here, the charge density n($\mathbf{r}$) that minimizes the energy of system is assumed to be in close neighborhood of the charge density $n_o(\mathbf{r})$ of free and neutral atoms. For multi-atom system, n($\mathbf{r}$) = $n_o(\mathbf{r})$ + δn($\mathbf{r}$), $\delta n(\mathbf{r})$ being small. Expanding E[n] at n_o to second-order in fluctuations $\delta n(\mathbf{r})$, the energy becomes:

$$\begin{aligned} E[\delta n] \approx & \sum_a f_a \langle \psi_a | -\frac{1}{2}\nabla^2 + V_{ext} + V_H[n_o] + V_{xc}[n_o] | \rangle \\ & + \frac{1}{2} \int \int' \left(\frac{\partial^2 E_{xc}[n_o]}{\partial n \partial n'} + \frac{1}{|\mathbf{r} - \mathbf{r}'|} \right) \partial n \partial n' \\ & - \frac{1}{2} \int V_H[n_o](\boldsymbol{r}) n_o(\boldsymbol{r}) + E_{xc}[n_o] + E_{II} - \int V_{xc}[n_o](\boldsymbol{r}) n_o(\boldsymbol{r}) \end{aligned} \tag{2.34}$$

where $f_a \in [0,2]$ is the occupation of a single-particle state ψ_a with energy E_a. The total energy $E[n]$ in DFTB involves band-structure energy

(E_{BS}) with no charge transfer, energy due to charge fluctuations primarily from Coulomb interactions and xc-contributions (E_{Coul}), and repulsive energy (E_{rep}), as expressed in Equation 2.34 with terms in first, second and third line respectively. Thus, the quality and transferability in DFTB is determined by E_{BS}, E_{Coul}, and the chosen structures for fitting the parameters of repulsive potentials E'_{rep} with respect to inter-atomic distance R_{IJ} [66].

The Hartree term $\left(-\frac{1}{2}\int\int \frac{n_o(\boldsymbol{r})n_o(\boldsymbol{r'})}{|\mathbf{r}-\mathbf{r}'|}d^3r d^3r' \right)$ of the repulsive energy is computed by dividing the total volume into atomic volumes, and the sum is computed over atom pairs taking into account the atomic number and inter-atomic distances, since $n_o(\mathbf{r})$ is spherically symmetrical for free atoms. Similarly, the ion-ion repulsions (E_{II}) can be approximated taking into account each pair of atoms depending only on the atomic number. Further, the E_{rel} includes on-site contributions from each atom depending only on $n_o(\mathbf{r})$, and thus introduce a shift in total energy by a constant value.

The energy as a function of charge fluctuation (δn) corresponding to Coulomb and *xc*-interactions involves double integrals over the space. In order to convert the integral into sum over atomic pairs IJ, electronic fluctuations over the space are decomposed into atomic contributions by considering volumes v_I and computing atomic-charge fluctuations Δq_I as:

$$\Delta q_I \approx \int_{v_1} \delta n(\boldsymbol{r}) d^3r \tag{2.35}$$

and the total charge fluctuations $\delta n(\boldsymbol{r})$ is:

$$\delta n(\boldsymbol{r}) = \sum_I \Delta q_I \delta n_I(\boldsymbol{r}) \tag{2.36}$$

The on-site energy, i.e. $I = J$, depends on Hubbard U, which is the difference between ionization energy (IE) and electron affinity (EA), as $\frac{1}{2}U_I\Delta q_I^2$.

For $I \neq J$, the Coulomb energy $\mathrm{E}_{coul}[\delta \mathrm{n}]$ depends on electrostatic interactions as:

$$\frac{1}{2}\Delta q_I \Delta q_I \int_{v_I}\int_{v_J}' \frac{\delta n_I \delta n_J'}{|\mathbf{r}-\mathbf{r}'|} \tag{2.37}$$

between $\Delta \mathrm{q}_I \mathrm{q}_J$, with an assumption that charge fluctuations about each atom I, $\delta \mathrm{n}_I$ are spherically symmetrical and generally modeled using a Gaussian profile. Hence, energy due to Coulomb interactions between the atoms can be estimated from fluctuations in the charge distributions $\delta \mathrm{n}_I(\mathbf{r})$ of each atom I.

To model the repulsive energy due to core tightly bound electrons, TB approach employs minimal localized radial basis, typically real spherical harmonics. With these basis functions $\{\phi\}$, the band structure energy E_{BS} then becomes

$$E_{BS} = \sum_a f_a \sum_{\mu\nu} c_\mu^{a*} c_\nu^a H_{\mu\nu}^o, \tag{2.38}$$

where, $H_{\mu\nu}^o = \langle \phi_\mu | H^o | \phi_\nu \rangle$. The matrix elements $\mathrm{H}_{\mu\nu}^o$ are the relevant parameters in the TB approach.

The atomic charges q_I in terms of $\{\phi\}$ are expressed as:

$$q_I = \frac{1}{2}\sum_a f_a \sum_{\mu\nu} c_\mu^{a*} c_\nu^a S_{\mu\nu} \tag{2.39}$$

where, $S_{\mu\nu}^o = \langle \phi_\mu | \phi_\nu \rangle$ such that such that μ belongs to I and ν to some other atom J, signifying overlap of non-orthogonal orbitals. The fluctuations in atomic charges $\Delta q_I = q_I - q_I^o$, where q_I^o is the number of valence electrons in

the neutral atom.

The total energy expression that includes E_{BS}, E_{Coul} and E_{rep} becomes:

$$E = \sum_a f_a \sum_{\mu\nu} c_\mu^{a*} c_\nu^a H_{\mu\nu}^o + \frac{1}{2} \sum_{IJ} \gamma_{IJ}(R_{IJ}) \Delta q_I \Delta q_J + \sum_{I<J} V_{rep}^{IJ}(R_{IJ}) \quad (2.40)$$

Here, $\gamma_{IJ}(R_{IJ}) = \int_{v_1} \int'_{v_J} \frac{\partial n_I \partial n'_J}{|\mathbf{r}-\mathbf{r}'|} = \frac{\boldsymbol{erf}(C_{IJ}R_{IJ})}{R_{IJ}}$ for a spherical symmetric Gaussian charge distribution. Thus, formulation of DFTB largely involves estimating of matrix elements $\mathrm{H}_{\mu\nu}^o$ and $\mathrm{S}_{\nu\mu}$ and repulsive potentials $V_{rep}^{IJ}(R_{IJ})$.

2.6.1 Estimation of matrix elements $\mathbf{H}_{\mu\nu}^o$ and $\mathbf{S}_{\mu\nu}$

In TB approach, minimal basis functions $\phi_\nu = R_\nu(r)\tilde{Y}_\nu(\theta,\phi)$ used for the expansion of electronic eigenstates [66], are not the atomic orbitals of free atoms but are localized basis functions, but are obtained by introducing a spherically symmetric confinement potential of the form $\mathbf{r}^{2i}$, i > 1. These localized orbitals are used to calculate the overlap matrix elements $\mathrm{S}_{\nu\mu}$ for orbital pairs ν and μ given by:

$$S_{\mu\nu} = \int \phi_\mu^*(\boldsymbol{r}) \phi_\nu(\boldsymbol{r}) d^3r \quad (2.41)$$

The overlap matrix obtained is real and symmetric. For orbitals belonging to different atoms, the integral in Equation 2.41 is computed by considering ϕ_ν at $\mathrm{R}_I = 0$ and ϕ_μ at $\mathrm{R}_J = \mathrm{R}$. The dependence on R_{IJ} is incorporated by Slater-Koster transformation rules [67]. The Hamiltonian matrix element $\mathrm{H}_{\mu\nu}^o$ for basis states μ and ν is given by:

$$H^o_{\mu\nu} = \int \phi^*_\mu(\mathbf{r}) \left(\frac{1}{2}\nabla^2 + V_s[n_o] \right) \phi_\nu(\mathbf{r}) \tag{2.42}$$

where, the effective potential $V_s[n_o](\mathbf{r}) = \mathbf{V_{ext}}(\mathbf{r}) + \mathbf{V_H}(\mathbf{r}) + \mathbf{V_{xc}}(\mathbf{r})$ is computed at neutral density $\mathrm{n}_o(\mathbf{r})$ of the system. The diagonal elements $H^o_{\mu\mu}$ are approximately equal to the eigen-energies of the free-atom orbitals. With the off-diagonal matrix elements $H^o_{\mu\nu}$ for μ localized around I and ν around J, and the contributions from other atoms assumed to be small, $H^o_{\mu\nu}$ can be evaluated from the potential $V_s[n_o](\mathbf{r}) = \mathbf{V_{s,I}}[\mathbf{n_o}, \mathbf{I}](\mathbf{r}) + \mathbf{V_{s,J}}[\mathbf{n_o}, \mathbf{J}](\mathbf{r})$, where $V_{s,I}[n_o, I](\mathbf{r})$ is the Kohn-Sham potential corresponding to atomic density.

2.6.2 Estimation of repulsive interactions

The repulsive term V_{rep} is reminiscent to E_{xc} in DFT in the sense that both embed details of electronic interactions that dictate the nature of chemical bonds. DFTB uses a set of structures, namely dimers, trimers, polyhedra etc, with different chemical environments obtained using DFT. The difference in forces $|F_{DFT} - F_{DFTB}|$ are minimized, and the fitting parameters are obtained. Generally, smoothing splines or low-order polynomials are chosen for repulsive functions $\mathrm{V}_{rep}(\mathbf{r})$. These functions computed from the fitted parameters are required to be short-ranged, monotonic and smooth for transferability and performance of DFTB in simulation of an unknown structure.

Chapter 3

Origin of structural flexibility of crystals: soft and hard vibrations acting *in sync*

3.1 Introduction

Flexibility of a solid is a term referred ubiquitously to describe its tendency to accommodate changes in shape, size or its form on external perturbation, without compromising structural identity. In proteins, it is known in the context of their ability to respond to environmental changes while retaining their chemical structure [68–70]. In low-density porous framework solids with weak interactions between their isostatic rigid building units, flexibility is associated with a density window [71] in which their polyhedral structure remains intact [72] as the structure undergoes conformational changes, the latter determined by topological features namely, degrees of freedom and

number of constraints at the junctions between rigid units [47,73]. While this refers to the tendency of a material/solid to allow internal structural reorientations in response to homogeneous strains through low-frequency phonon modes [44, 74], the precise measure of flexibility is currently lacking and its origin in the microscopic degrees of freedom constrained by symmetry is unclear [75].

One approach to understand structural flexibility is through *intuitively* analogous physical property of the liquid state: flowability [76, 77]. With a plethora of low-energy internal DoFs in liquid, it readily undergoes structural rearrangements when subjected to shear strain, while maintaining the local-coordination and symmetry (in this case, P1) at each site. An ordered crystalline solid, however, is the consequence of spontaneously broken continuous translational and rotational symmetries, and is characterized by Goldstone bosons [14] manifesting as longitudinal and transverse phonons. Its long-range order constrains the atoms (or molecules) of a crystal to maintain *a well-defined spatial arrangement*, giving rise to a finite restoring force (internal stress) against an external perturbation $\bar{\boldsymbol{\epsilon}}$, resulting in a non-zero rigidity (slope of transverse acoustic phonons) [78]. Because of the finite elastic moduli, viz. shear rigidity and bulk modulus, there is accumulation of structural stresses in the presence of homogeneous strains, eventually resulting in either plastic deformation or phase change (as in ductile metals) or rupture (as in brittle solids or glasses). An alternative mechanism of elastic softening, which circumvents structural disintegration and phase transformations, through internal structural rearrangements reminiscent to liquids (or glasses) is, presented here as, the structural flexibility (see Figure 3.1 for

illustration).

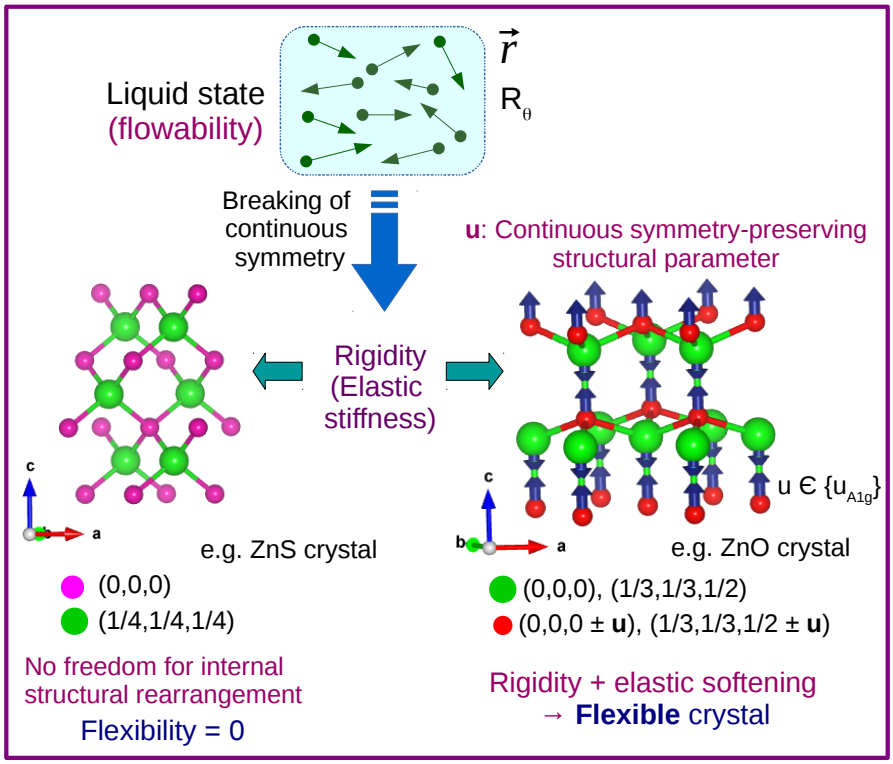

Figure 3.1: (Color online) Schematic for structural flexibility.

3.2 Results and Discussion

We first present a quantitative measure of structural flexibility ($\bar{\boldsymbol{F}}^{\boldsymbol{s}}$ tensor) of a crystalline material as the fractional release of elastic stress or strain-energy upon internal structural rearrangements through symmetry-preserving normal modes of homogeneously deformed structure, isomorphic to symmetry-preserving vibrations with identity (Γ_1) representation. Illustrating mechanical responses of structurally distinct classes of crystals $\mathbf{C}$ with

hydro-static (ϵ_h) and rhombohedral (ϵ_r) strains as the prototypic perturbations, we unravel that symmetry-preserving modes of deformed crystals $\mathbf{C}$ allow $0 < \bar{\boldsymbol{F}}^{\boldsymbol{s}} < 1$, rendering intrinsic flexibility to a crystal (as shown in ZnO, ZIF-8, MOF-5 and ZrW_2O_8). ZnO, with a simple wurtzite structure and a single mode with Γ_1 representation in its parent phase, represents an appropriate model crystal to understand the concept of structural flexibility F_i^s. Metal-organic frameworks (MOFs) form a class of ordered, crystalline nanoporous materials consisting of metal-centered polyhedra, connected through organic linkers. With diverse topologies and secondary-building units, MOFs are classified as rigid or flexible. While ZIF-8 is known to be *flexible*, MOF-5 is considered rigid [44, 79]. ZrW_2O_8 is an interesting crystal that exhibits negative thermal expansion driven by soft normal modes, and thus is highly *flexible*. Structural details of these crystals is provided in Chapter 1. From the analysis of bond stiffness matrix (inter-atomic force constants) of these materials, we highlight that, in addition to large structural rearrangements, analogous to flowability of liquids, flexibility of solids greatly involves release of strain energy or stresses through coupling of symmetry-preserving optical modes with the strain-field. Through the interplay of symmetry-preserving modes spanning broad range of energies, structural flexibility of a crystal induces elastic softening, allowing it to accommodate large homogeneous strain.

Flexibility is associated with the ability of a *solid* to accommodate homogeneous deformation through internal displacements (optical phonons), *without* a phase transition or loss of structural integrity. To quantify this property, we define a dimensionless *structural flexibility tensor*, $\bar{\boldsymbol{F}}^{\boldsymbol{s}} \in [0,1]$

for uniform strain tensor $\bar{\boldsymbol{\epsilon}}$ applied to a reference crystal $\mathbf{C}_{Ref}$ ($\epsilon = 0$, $\vec{d} = 0$) such that a component $F^s{}_i$ for strain ϵ_i is:

$$F^s{}_i = \frac{E_o(\epsilon_i, \vec{d} = 0) - E_{relax}(\epsilon_i, \vec{d} = \vec{d}_{relax})}{E_o(\epsilon_i, \vec{d} = 0) - E_{ref}(\bar{\boldsymbol{\epsilon}} = 0, \vec{d} = 0)} \tag{3.1}$$

where, $\mathrm{E}_o(\epsilon_i, \vec{d} = 0)$ is the energy of a strained structure with no internal relaxation and $\mathrm{E}_{relax}(\epsilon_i, \vec{d} = \vec{d}_{relax})$ is its energy after relaxation to minimum-energy state. Since F^s_i is the fractional release of strain-energy of uniformly deformed crystal $\mathbf{C}$ through internal displacements that maintain its space-group symmetry $\mathbf{G}$, projection of $\vec{d}_{relax}$ (that is, $\Delta\vec{s} = d_{l\alpha}$, a ($3N$x1) vector quantifying change in internal structure, see Methods) onto normal modes $\{\hat{u}_{\nu\vec{q}=0}\}$ is non-zero only for $\nu \in \{A_{1g}\}$ of the strained crystal $\mathbf{C}$.

In the harmonic approximation, the energy E, in terms of homogeneous strain ϵ_i (here, hydrostatic strain ϵ_h and rhombohedral strain ϵ_r) and internal displacements $\{u_\nu\}$, is:

$$E(\epsilon_i, \{u_\nu\}) = \frac{1}{2} C^{bare} \epsilon_i^2 + \sum_\nu \left(g_\nu \epsilon_i u_\nu + \frac{1}{2} K_\nu u_\nu^2 \right) \tag{3.2}$$

where, C^{bare} is the un-relaxed elastic modulus of the reference crystal $\mathbf{C_{ref}}$ [80] relevant to the component of applied strain-tensor, K_ν is the spring constant of mode ν, obtained from the eigen-spectrum of second-order force-constant matrix, and g_ν is the first-order coupling-strength of ν with ϵ_i. Minimization of E with respect to u_ν gives $u_\nu = \frac{-g_\nu \epsilon_i}{K_\nu}$. Substituting u_ν in Equation 3.2, the flexibility arising from a symmetry-preserving mode $F^s_i(\nu)$ $= \frac{(g_\nu)^2}{C^{bare} K_\nu}$. Since the response $\frac{\partial u_\nu}{\partial \epsilon_i}$ determines the spatial extent of internal

structural rearrangements through a mode ν with ϵ_i and $g_\nu = -K_\nu \frac{\partial u_\nu}{\partial \epsilon_i}$, $F_i^s(\nu)$ is re-written as:

$$F_i^s(\nu) = \frac{K_\nu (\frac{\partial u_\nu}{\partial \epsilon_i})^2}{C^{bare}} \tag{3.3}$$

and the structural flexibility of a crystal is $F_i^s = \sum_\nu F_i^s(\nu)$, where the sum is over the set of Γ_1 modes in the homogeneously deformed crystal $\mathbf{C}$. While for ϵ_h, $\mathbf{C} = \mathbf{C}_{ref}$, that is, the crystal-symmetry is maintained on hydrostatic strains, the shear-deformed crystal $\mathbf{C} = \bar{\boldsymbol{D}}\mathbf{C}_{ref}$, where $\bar{\boldsymbol{D}}$ is the deformation-gradient tensor with $\epsilon_{ii} = 0$, and $\epsilon_{ij} \neq 0$, typically has a lower symmetry. Transformation of $\mathbf{C}_{ref}$ in accordance with irreducible representation matrix (or symmetry label) isomorphic to $\bar{\boldsymbol{D}}$ maps it onto the deformed crystal $\mathbf{C}$. For instance, T_{2g} irrep of O_h group maps the cubic structure ($Fm\bar{3}m$ symmetry) onto $\mathbf{C}$ in response to rhombohedral shear strain. Lower the symmetry of $\mathbf{C}$, larger is the set of symmetry-preserving modes in $\mathbf{C}$ (see the number of Γ_1 modes of strained crystals $\mathbf{C}$ considered here in Table 3.1 [17]).

Clearly, Equation 3.3 indicates that a competition between a mode with large stain-phonon coupling, $g_\nu = -K_\nu \frac{\partial u_\nu}{\partial \epsilon_i}$, and un-relaxed elastic modulus C^{bare} determines the structural flexibility F_i^s, upto first-order. This definition also represents a fractional release of stresses on structural optimization. Hence, in terms of a component of elastic modulus tensor, F^s = 1-$\frac{C_{ij}^{rel}}{C_{ij}^{bare}}$, clearly corroborating the intuitive notion of flexibility emerging from soft *relaxed* elastic modulus C_{ij}^{rel} [81].

To illustrate the concept of flexibility given in Equation 3.3, we present $\bar{\boldsymbol{F}}^{\boldsymbol{s}}$ with respect of hydrostatic and rhombohedral strains ($F^s{}_h$ versus ϵ_h

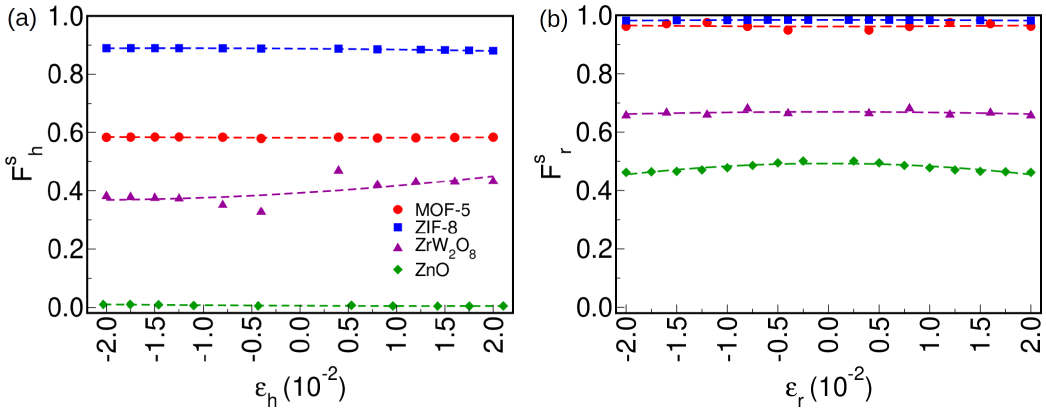

Figure 3.2: Illustration of quantitative measure of flexibility of ZIF-8, MOF-5, ZrW_2O_8 and ZnO crystals with respect to (a) hydrostatic strain ϵ_h, and (b) rhombohedral shear strain ϵ_r. In general, F^s_r is higher than F^s_h for all crystals.

and $F^s{}_r$ versus ϵ_r) for structurally disparate crystalline systems viz. ZnO, ZIF-8, MOF-5 and ZrW_2O_8 (see Figure 3.2a and b). Quite evidently, the structural flexibility F^s_i shows wide variation across the materials considered here, and the perturbations (ϵ_h and ϵ_r) applied. Further, while F^s_h is essentially constant for ZIF-8, MOF-5 and ZnO over the considered range of strains, $\epsilon_i \in$(-0.02 to 0.02), the expansion-compression asymmetry in F^s_h of ZrW_2O_8 originates primarily from *non-linear* elastic behavior (i.e. strain derivatives of B^{bare}) as well as anharmonic (i.e. phonon-phonon coupling) contribution to E_{relax}. These aspects are not pursued here and will be the undertaken in the future.

To understand the origin of the large differences in $\bar{\boldsymbol{F}}^{\boldsymbol{s}}$, or the measure of fractional release in strain energies or structural stresses with respect to homogeneous strains, we first determined the *bare* elastic moduli, viz. bulk modulus B^{bare} and shear modulus C^{bare}_{44}, upto second order, for each of the

materials considered (see Table 3.1). Quite evidently, C_{44}^{bare} is lower than B^{bare} for all the crystals, indicating a generic tendency of higher flexibility on application of rhombohedral shear strain ϵ_r, which breaks the symmetry of the reference crystal $\mathbf{C}_{ref}$.

Table 3.1: Bare elastic moduli and number of symmetry-preserving phonons of the crystals considered in this study

	B^{bare} (GPa)	C_{44}^{bare} (GPa)	$N_{A_{1g}}(\epsilon_h)$	$N_{A_{1g}}(\epsilon_r)$
MOF-5	38.2	29.7	9	78
ZIF-8	83.8	72.8	18	79
ZrW_2O_8	154.8	84.6	11	107
ZnO	128.3	87.9	1	7

A rather high value of F_i^s of ZIF-8 with both hydrostatic and shear strains, despite its large *bare* elastic moduli than of MOF-5, indicates that internal strains (u_ν) dominate its structural flexibility. This applies also to ZrW_2O_8, which exhibits significantly higher flexibility than ZnO. Quite clearly, ZIF-8 derives its higher hydrostatic flexibility F_h^s from the larger set of symmetry-preserving modes, and ZnO, with a single Γ_1 phonon in its $P6_3mc$ phase, possesses a non-zero F_h^s, albeit with a very small value of $\sim$0.01. Increase in the number of symmetry-preserving degrees of freedom gives rise to a larger F_r^s of ZnO ($\sim$ 0.45) with respect to ϵ_r (see Table 3.1 and Fig. 3.2). Counter-intuitively, ZrW_2O_8, with 11 Γ_1 irreps, as against 9 modes in MOF-5, shows a relatively lower value of F_h^s (see Fig. 3.2a). This stems from its value of B^{bare} ($\sim$ 155 GPa), which is about 4 times as that of MOF-5. In addition to a lower C_{44}^{bare} with respect to B^{bare} of each material, a larger set of symmetry-preserving modes in shear-deformed structure gives rise to greater

shear flexibility F_r^s. While flexibility of a crystal is thus not directly related to *bare* elastic moduli, the foregoing analysis distinctly highlights the role of symmetry-preserving irreps as the primary source of non-trivial flexibility.

To understand in detail the origin of $\bar{\boldsymbol{F}}^{\boldsymbol{s}}$, precise contributions of each symmetry-preserving mode ν to flexibility F_i^s of $\mathbf{C}$ (using Equation 3.3) can to be determined (see Tables 2-9 for K_ν, $\frac{\partial u_\nu}{\partial \epsilon_i}$ and $\mathrm{F}^s(\nu)$ of the Γ_1 modes with contributions greater than 1% to total flexibility F^s of the the four materials with respect to ϵ_h and ϵ_r). While soft modes (weak spring constants i.e. low K_ν), in general, dominate the atomic displacements (i.e large $\frac{\partial u_\nu}{\partial \epsilon_i}$) in response to homogeneous strains, these modes are not the primary contributors to F^s (see Tables 2-9). Flexibility, which is defined as the fractional release in energy or stress due to internal structural arrangements, can predominantly originate from stronger *springs* (i.e. larger K_ν), due to large coupling of these modes with homogeneous strain ϵ_i ($g_\nu = K_\nu \frac{\partial u_\nu}{\partial \epsilon_i}$). Thus, a structure that encompasses low-energy modes which support internal rearrangements at the atomic scale, and higher-frequency vibrations which *absorb* a rather large fraction of energy through stronger strain-phonon coupling strength, exhibits high flexibility. This is in stark contrast to widely-accepted concept of flexibility and its origin solely in low-frequency modes [44, 82]. Quite interestingly, the *co-operating* soft and hard modes and their contributions to structural rearrangements and flexibility respectively is well-corroborated in all crystals considered here (ZIF-8, ZrW_2O_8, MOF-5 and ZnO) with ϵ_r. While this holds for ZIF-8 and ZrW_2O_8 in response to ϵ_h, softest symmetry-preserving mode of MOF-5 shows a rather low $\frac{\partial u_\nu}{\partial \epsilon_h}$ (see Fig.), signifying a lack of low-energy modes that allow structural rearrangements. Further, in

comparison to ZIF-8, these modes of MOF-5 show a rather limited response to ϵ_h due to smaller internal strains ($\frac{\partial u_\nu}{\partial \epsilon_h}$) allowed along each mode, thus corroborating its low flexibility (or rigidity) [47, 79]. Vanishingly low F_h^s of ZnO arises from a single high-energy Γ_1 mode ($K_\nu = 11.8$ eV/$\mathring{A}^2$, see Figure 3.1) that couples very weakly with ϵ_h.

To determine whether the nature of modes that contribute to flexibility are specific to a material-system or show certain common features, we filter-out the two sets of symmetry-preserving modes of ZIF-8, MOF-5 and ZrW_2O_8 under strain ϵ_h and ϵ_r, one, that dominate structural rearrangements, and two, that contribute dominantly to flexibility F_i^s (see Fig. 3.3, 3.4, 3.5). Low-energy modes that assist in internal structural rearrangements represent linker rotations, commonly known as breathing modes (as in ZIF-8 and MOF-5) (see top panels of Fig. 3.3 and 3.4) [44, 73], liberations of WO_6 octahedra (as in ZrW_2O_8) (see top panels of Fig. 3.5) [42], and shearing of constituent tetrahedra (as in ZnO). Quite invariably, the high-energy modes (see bottom panel of Fig. 3.3, 3.4, 3.5) exhibit stretching or twisting modes of molecular entities of the crystals [83].

With a sound understanding of emergence of structural flexibility from high-energy symmetry-preserving modes of uniformly deformed crystal $\mathbf{C}$, we now illustrate its fundamental aspect in terms of elastic softening, both bulk modulus and shear rigidity. Elastic moduli of a crystal, which are the consequence of broken continuous symmetry of liquids, manifests as Goldstone modes (two transverse branches and one longitudinal branch with positive slopes) of solids. Crystals with certain symmetries, as considered in the

present study, host a finite number of symmetry-preserving modes that couple with homogeneous strain ϵ_i, constituting continuous internal symmetry-preserving degrees of freedom, denoted by $u_{A_{1g}}$. Response of $u_{A_{1g}}$ through structural relaxation causes release of strain-energy and elastic softening, that counters the emergent modulus of a crystal, and is termed here as structural flexibility F^s. Quite clearly, higher the F^s, larger is the energy (or stress) release, softer the *relaxed* elastic modulus C_{ij}^{rel} [81]. Thus, optical modes, though their coupling with acoustic modes, are pertinent to the flexibility of a crystal. The concept of flexibility presented here applies to any long-range ordered state arising from broken-continuous symmetry, like electronic polarization or magnetization.

Methods:

The internal strains, or atomic displacements $\{\vec{d}_{relax}\}$ can be represented as a $(3N\text{x}1)$ vector $\Delta\vec{s} = d_{l\alpha}$, where $d_{l\alpha} = f_{l\alpha}$ - $i_{l\alpha}$, $f_{l\alpha}$ and $i_{l\alpha}$ being reduced (crystal) atomic coordinates of l^{th} atom in α-direction of relaxed and unrelaxed structures, respectively. Projections onto normal modes of crystal is expressed as: $\Delta\vec{s} = \sum_{\nu\in\{A_{1g}\}}(\Delta\vec{s}.\hat{u}_\nu)\hat{u}_{\nu\vec{q}=0}$. Here, $\{\hat{u_\nu}\}$ are the normalized eigen-displacements ($\vec{u}_{\nu\vec{q}} = \frac{\vec{e}_{l\vec{q}}}{\sqrt{M_l}}$) of symmetry-preserving phonons of $\mathbf{C}$, and $\vec{q} = 0$ is omitted for brevity.

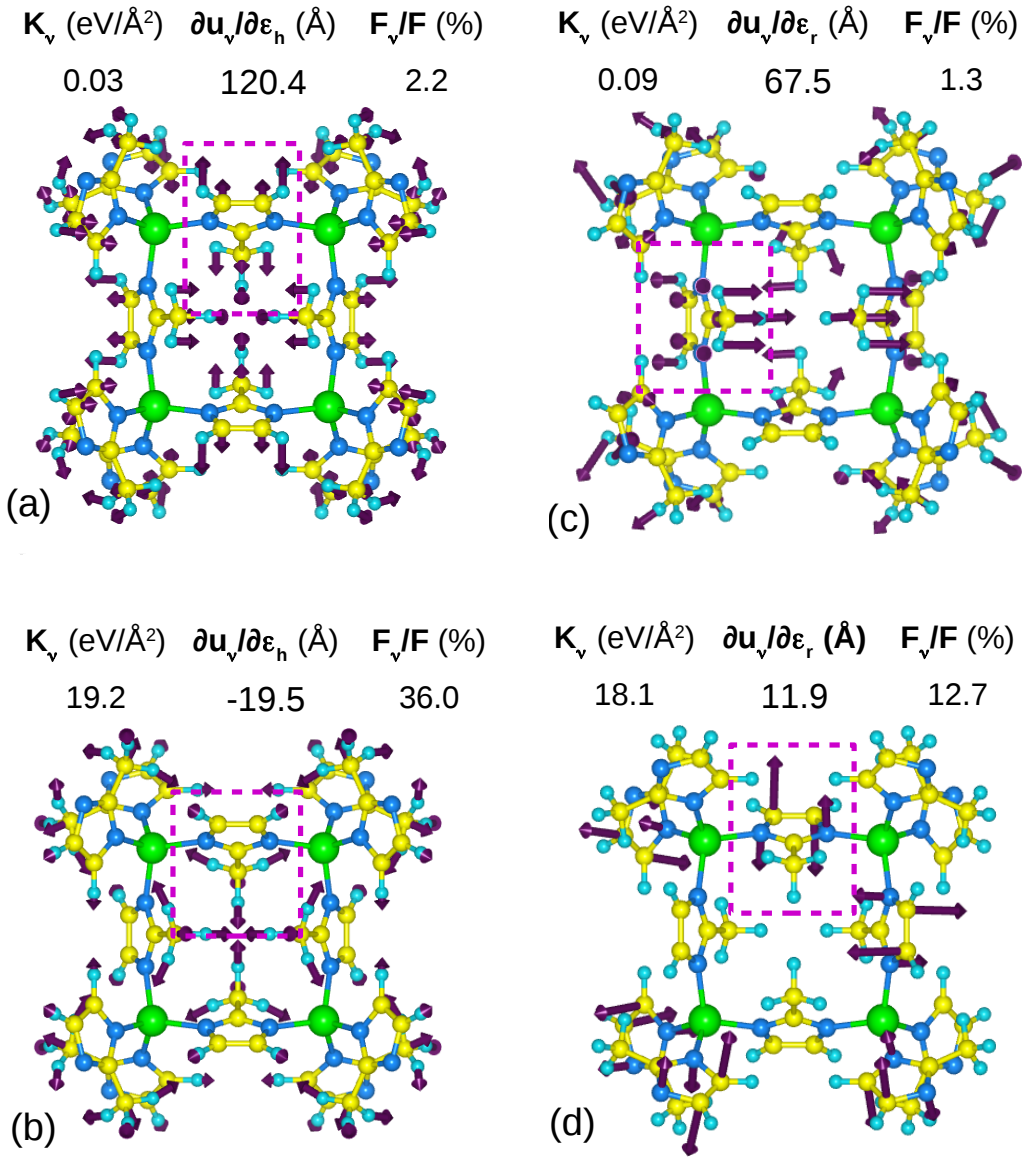

Figure 3.3: Symmetry-preserving modes and flexibility of ZIF-8 crystal with respect to homogeneous strain ϵ_h (left panel) and ϵ_r (right panel): low-energy modes that allows large structural rearrangement (upper panel; (a) and (c)) and high-energy modes that dominate flexibility (lower panel; (b) and (d)). Soft modes (a) and (c) represent rotation of IM-linkers. Hard modes denote stretching vibrations, as in (b), with respect to ϵ_h; and twisting of IM ring, as in (d), with respect to ϵ_r.

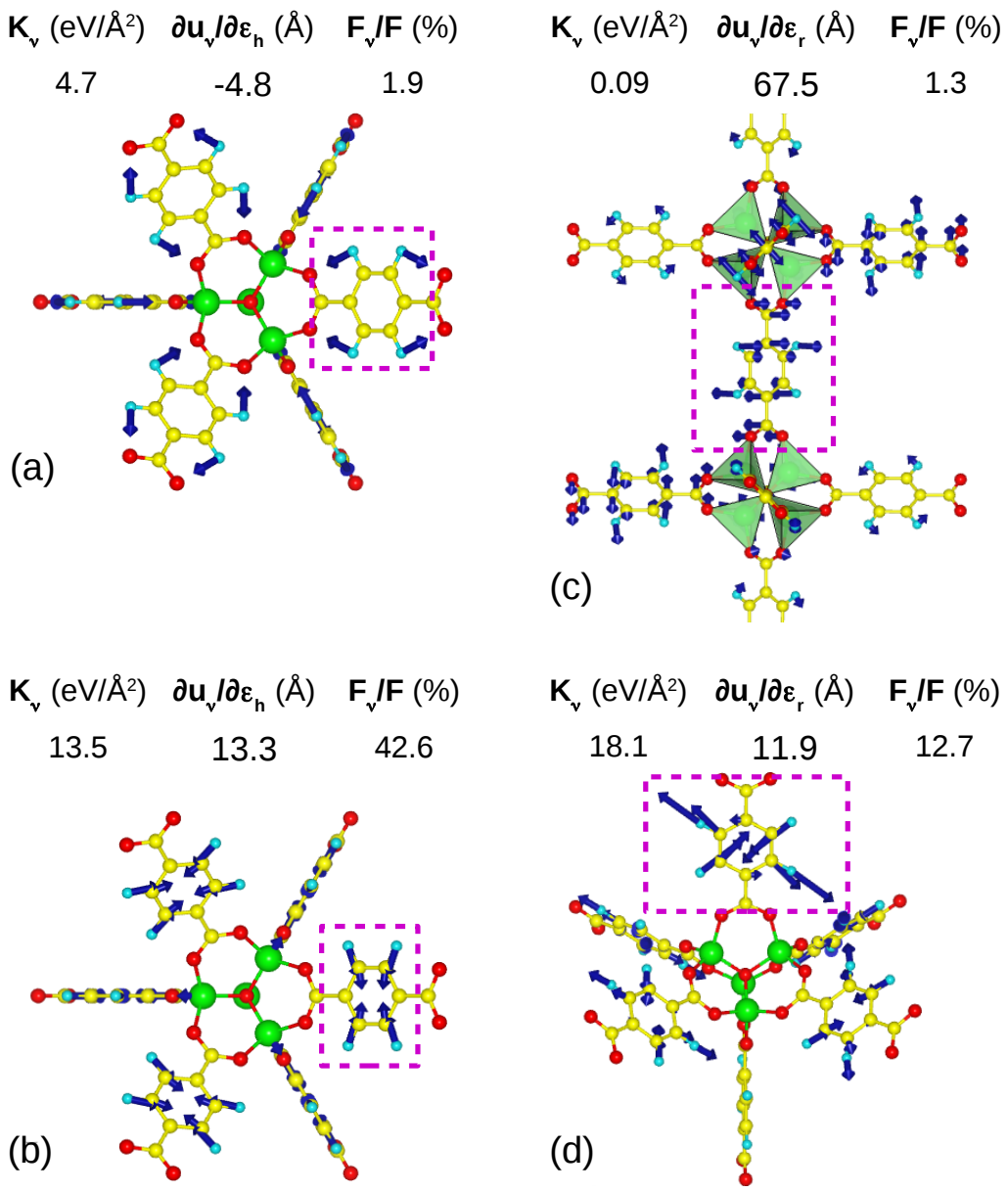

Figure 3.4: Symmetry-preserving modes and flexibility of MOF-5 crystal with respect to homogeneous strain ϵ_h (left panel) and ϵ_r (right panel): unlike soft modes in ZIF-8, low-energy mode with respect to ϵ_h, as in (a) does not support large structural rearrangement, i.e. low $\frac{\partial u_\nu}{\partial \epsilon_h}$, and denote rotation of C-H bonds of benzene linker. Here, higher-energy mode dominates internal strain and flexibility, as in (b), and exhibit change in bond-lengths of linker. Response to ϵ_r is similar to that in ZIF-8; low K_ν, large $\frac{\partial u_\nu}{\partial \epsilon_r}$, as in (c), and large K_ν exhibits high F_ν, as in (d). While the former represents liberation of BDC-group, latter is linked to distortion of benzene-group.

Table 3.2: Relative contributions of symmetry-preserving modes of ZIF-8 to its F_h^s with respect to hydrostatic strain ϵ_h

K_ν $(\frac{eV}{\mathring{A}^2})$	$\frac{\partial u_\nu}{\partial \epsilon_h}$ $(\mathring{A})$	F_ν (%)
19.21	-19.54	36.0
6.57	25.74	21.4
118.01	3.69	7.9
101.32	3.82	7.2
0.30	-60.88	5.5
51.23	-4.11	4.2
4.50	13.87	4.2
0.49	41.50	4.1
32.59	-4.38	3.1
71.28	-2.60	2.4
0.03	120.38	2.1

Table 3.3: Relative contributions of symmetry-preserving modes of ZIF-8 to its F_r^s with respect to rhombohedral shear strain ϵ_r

K_ν $(\frac{eV}{\mathring{A}^2})$	$\frac{\partial u_\nu}{\partial \epsilon_h}$ $(\mathring{A})$	F_ν (%)
18.05	11.87	8.1
12.37	11.85	5.5
18.09	-9.04	4.7
24.71	-7.13	4.0
12.37	9.94	3.9
71.52	4.07	3.8
109.23	3.21	3.6
0.72	38.23	3.3
74.63	-3.65	3.1
51.58	4.03	2.6
6.80	10.81	2.5
120.56	-2.51	2.4
6.57	-10.17	2.2
109.23	-2.42	2.0

Table 3.4: Relative contributions of symmetry-preserving modes of MOF-5 to its F_h^s with respect to hydrostatic strain ϵ_h

K_ν $(\frac{eV}{\mathring{A}^2})$	$\frac{\partial u_\nu}{\partial \epsilon_h}$ $(\mathring{A})$	$\frac{F_\nu}{F}$ (%)
13.48	13.28	42.6
31.01	6.50	23.5
98.53	-3.21	18.2
19.00	4.98	8.4
8.65	4.22	2.8
52.75	-1.51	2.2
4.74	-4.77	1.9

Relative contributions of symmetry-preserving modes of MOF-5 to its F_r^s with respect to rhombohedral shear strain ϵ_r

K_ν $(\frac{eV}{\mathring{A}^2})$	$\frac{\partial u_\nu}{\partial \epsilon_h}$ $(\mathring{A})$	$\frac{F_\nu}{F}$ (%)
12.58	9.62	20.0
9.27	12.29	12.9
123.72	2.53	7.3
0.66	-31.52	6.1
96.88	2.32	4.8
30.17	-4.13	4.8
9.27	7.30	4.6
123.72	-1.80	3.7
96.88	-1.88	3.2
5.47	-7.59	2.9
2.12	-11.66	2.6
30.17	3.05	2.6
12.58	-4.66	2.5

Table 3.5: Relative contributions of symmetry-preserving modes of ZrW_2O_8 to its F_h^s with respect to hydrostatic strain ϵ_h

K_ν $(\frac{eV}{\mathring{A}^2})$	$\frac{\partial u_\nu}{\partial \epsilon_h}$ $(\mathring{A})$	F_ν (%)
57.86	4.30	40.5
11.20	4.85	30.1
92.94	-2.00	17.1
53.46	1.59	5.1
19.00	1.71	2.1
6.48	2.54	1.6
2.78	-3.21	1.1
1.46	-3.92	0.8
0.81	5.20	0.8
0.52	5.65	0.6

Table 3.6: Relative contributions of symmetry-preserving modes of ZrW_2O_8 to its F_r^s with respect to rhombohedral shear strain ϵ_r

K_ν $(\frac{eV}{\mathring{A}^2})$	$\frac{\partial u_\nu}{\partial \epsilon_h}$ $(\mathring{A})$	F_ν (%)
92.89	3.42	29.9
73.23	-2.98	17.9
92.89	1.69	7.3
92.89	-1.47	5.5
0.61	16.53	4.6
8.19	4.47	4.5
0.30	18.11	2.8
21.67	-2.10	2.6
8.19	3.41	2.6
2.37	6.17	2.5

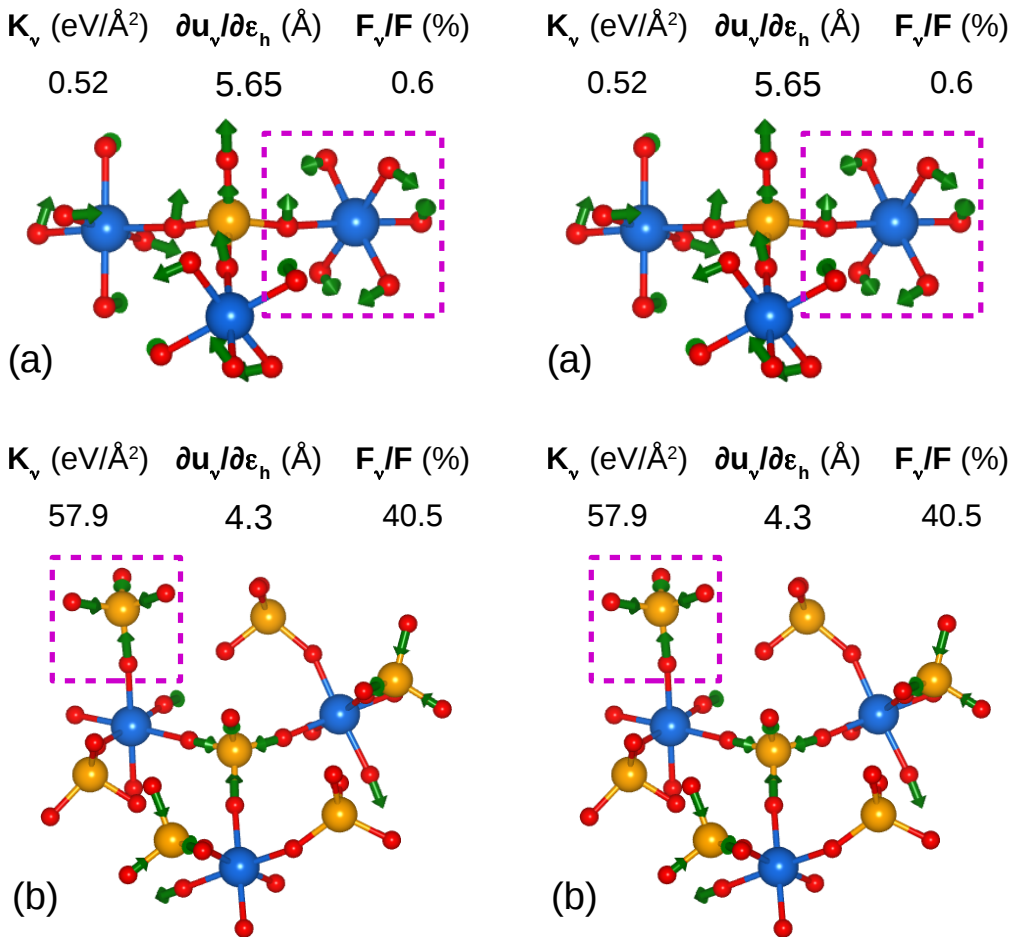

Figure 3.5: Symmetry-preserving modes and flexibility of ZrW_2O_8 crystal with respect to homogeneous strain ϵ_h (left panel) and ϵ_r (right panel): low-energy modes that allows large structural rearrangement (upper panel; (a) and (c)) and high-energy modes that dominate flexibility (lower panel; (b) and (d)).

Chapter 4

Twist without *split*: Mechanism of amorphization of MOF-5 at ultra-low pressures

4.1 Introduction

In the last three decades, MOFs have emerged as a class of technologically relevant crystalline materials, essentially because of their porous structure with large pore-size and ultra-high surface area in their *pristine* form [84]. Constructed rationally from molecular polyhedra, directed by *rigid* secondary building units (SBUs), and connected by a variety of organic linkers, MOFs exhibit a plethora of blueprint-target structural networks and properties [85]. This inherent reticular design gives rise to a large number of inter-molecular degrees of freedom (DoFs) [86,87] within a periodic unit of MOFs, permitting

a range of structural conformations in response to external strains [88]. Low-frequency atomic vibrations associated with linker rotations, or bond-bending and buckling [89] contribute predominantly to vibrational entropy or lattice disordering of MOFs, leading to their structural phase-transition or amorphization. The SBUs, however, have been widely accepted to impart elastic rigidity, robustness and directionality to their extended three-dimensional network [1, 34].

Amorphization of MOFs, as characterized by the loss of long-range order of crystalline structure, is generally detrimental to their porosity [48, 90, 91]. Certain MOFs, for instance ZIF-4, undergo reversible amorphization in low-pressure regime [92], and others exhibit irreversible amorphization on compression through collapse of their pore volume, either retaining the short-ranged order [93] or by undergoing endothermic bond-rupture [94]. While the crystal-to-amorphous transition in these MOFs requires hydrostatic pressure in a few GPa, an exceptionally *stable* porous MOF-5 amorphizes at vanishingly low pressure of the order of 10 MPa, that is, about a 100 times lower! [3, 48]. This is quite atypical since the structure of MOF-5 consists of a rigid octahedral SBU encasing ZnO_4 tetrahedra, bonded with strong carboxylate groups [1]. Studies of pressure-response of MOF-5 carried out so far ascribe this irreversible amorphization, and consequent pore-collapse, to the breaking of carboxylate bonds [3, 48, 95]. This is believed to originate from the anharmonic dynamics of unstable non-dispersive phonon branches in response to external perturbation and kinetic stabilization of a plethora of amorphous phases within the high-symmetry structure [96]. While local

atomic vibrations explain structural transitions that give rise to cooperative phenomena at the nano-scale, for instance emergence of ferro-electricity in HfO_2 [97], their manifestation as preferential cleavage of strong carboxylate (C-O) bonds of MOF-5 in response to pressure within a few MPa, is quite inconceivable. Therefore, it is imperative to understand the nature of bond-breaking, or its lack thereof, in porous MOF-5 crystal to establish its stability-window, as well as in its suitability among other candidate MOFs for prospective applications.

4.2 Results and Discussion

In this work, we study the structural and dynamical response of MOF-5 to compressive strains, and understand the mechanism of its crystal-to-amorphous transition. In contrast to the earlier reports [3, 48, 95], we find that MOF-5 undergoes an order-to-disorder transition at infinitesimal hydrostatic strain $\epsilon_h \sim$ -0.003, which emerges from symmetry-lowering torsional forces and destabilization of its SBU about the central O-atom. Lattice-dynamical and group-theoretical analysis of phonons of MOF-5 unravel the role of triply-degenerate normal modes of its $Fm\bar{3}m$ phase associated with its structural transition. Using first-principles density-functional tight-binding approach, we show that at large compressive strains, structures distorted along the randomized unstable phonon-eigenvectors relax to lower energies, disrupting the long-ranged order of the MOF-5 crystal and resulting in its amorphization. With noticeable spread in the framework angle, Zn-O-Zn, while retaining the C-O bond lengths of the pristine crystal, the simulated

amorphous structures at $\epsilon_h \sim$ -0.08 highlight that amorphization of MOF-5 originates primarily from orientational disordering of ZnO_4 tetrahedra of the SBU, while ruling out the possibility of bond-rupture.

Our calculations are based on first-principles density functional theory (DFT), with plane-wave basis and pseudopotential method as implemented in Vienna Ab initio Simulation Package (VASP) [98]. The ionic core-valence electron interactions are modeled with ultrasoft pseudopotentials [99] and electronic exchange-correlation functional is approximated with a generalized gradient approximation (GGA), as parameterized by Perdew-Burke-Ernzerhof [100]. Kohn-Sham wave-functions are represented in a plane-wave basis sets truncated with an energy cutoff of 560 eV. A uniform (2 x 2 x 2) **k**-mesh is used for sampling the Brillouin Zone of primitive cell of MOF-5, while atomic relaxation is carried out with steepest gradient method until the Hellman-Feynman forces are lower than 1.0 meV/$\mathring{A}$ on each atom. The force-constants (or Hessian matrix) are obtained from symmetry reduced set of atomic displacements using a finite-difference method in VASP with a step-size of 0.025 $\mathring{A}$. Large dimensions of primitive cell of MOF-5 (over 12 $\mathring{A}$) in each direction, with a system-size of 106 atoms, enable the calculation of all the force-constants with a (1 x 1 x 1) primitive cell. Hessian matrices at specified q points are then computed using Phonopy [101] code. Manifestations of lattice-instabilities at larger strains, and the breakdown of long-range order are analyzed by structural optimization of (2 x 2 x 2) and (3 x 3 x 3) supercells using density functional tight-binding method, as implemented in DFTB+ code [102] with parameters from the set *3ob-3-1* [103, 104].

MOF-5 has a cubic structure that consists of $Zn_4O(CO_2)_6$ secondary

building units (SBU) with octahedral geometry (Fig. 4.1), each containing four ZnO_4 tetrahedra with a common O-vertex (henceforth referred to as O^C-atom) [1], and the remaining peripheral O atoms (referred to as O^P-atom) of each tetrahedra are bound, in pairs, to C atoms of the carboxylate groups (see Figure 4.1c and d). These units form the Bravais sites of two interpenetrating *fcc* lattices, linked to benzene rings along [001] directions. Two carboxylate groups with a sandwiched benzene ring form a 1,4-benzodicarboxylate, commonly known as the BDC group. Octahedral geometry imposes stringent directionality constraints on the O^P atoms and the metal (Zn(II)) sites, imparting a high degree of stiffness to the SBU. Further, site-symmetry inequivalence of O atoms (O^C and O^P) gives rise to deviations in Zn-O^C and Zn-O^P bond lengths of bulk MOF-5 ($\sim$ 0.003 $\mathring{A}$), and correspondingly difference of $\sim 4^o$ between O^C-Zn-O^C and O^C-Zn-O^P bond angles, rendering the tetrahedra inherently distorted. Despite these small differences in topological parameters, the MOF-5 crystal exists in an *fcc* lattice with $Fm\bar{3}m$ symmetry, as corroborated by simulated XRD pattern showing high peak-intensity for (110), (121) and (220) peaks (Figure 4.1e).

Vibrational spectrum of MOF-5 crystal confirms its local stability in the cubic $Fm\bar{3}m$ phase [105] (see Fig. 4.2a). Further, it exhibits flat phonon bands at very low frequencies ($\omega \sim \{0.6\text{-}0.8\}$ THz and $\{1.3\text{-}1.7\}$ THz) which are essentially dispersion-less, which signifies that the eigen-vectors of these normal modes can be chosen to be highly localized in the real space. Irreps of these low-energy phonons, $\vec{u}_{\nu\vec{q}} = \frac{1}{\sqrt{M_l}}\vec{e}_{\nu\vec{q}}$, $\vec{q} = 0$ are tabulated in Table 4.1, along with symmetry of the structures they generate.

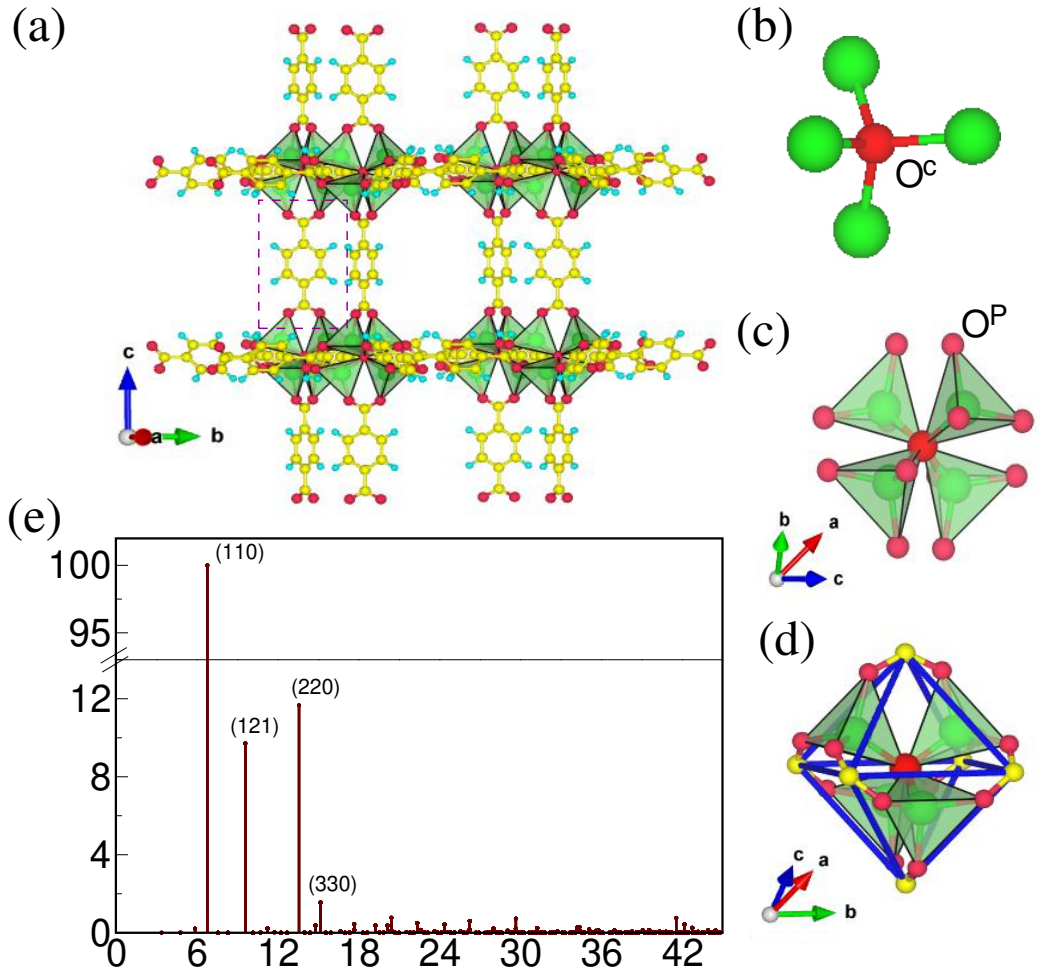

Figure 4.1: Structure of MOF-5 crystal: (a) Cubic structure viewed along [110] direction. Adjacent SBUs are rotated by 90^0 about each other, and are bonded through organic linkers (i.e. benzene rings) along $\langle 100 \rangle$. Dashed box delineates the 1,4-benzodicarboxylate or the BDC group [1]. Constituents of the SBU: (b) inner Zn_4O^C tetrahedron forms its core, (c) each of the Zn is bonded with three peripheral oxygen to form four ZnO^CO^P tetrahedra, and (d) pairs of O^P atoms of adjacent tetrahedra are bonded to C atoms, exhibiting an octahedral geometry of the SBU. (e) Simulated XRD shows high peak-intensity primarily along (110), (121), (220) planes, and the corresponding q-values agree closely with the experimental observations for single-crystal MOF-5 [2].

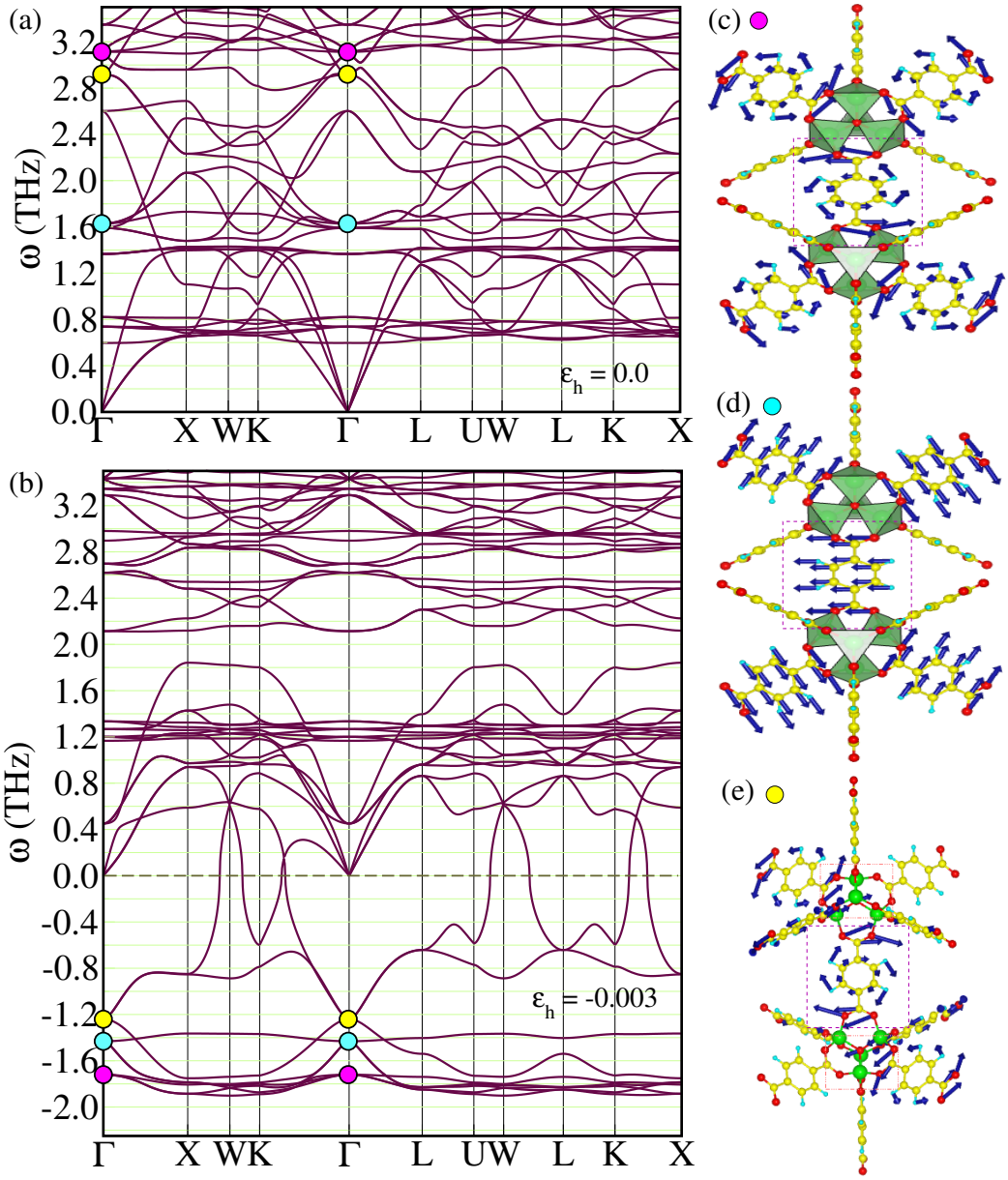

Figure 4.2: Low-frequency region of phonon dispersion of bulk MOF-5: (a) $\epsilon_h = 0$, showing stable phonons, confirming its local stability in $Fm\bar{3}m$ phase, (b) upon vanishingly small hydrostatic compression, $\epsilon_h \sim$ -0.003, lattice instabilities appear across the BZ. Overlap of eigen-vectors of stable structure $\epsilon_h = 0$ with that of dynamically unstable configuration ϵ_h = -0.003 show de-stabilization of higher-frequency phonons (marked by circles), with point-group symmetries T_{1g}, T_{2u} and T_{2g} (see Table 4.1). These modes give rise to torsional forces on the SBU octahedron, through (c) rotation of BDC group (ω = -1.7 THz), (d) in-plane displacements of BDC-group (ω = -1.43 THz), and (e) rotation of BDC group and shearing of SBU through displacements of O^C atoms (ω = -1.2 THz).

Table 4.1: Symmetry labels and calculated frequencies of soft phonons modes Γ-point of bulk MOF-5 subjected to volumetric strains; ϵ_v = 0.0 and ϵ_v = -0.009. Column III and IV show resulting subgroups of $Fm\bar{3}m$ and the symmetry label respectively, corresponding to the normal mode of primitive MOF-5 crystal.

ϵ_h = 0.0	ϵ_h = -0.003	Resulting	Irrep
ω (THz)	ω (THz)	structure	
3.1	-1.7	P-1 (2)	T_{1g}
3.1	-1.7	P-1 (2)	
3.1	-1.7	C2/m (12)	
1.6	-1.4	C2 (5)	T_{2u}
1.6	-1.4	C2 (5)	
1.6	-1.4	Imm2 (44)	
2.9	-1.2	P-1 (2)	T_{2g}
2.9	-1.2	P-1 (2)	
2.9	-1.2	C2/m (12)	
1.5	0.4	P1 (1)	T_{1u}
1.5	0.4	Cm (8)	
1.5	0.4	P1 (1)	
0.6	1.1	Fm-3 (202)	A_{2g}
1.4	1.2	C2 (5)	T_{2u}
1.4	1.2	C2 (5)	
1.4	1.2	Imm2 (44)	
0.7	1.3	P-1 (2)	T_{1g}
0.7	1.3	P-1 (2)	
0.7	1.3	C2/m (12)	
0.8	1.4	Fmmm (69)	E_g
0.8	1.4	I4/mmm (139)	

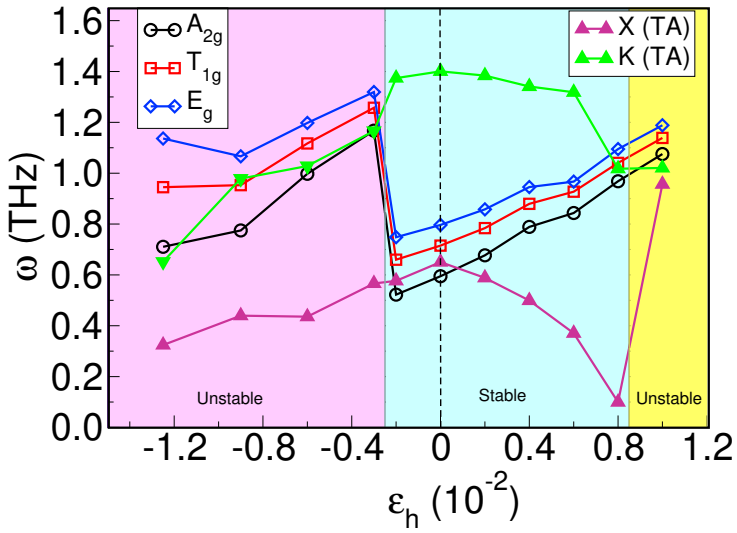

Figure 4.3: Evolution of low-frequency flat optical phonons upon hydrostatic strains. These modes couple with TA modes along Γ-X in pristine MOF-5, to form *composite* modes at the BZ boundary. On compression, ϵ_h = -0.003, while the high-frequency phonons become unstable, the low-frequency flat branches decouple with softest TA branch, undergo hardening, and couple with TA modes along Γ-K. With expansion, TA-optical coupling is deferred until ϵ_h = 0.01, beyond which the structure destabilizes.

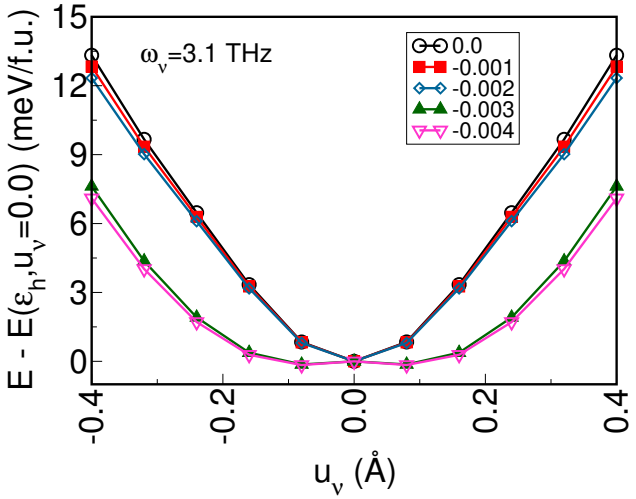

Figure 4.4: Quadratic dependence of internal strain energy on amplitude u_ν of eigenvectors of modes that become unstable at ϵ_h = -0.003. For ϵ_h < -0.003, the energies show a quartic dependence. This change suggests pressure-induced order-to-disorder structural phase transition of MOF-5 at ϵ_h = -0.003

In response to hydrostatic compression, MOF-5 loses its structural stability in the parent $Fm\bar{3}m$ phase at infinitesimally small strain, ϵ_h = -0.003, with a corresponding normal stress σ_1 ∼0.12 GPa. This is evident from the unstable optical branches i.e. phonons with imaginary frequencies, occurring across the first Brillouin Zone (BZ) of MOF-5 (Fig. 4.2(b)). Relatively higher stress σ_1 to destabilization than that observed in pressure-induced structural transitions of MOF-5 is attributed to calculations at $0K$, in contrast to experiments [48] at ambient conditions (T ∼ 300 K). Projections of eigen-vectors of these unstable modes onto the stable normal modes of unstrained MOF-5 show maximum overlap with relatively higher-frequency phonons (ω = 3.11, 1.63 and 2.92 THz) (See Table 4.1). Concurrently, very low-energy A_{2g}, E_g and T_{1g} modes of MOF-5 with $\omega < 1$ THz exhibit noticeable hardening upon compression (see Table 4.1). Appearance of strain-induced lattice instability with respect to relatively higher-frequency phonons, while excepting the softer ones, is quite intriguing and requires further analysis.

To this end, we understand the strain-dependence, both compression and expansion, of low-frequency optical phonons with $\omega < 1.0$ THz, and soft transverse (TA) and longitudinal acoustic (LA) phonon bands of MOF-5 (Fig. 4.3). In unstrained MOF-5, the flat, non-dispersive modes *resonate* with the *softest* TA phonons at the X-point (see Fig. 4.3). On compression (ϵ_h = -0.003), while the Γ-X TA branch softens, the low-frequency optical modes ($\omega < 1.0$ THz) undergo mode-repulsion with Γ-X TA phonons, and exhibit coupling with TA branch along Γ-K. This abrupt hardening occurs concurrently with the lattice instability of MOF-5 in its parent phase and destabilization of its higher-frequency phonons at ϵ_h = -0.003. With hydrostatic

expansion, $\epsilon_h > 0$, the cubic symmetry is preserved until relatively larger strains (ϵ_h ~0.008) as the strength of coupling between TA branch along Γ-X and flat optical modes continuously decreases (see Fig. 4.3). Nonetheless, at $\epsilon_h = 0.01$, overlap of acoustic and optical phonon branches leads to lattice instability across the BZ. This reinforces that structural destabilization of MOF-5 is driven by coupling between TA and stable *soft* optical branches that give rise to *composite* (or hybridized) normal modes at BZ boundaries.

Visualization of the eigen-modes of relatively higher-frequency phonons, that become unstable on vanishingly small compressive strains, show rotation and in-plane displacements of the BDC groups (See Fig. 4.2c,d,e). These groups act like chemical *fasteners* to each pair of $ZnO_3^P O^C$ tetrahedra (Fig. 4.1a), generating non-zero torque (Fig. 4.2c,e) or linear motion (Fig. 4.2d) upon hydrostatic strains, resulting in twisting of one side of SBU relative to the stationary one, about the central oxygen O^C. Consequent *torsional* forces destabilize the *rigid* SBU at infinitesimal compression $\epsilon_h \sim$ -0.003, clearly indicating that the MOF-5 crystal cannot sustain hydrostatic compression in its parent $Fm\bar{3}m$ phase. Thus, despite a large pore volume (~ 3100 m^2/g) [106], as well as low bulk modulus (about 15.84 GPa) [107], destabilization of MOF-5 in response to infinitesimal strains emerges primarily from geometrical constraints and emergent structural instabilities. Such distortions have been observed in paddle-wheel SBU involving conformational twist of four carboxylates in the equatorial plane [108] around the rotational 4-fold axis, which results in reversible *pre-amorphization* in response to small pressures (~ 0.7 GPa).

As these instabilities are weak and arise at minuscule strains, we determine the energetics of structural distortions with respect to each of these triply-degenerate modes in one of three directions: mode A (C2/m): ω = 3.113 THz, mode B (Imm2): ω = 1.628 THz, and mode C (C2/m): ω = 2.918 THz (Table I), as a function of hydrostatic compression. We freeze-in varying amplitudes (u_ν in $\mathring{A}$) of eigen-displacements of these modes in MOF-5 structures relaxed to their energy-minimum at varying strains (i.e. ϵ_h = [0.0, -0.004]), and obtain the energy, E(ϵ_h, u_ν)-E(ϵ_h, u_ν=0). Interestingly, energies of all the three modes (A, B and C) show a transition from quadratic dependence on u_ν for $|\epsilon_h|>$ -0.003, to quartic-dependence (i.e. anharmonic, or double-well potential) in u_ν for $\epsilon_h <$ -0.003 (Fig. 4.4 for ω = 3.3 THz) with very small changes in energies, within a few meV/formula unit of MOF-5 for relatively large values of u_ν. This clearly indicates an order-to-disorder structural phase transition [109] at very small hydrostatic strain ($\epsilon_h \sim$ -0.003).

While the foregoing discussion illustrates the mechanism of destabilization of MOF-5 crystal in Fm$\bar{3}$m phase, we now elucidate the nature of *internal* structural rearrangements and changes in the long-range order that arise with respect to the unstable vibrational-modes upon varying hydrostatic strains. Since amorphization involves disruption of long-range order, and periodic cell of a lattice imposes spatial limit on the range of effect of inter-atomic interactions, we demonstrate the structural changes in MOF-5 due to *flat* unstable phonons across the BZ by considering (1 x 1 x 1), (2 x 2 x 2) and (3 x 3 x 3) supercells, containing 106, 848 and 2862 atoms respectively. We introduced $\{\vec{u}\}$ into the strained structures of MOF-5, $|\epsilon_h|\in$

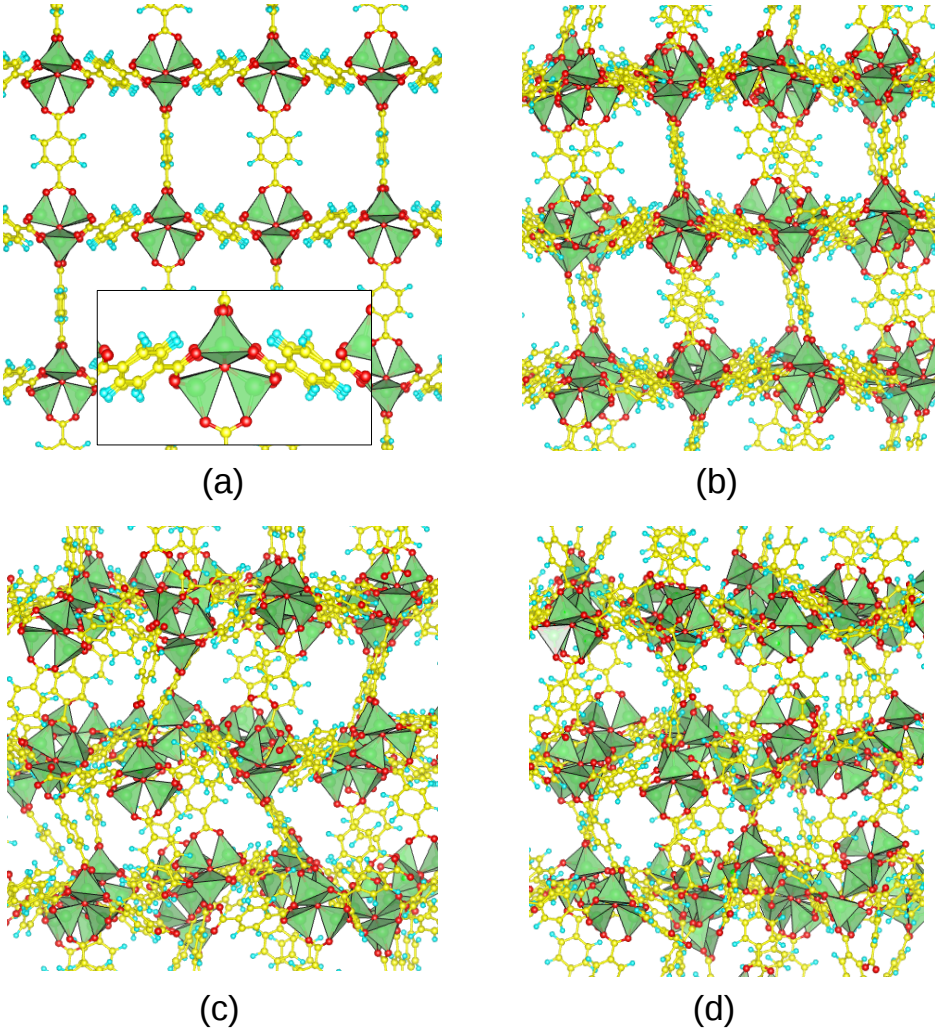

Figure 4.5: Structural distortions and amorphization upon relaxation with respect to lattice instabilities in (3 x 3 x 3) supercells of MOF-5: (a) at ϵ_h = -0.003, MOF-5 crystal undergoes mis-orientations about O^C-atom of SBU. This manifests as breaking of octahedral symmetry and rotation of benzene rings about [100] axis. (b) at ϵ_h = -0.025, the distorted structure at energy-minimum shows off-centering of O^C atoms from the (0,0,0) lattice sites of $Fm\bar{3}m$ phase. At $|\epsilon_h|>$ 0.05, (c) and (d), colossal structural distortions lead to complete dis-positioning of building units about the {100} planes, while maintaining the short-range order in Zn-O_4 tetrahedra.

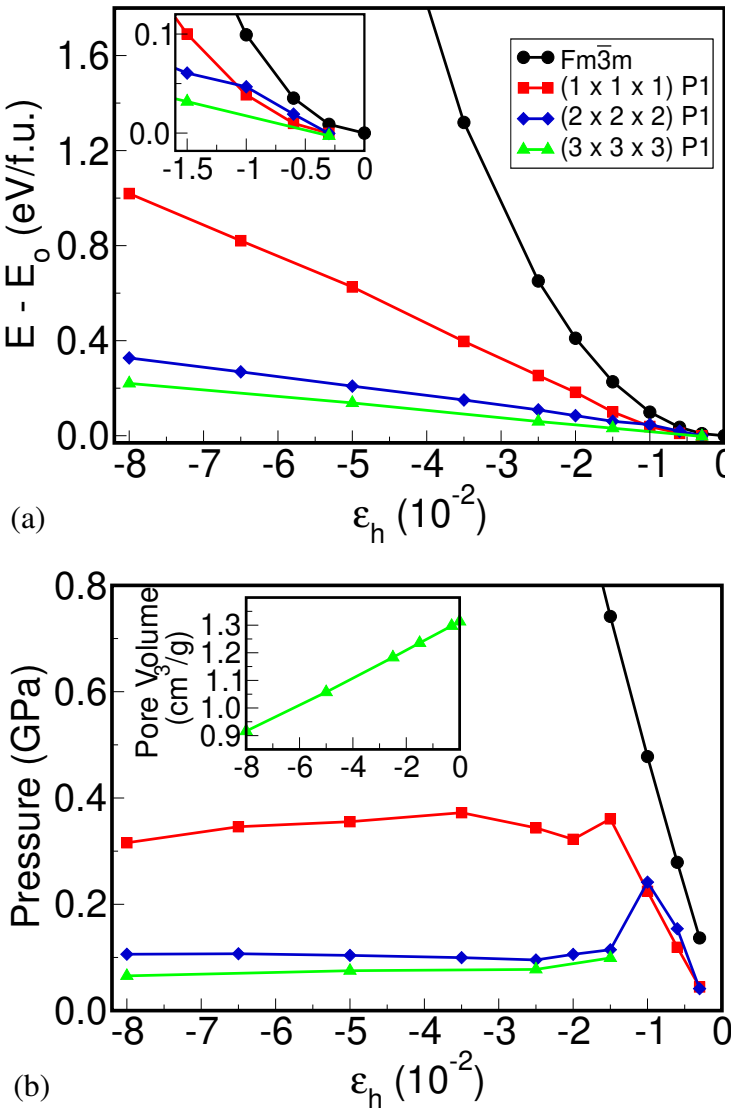

Figure 4.6: Changes in energies and stresses on structural distortion with respect to unstable phonon modes: (a) energies and (b) stresses of structures distorted with random combinations of unstable phonon modes, and optimized to minimum-energy keeping cell-shape and cell-volume fixed. Increase in strain energies with ϵ_h are significantly smaller in (2 x 2 x 2) and (3 x 3 x 3) deformed supercells, in comparison to the corresponding (1 x 1 x 1) cells. Stresses increase upto $|\epsilon_h| = 0.015$, but remain essentially constant at higher $|\epsilon_h|$, indicating enhanced degree of internal rearrangements allowing isobaric compression of MOF-5 crystal. Inset of (b) shows significant decline in pore volumes of deformed (3 x 3 x 3) supercells on compression.

{0.003, 0.8}, each optimized while preserving Fm$\bar{3}$m symmetry. The atomic displacements $\{\vec{u}\}$ (with respect to the reference structures) are represented in terms of unstable modes $\vec{u}_\nu$:

$$\vec{u} = \sum_{\nu=1}^{9} c_\nu \vec{u}_\nu \qquad (4.1)$$
$$c_\nu : random \in \{0.0, 1.0\}$$

where the sum is over 9 unstable phonon modes (See Fig.). Using density-functional tight-binding method, we carried-out energy-minimization of the distorted structures at a fixed cell-shape and cell-volume. This resembles conditions typically occurring at high strain rates or compression carried out in diamond anvil cell (DAC), without a hydrostatic medium.

Optimization of strained MOF-5 structures with lattice distortions corresponding to *randomized* unstable phonon modes results in lowering of its crystal-symmetry from Fm$\bar{3}$m to P1 at very low $\epsilon_h \sim$ -0.003, with negligible change in the strain-energy ($\sim$ 10 meV/f.u.) (see inset of Fig. 4.6a). Mis-orientations of ZnO_4 tetrahedra about O^C arising from rotations or displacements of the BDC groups (see Fig. 4.2c,d,e) and consequent distortion of octahedral SBU, give rise to deviation in CO^CC bond angles by $\pm 1.5^o$ from 90^o in pristine Fm$\bar{3}$m phase (see Fig. 4.5a), resulting in a lower stress relative to the dynamically unstable constrained cubic structure. Crystallanity or long-range order of pristine MOF-5 is preserved in this distorted *polymorph*, as evident from sharp features in its structure-factor, $S(\vec{q})$, upto $\mathbf{q} \sim 10\mathring{A}^{-1}$ (Fig. 4.7a).

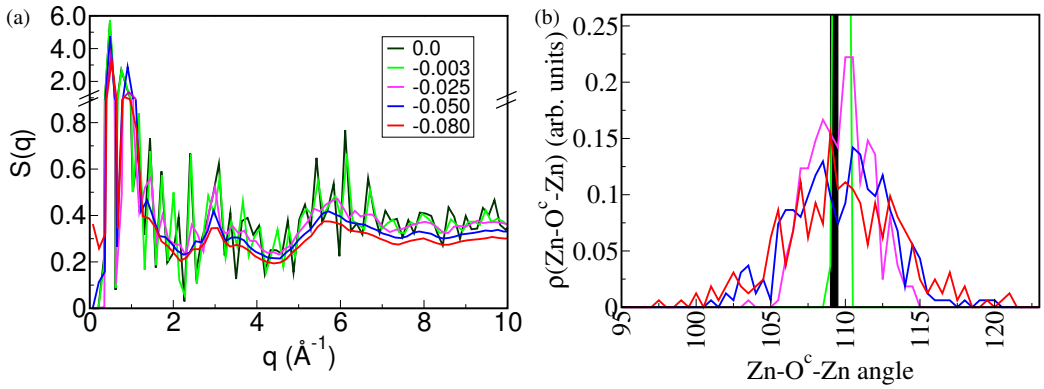

Figure 4.7: Signatures of crystal-to-amorphous transition of MOF-5 with hydrostatic strains: (a) Structure factor S($|\vec{q}|$) of (3 x 3 x 3) distorted cells, showing significant decrease in the height of the most dominant peak at low $|\vec{q}|$, and lack of sharp features at $|\vec{q}|> 6\mathring{A}$ with increase in $|\epsilon_h|$. (b) Variations in framework angle, Zn-O^C-Zn, that signify the degree of mis-orientations of ZnO_4 tetrahedra about central O^C atom. Large spread in Zn-O^C-Zn angles results in the loss of long-range order of MOF-5 crystal at higher $|\epsilon_h|$.

Degree of structural disorder increases with hydrostatic strains ($|\epsilon_h|>$ 0.015) (Fig. 4.5). Loss of long-range order on compression is evidenced by the reduction in strain energies, as well as release of stresses due to internal structural rearrangements of (2 x 2 x 2) and (3 x 3 x 3) strained cells, compared to that in corresponding (1 x 1 x 1) distorted structures (see Fig. 4.6). Gradual changes in strain energies with $|\epsilon_h|$ invalidate the plausibility of bond-breaking events in the compressed structures. Further, a decline in S($|\vec{q}|$) at very low $|\vec{q}|$, by about 55% at $\epsilon_h \sim$ -0.08, and absence of sharp features beyond $|\vec{q}|\sim$ 4-6$\mathring{A}^{-1}$ corroborate crystal-to-amorphous transition of MOF-5 (Fig. 4.7), arising from structural relaxation with randomized unstable lattice modes. Amorphous-MOF-5 structures exhibit significant densification. For instance, at ϵ_h = -0.08, there is a reduction in pore volume by about 33% relative to pristine MOF-5, with little increment in pressure (P

$\sim$ 0.07 GPa). Indeed, this decline in porosity is fully consistent with significant reduction in the surface area of pressure-induced amorphous structure of MOF-5 [48].

Since the lattice instability is associated with misorientations of ZnO_4 tetrahedra about the central O^C atom, amorphization of MOF-5 at large compressive strains originates from order-to-disorder transition of MOF-5 [110, 111], with concurrent release of structural stresses. This is in contrast to the proposed mechanism of irreversible amorphization of MOF-5 involving rupture of a few carboxylate groups of MOF-5 [48].

We now analyze the topological features of optimized distorted structures at varying hydrostatic compression. $ZnO_3^PO^C$ tetrahedra described by Zn-O bond lengths and O-Zn-O angles, and carboxylate groups, with C-O^P bonds and O^P-C-O^P angles, characterize the short-range order and local coordination in pristine and distorted MOF-5 structures. Framework parameter, namely Zn-O^C-Zn angle, can reveal disruption of octahedral symmetry or degree of mis-orientations in the SBU, that results in the loss of long-range order of MOF-5. In addition to featureless S($|\vec{q}|$) at large $|\vec{q}|$, significant spread in Zn-O^C-Zn with increase in $|\epsilon_h|$ (see Fig. 4.7b), indeed confirm amorphization of MOF-5 crystal, originating primarily from orientational disordering of $ZnO_3^PO^C$ tetrahedra about the central O^C atom of SBU. With deviation of $\pm$ 5^o in O^P-C-O^P bond angles, and negligible change in $\mathbf{b}$(C-O), $\pm$ 0.03 $\mathring{A}$ (see Fig. 4.8a,b), cleavage of carboxylate bonds is essentially ruled out. Nonetheless, substantial tetrahedral distortion, as evident from changes in O-Zn-O ($\pm$ 20-25^o) angles, while preserving $\mathbf{b}$(Zn-O) within $\pm 0.05\mathring{A}$ (Fig.

4.8c,d), reinforces that amorphization of MOF-5 is driven by internal structural rearrangements, rather than *catastrophic* bond-breaking events.

In conclusion, we have demonstrated that a *stable* MOF-5 crystal cannot sustain hydrostatic compression, primarily due to symmetry-lowering torsional forces that distort its octahedral SBUs upon infinitesimal strain, $\epsilon_h \sim$ -0.003. Relatively higher-frequency triply degenerate phonons become unstable at very small compressive strains leading to an order-to-disorder structural phase transition, essentially ruling-out the breaking of carboxylate bonds at low pressures. At large strains, relaxation of MOF-5 structures distorted along the randomized eigenvectors of the flat, unstable phonon bands exhibit disruption of long-range order of the MOF-5 crystal, resulting in its amorphization. The microscopic mechanism of destabilization involving orientational disordering in SBUs of MOF-5 is generalizable to many other MOFs that encase directionally constrained rigid building units in their three-dimensional network structure [34].

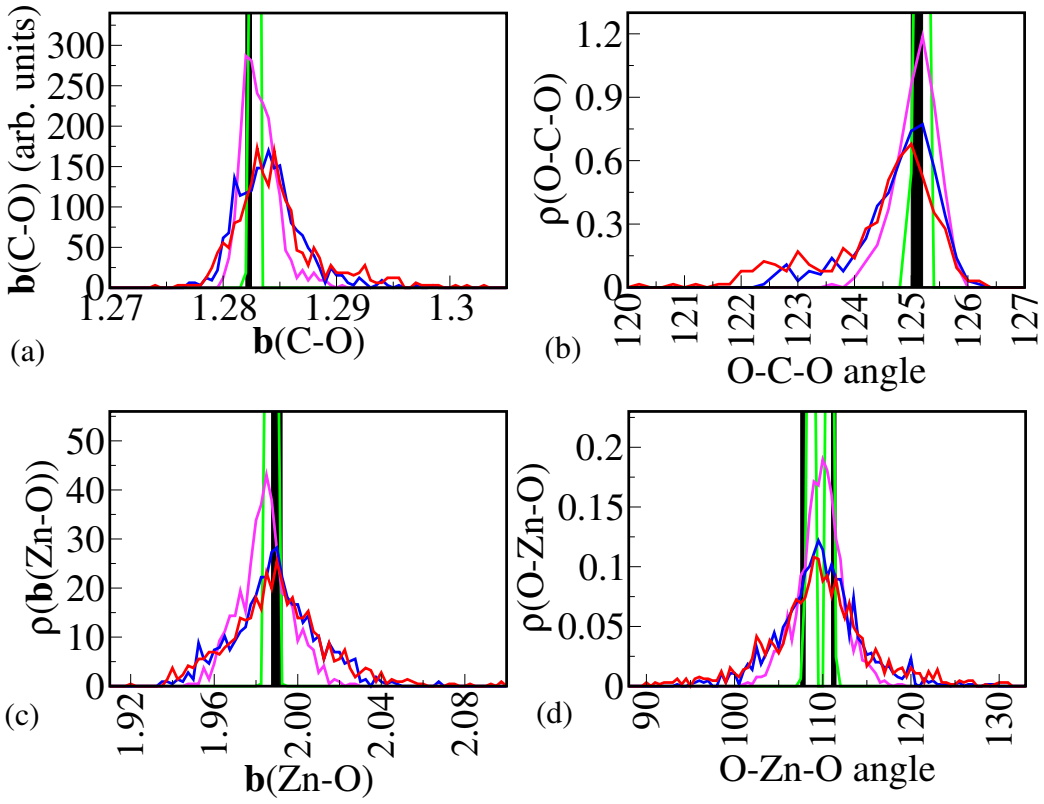

Figure 4.8: Local structural distortions on crystal-to-amorphous transition of MOF-5 with hydrostatic compression: (a) C-O^P bond lengths, and (b) O^P-C-O^P angle of the carboxylate group. Small variations in $\mathbf{b}$(C-O^P) negate the possibility of bond-breaking, in contrast to the prediction of Erkartal *et. al.* [3]. (c) Zn-O bond lengths, and (d) O-Zn-O bond angles of ZnO_4 tetrahedra, indicating significant distortions of local structural motifs with $|\epsilon_h|$

.

Chapter 5

Non-linear elasticity and amorphization of ZIF-8: Lattice-dynamical analysis

5.1 Introduction

By virtue of their chemistry and network topology, zeolitic-imidazole frameworks (ZIFs) form an interesting class of crystalline nano-porous metal-organic frameworks [30] with highly tunable structural metrics, and exceptional thermal and chemical stability [49]. Consisting of rigid molecular polyhedra interconnected by a variety of organic linkers, ZIFs exhibit a plethora of chemical properties that enable their widespread applications in gas-storage [112] and separation [113], heterogeneous catalysis [114], and drug delivery [115]. While porosity of a framework [32] is crucial, practical applications *de facto* depend on its mechanical and thermal stability [116] against

external perturbations [117, 118]. When subjected to hydrostatic compression, ball-milling or nano-indentation, crystalline ZIFs have been shown to undergo reversible [119] or irreversible [50, 120] amorphization [121]; with a concomitant decline in porosity [51], or a sudden structural-collapse [122] limiting their suitability in many structure-sensitive applications. Recently, investigations of structural and functional properties of amorphous-MOFs has been the focus of extensive research [54–57] in order to uncover their industrial and technological relevance. Therefore, it is essential to develop proper understanding of different mechanisms of crystal-to-amorphous transitions to attain better controllability and structural tunability in response to mechanical strains.

Amorphous ZIFs (aZIFs) have been known to retain their structural motifs (metal-centred tetrahedra and organic linkers) and local coordination of their crystalline counter-parts, but lack the long-range periodic order [50, 123], as identified by pair-distribution functions or XRD- diffraction or neutron scattering experiments. Disorder in the network topology gives rise to broader diffraction peaks and diffuse scattering, and loss of medium- or long-range order as characterized by featureless Bragg diffraction pattern at longer-distances [124]. Dynamics of amorphization has revealed cooperative structural rearrangements [125], twisting, mis-orientations of organic linkers, and framework reconstruction [123]. While the studies establish structural, geometrical, topological and dynamical signatures that characterize the amorphous state of ZIFs, the mechanism of crystal-to-amorphous transition, as well as distinction in structures of amorphous phases synthesized from dissimilar routes [124] is still unclear. Computational studies of

deformation-response to hydrostatic pressures have attributed *amorphization* of ZIFs to very low shear modulus [52], shear instability ($C_{44} < 0$) [53, 126], breathing modes associated with linker-rotation at very low-frequencies [126], and distortion of ZnN_4 tetrahedra or fracture [127], with no structural evidence of disruption of the long-range order.

Ramification of strains, hydrostatic or non-hydrostatic, pertinent to amorphization of ZIFs on ball-milling or nano-indentation is yet an unsettled topic in their mechanical response to external perturbations. Understanding the nature of structural transitions, and changes in constituent building units and framework topology is indispensable in selection of robust structures among the candidate ZIFs to be brought into service, as well as in judicious design of amorphous frameworks for desired applications. Among the plethora of ZIF structures known till date, ZIF-8 has been known to exhibit high thermal stability and high porosity in its as-synthesized form [49]. Existing in a sodalite structure [128], encasing a cube-obtahedral pore, its tendency to amorphize on ball-milling or application of modest pressures ($P \sim 0.3$ GPa) [51, 53] has been a subject of active research for sometime now. We, thus consider ZIF-8 as the prototypic MOF for lattice-dynamics based study of its crystal-to-amorphous transition in response to both hydro-static (ϵ_h) and non-hydrostatic (rhombohedral shear ϵ_r) strains, within the framework of density-functional tight-binding approach.

5.2 Results and Discussion

We first establish inherent *non-linear* elastic behavior of ZIF-8, in terms of coupling between long-wavelength acoustic phonons (and homogeneous strains) and *dispersive* soft optical-phonons. Dynamical stability of ZIF-8 at large shear stains ($\epsilon_r \sim 0.07$) counters the role of soft shear modulus (C_{44}) in its destabilization [52]. Upon compression, however, the higher-order mixed moduli (C_{144} and C_{1144}) give rise to a shear instability (i.e. negative C_{44}), which also manifests as dynamical lattice-instability at $\epsilon_h \sim$ -0.035 driven by soft-optical phonons of ZIF-8. While loss of shear rigidity, and hence enhanced *fluidity* of cubic ZIF-8, favors lowering of its structural symmetry, crystal-to-amorphous transition emerges dominantly from unstable modes throughout the BZ that become non-dispersive at $\epsilon_h \sim$ -0.10. Relaxation of (2 x 2 x 2) strained cells of crystalline ZIF-8 distorted with respect to random combinations of the eigen-vectors of the unstable modes results in disruption of long-range order leading to its amorphization. Analysis of *densified* structure obtained on ball-milling and modeled using reverse Monte-Carlo approach [50], exhibits significant distortion of ZnN_4 tetrahedra in addition to the loss of long-range order. This structure shows good agreement with simulated (2 x 2 x 2) distorted cell of ZIF-8 deformed with large hydrostatic and shear strains.

Our calculations are based on third-order density-functional tight-binding (DFTB3) method as implemented in DFTB+ [102]. To parameterize the inter-atomic interactions, the Slater-Koster files are used from parameter sets

3ob-3-1 [129,130], and Hubbard parameter is included to represent electron-electron interactions. Herein, the electronic exchange-correlation energy is approximated by a generalized gradient approximation (GGA) with the functional form given by Perdew-Burke-Ernzerhof (PBE). van der Waals (vdW) interactions are included with a Lennard-Jones dispersion, as implemented in DFTB+, with parameters taken from Universal Force Field (UFF) [131]. Integrations over the Brillouin Zone (BZ) are carried out with a uniform (2 x 2 x 2) **k**-mesh for bulk ZIF-8. Variable-cell relaxation of the structure is carried out using conjugate-gradient algorithm, with a low force-tolerance of 10^{-8} Ha/Bohr to obtain the correct crystal symmetry (space group: 217) and reduce the stresses to $\sim$ 0.01 kbar. Cell parameters of the relaxed structure deviate by $\sim$0.66% from the experimental value. Force-constants of bulk- and strained ZIF-8 structures are obtained using a (2 x 2 x 2) supercell with finite-difference method applied on symmetry-inequivalent displacements with a step-size of 0.04 $\mathring{A}$ to determine the Hessian matrix (matrix of the second derivatives of the energy with respect to atomic displacements) with Phonopy code [101]. Subsequently, dynamical matrices and corresponding phonon-eigenfunctions at a specified q-point are then computed along the specified BZ path [4].

Vibrational spectrum of ZIF-8 confirms its structural stability in the cubic I$\bar{4}$3m phase (See Fig. 5.1). Branches of soft transverse acoustic phonons along different directions are manifestations of low-shear elastic moduli of the crystal (see Ref. [81]). Unlike low-dimensional frameworks, for instance CuPA-2, that encompass a combination of strong covalent or coordination bonds and weak inter-molecular interactions, and show highly anisotropic

elastic response [132], ZIF-8 exhibits almost isotropic elastic behavior as evident for slopes of acoustic branches along different directions. This is ascribed to its near-spherical, cube-octahedral pore.

In response to rhombohedral shear strain ϵ_r, ZIF-8 exhibits a non-zero hydrostatic stress σ_1 (see Fig. 5.3a), that signifies a third-order coupling between hydrostatic (longitudinal acoustic phonons) and shear (transverse acoustic phonons) strains. This is reminiscent to acousto-elastic effect [133] observed in certain materials [134, 135]. The strength of coupling between homogeneous strains is obtained by polynomial expansion of strain-energy density $\tilde{E} = \frac{E}{V_o}$ in higher orders of strain components (ϵ_h and ϵ_r), upto fourth order as:

$$\begin{aligned}\tilde{E} = &\frac{1}{2}B_o\epsilon_h^2 + \frac{1}{2}C_{44}\epsilon_4^2 + \frac{1}{3}B_1\epsilon_h^3 + \frac{1}{2}C_{144}\epsilon_h\epsilon_4^2 + \frac{1}{3}C_{444}\epsilon_r^3 \\ &+\frac{1}{4}B_2\epsilon_h^4 + \frac{1}{2}C_{1144}\epsilon_h^2\epsilon_4^2 + \frac{1}{3}C_{1144}\epsilon_h\epsilon_4^3 + \frac{1}{4}C_{4444}\epsilon_4^4\end{aligned} \tag{5.1}$$

The coefficients are then obtained by fitting Equation 5.1 with the strain energies obtained from *ab-initio* calculations (see Table 5.1).

The value of linear elastic moduli of the ZIF-8 crystal, B_o = 8.50 GPa and C_{44} = 1.07 GPa are in close agreement with the experimental and first-principles DFT-based reports [136]. Further, derivatives of bulk modulus, B_1 and B_2, have negative values. Negative B_1, or a positive $\frac{\partial B_o}{\partial P}$ indicates a reduction in compressibility or structural hardening at larger compressive strains.

A low value of shear modulus C_{44} of ZIF-8 [52] has been intuitively

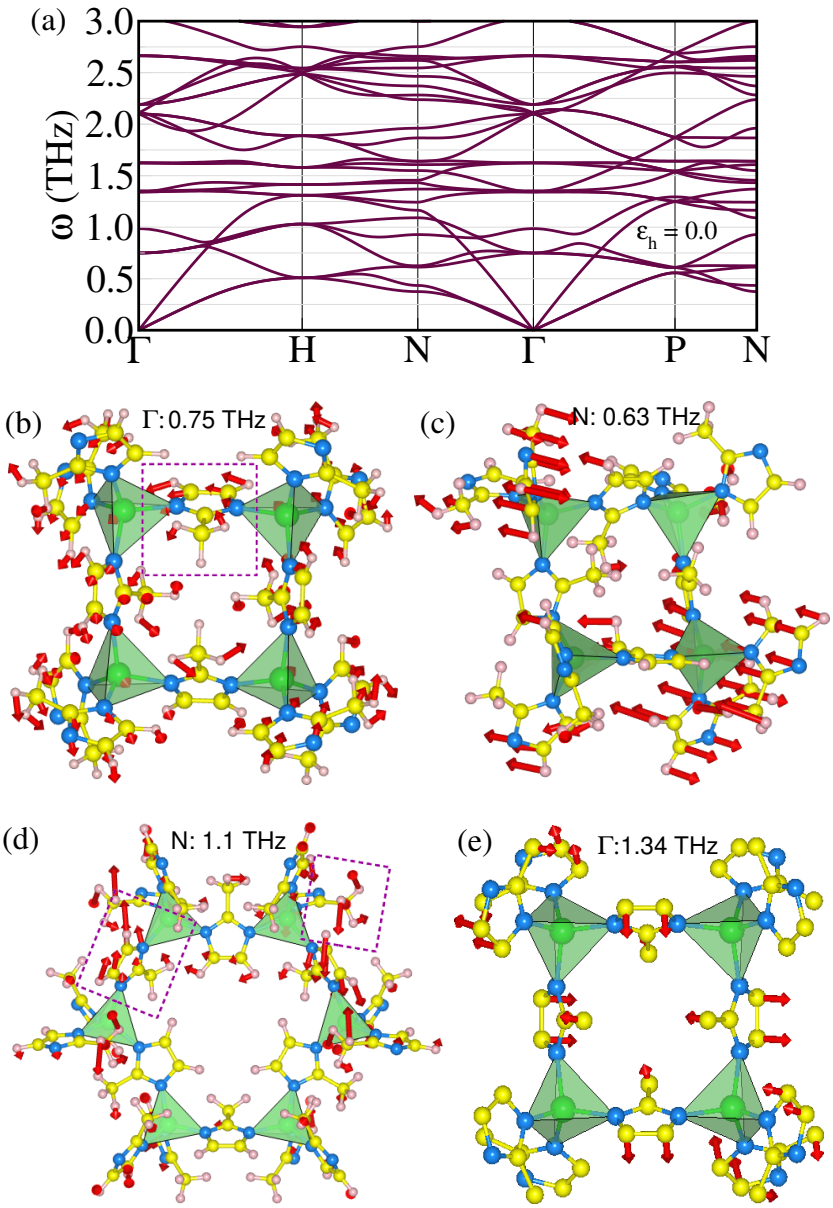

Figure 5.1: **Vibrational signatures of ZIF-8 crystal**: (a) Phonon spectrum of ZIF-8 crystal, confirming its lattice stability. Atomic vibrations corresponding to low-frequency optical branches exhibit (b) *in-plane* rotation of IM-linker, (c) shearing modes about the 4-membered rings of ZIF-8, (d) buckling and rotations of IM linkers, and distortion of Me-group, and (e) pore-opening modes associated with rotations of IM linkers.

Table 5.1: *Non-linear* elastic moduli of ZIF-8

Elastic modulus	Fitted value (GPa)
B_o	8.50
C_{44}	1.07
B_1	-13.3
C_{144}	-4.78
C_{444}	2.86
B_2	-29.31
C_{1144}	-45.85
C_{1144}	44.00
C_{4444}	40.38

thought to be linked to its destabilization and amorphization. However, vibrational spectra of sheared ZIF-8 crystal show structural stability retained until large $\epsilon_r = 0.07$ beyond which there is an appearance of lattice instability (see Fig. 5.2c), associated with pore-opening vibrations and Methyl-group rotations (see Fig. 5.2d). Introduction of random combinations of the eigenvectors corresponding to a single non-dispersive *unstable* phonon band into a (2 x 2 x 2) conventional cell of ZIF-8 (2208 atoms) with $\epsilon_r = 0.08$, and relaxation of the distorted structure to an energy-minimum shows retention of its long-range order. This is evidenced by sharp features in pair-distribution function (PDF) for $r \geq 6\mathring{A}$, and its similarity with the PDF of pristine ZIF-8 crystal (see Fig. 5.2e). This clearly shows that in the absence of hydrostatic strains, shear deformation does not induce a structural disorder or disrupt the long-range order of ZIF-8 crystal. Shear-deformed structures exhibit significantly high-density of low-frequency ($\leq$ 1 THz) phonon modes, as compared

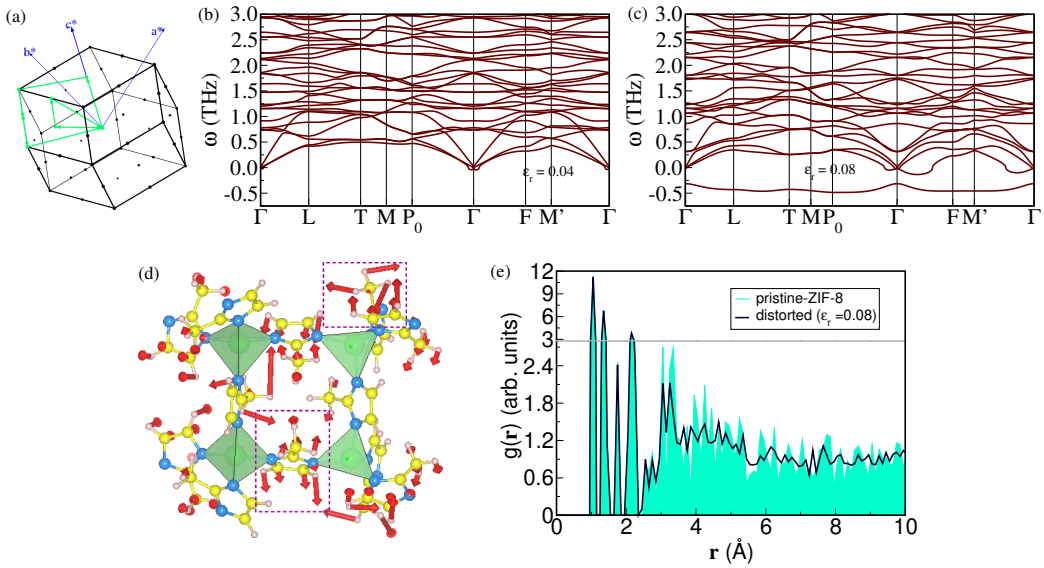

Figure 5.2: Vibrational spectrum of ZIF-8 upon shear deformation: (a) special points in the BZ of a rhombohedral crystal, and dispersion along the path described in Figure 19 of Ref. [4], phonon spectrum with (b) $\epsilon_r = 0.04$, and (c) $\epsilon_r = 0.08$. A significant increase in the density of low-frequency modes, in comparison to that in bulk ZIF-8 (Fig. 5.1a). Structural destabilization manifests as a dispersion-less phonon band across the BZ. (d) Atomic displacements in the unstable mode at $\vec{q} = 0$ represent bending of IM-group, and rotation of three H atoms about central C-atom of Me-group. Structural distortions with respect to these vibrations do not amorphize the ZIF-8 crystal, as evident from its pair-distribution function of the relaxed structure, (e).

that of the unstrained crystal (see Fig. 5.2b and c).

Taking into account the non-linear couplings between strains, the C_{44} depends on hydrostatic strain ϵ_h as:

$$C_{44}(\epsilon_h) = \frac{\partial^2 E}{\partial \epsilon_4^2} = C_{44}(\epsilon_h = 0) + C_{144}\epsilon_h + 2C_{444}\epsilon_r + C_{1144}\epsilon_h^2\epsilon_h^2 + 2C_{1444}\epsilon_h\epsilon_r + 3C_{4444}\epsilon_r^2 \tag{5.2}$$

Values of $C_{44}(\epsilon_h)$ at varying $\epsilon_h \in \{0.0, 0.07\}$ indeed show an onset of shear instability (negative C_{44}) at $\epsilon_h \sim$ -0.04 (See Fig. 5.3). This clearly indicates

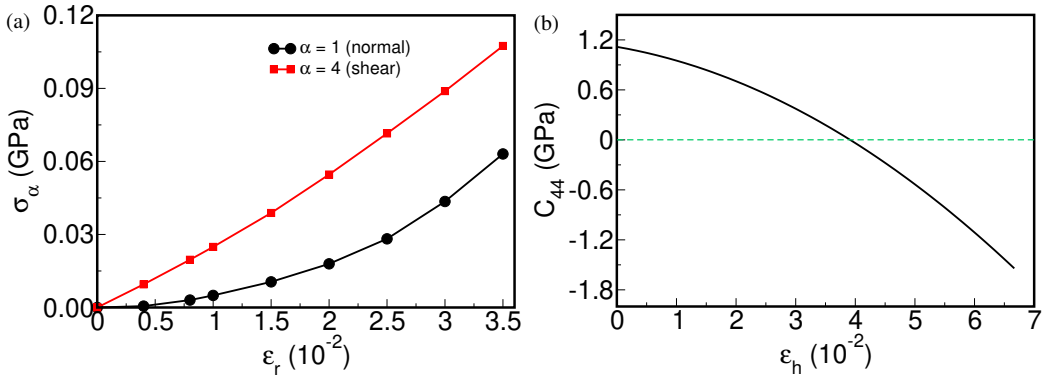

Figure 5.3: Non-linear elasticity and shear instability of ZIF-8 crystals: (a) on-zero σ_1 with ϵ_r at ϵ_h =0.0, (b) dependence of shear modulus C_{44} on hydrostatic strains ϵ_h. The modulus becomes negative at $\epsilon_h \sim$ -0.04, signifying an elastic instability.

the role of higher-order mixed elastic moduli C_{144} and C_{1144} in driving the elastic instability of ZIF-8.

Calculated phonons of minimum-energy structures of ZIF-8 at varying ϵ_h show continuous softening of low-frequency optical phonon bands ($\omega < 1.5$ THz) (see Fig. 5.4). This leads to a *de-coupling* from relatively higher-energy modes that remain essentially un-altered on compression (Fig. 5.4a). The soft-modes correspond to rotations/distortion of methyl (Me)-group, shearing of 4-membered channel or in-plane rotation or twisting of IM-linker about Zn^{2+} ions (see Fig. 5.1b,c,d). Pore-opening modes of vibrations associated with symmetric linker-rotation (Fig. 5.1e) have a slightly higher frequency ($\omega \sim$ 1.3-1.4 THz) and show no softening with increase in $|\epsilon_h|$. This indicates that these vibrations do not drive structural transitions of ZIF-8 on hydrostatic compression, in contrast to the destabilization mechanism recently proposed by Jefferson *et al.* [126], while confirming the co-existence of these modes in both porous crystalline and disordered ZIF-8 obtained on

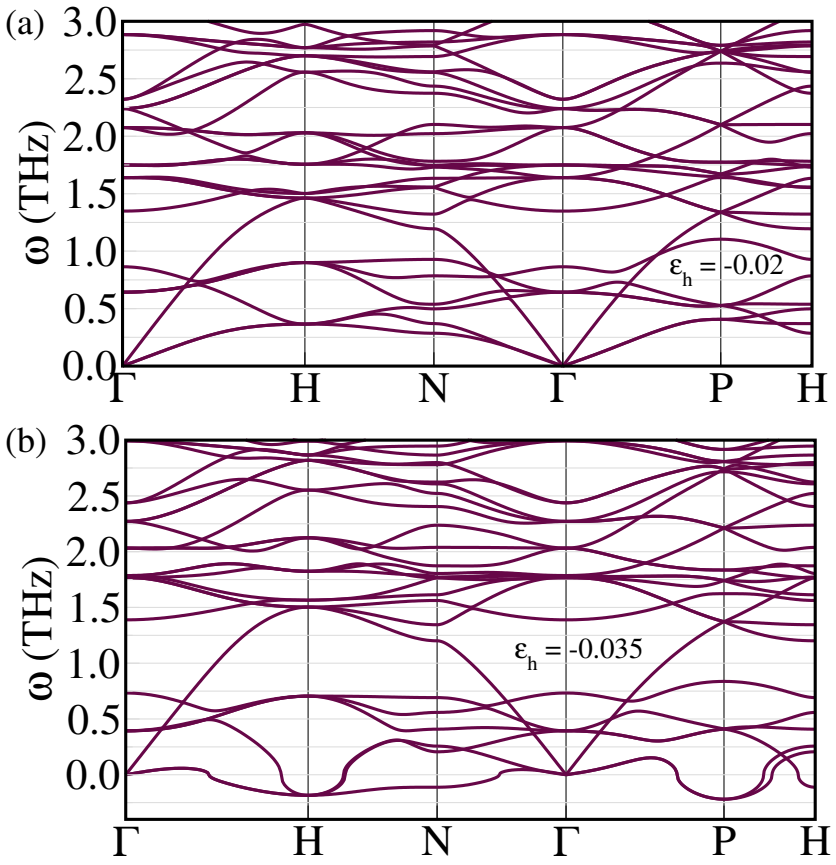

Figure 5.4: Phonon spectrum of ZIF-8 upon hydrostatic compression: (a) ϵ_h = -0.02, and (b) ϵ_h = -0.035. The latter shows negative slope of transverse acoustic phonons, and instability with respect to low-frequency optical modes at the zone boundaries.

compression or ball-milling [137].

Enhanced strength of coupling between transverse acoustic phonons and soft optical modes upon compression leads to structural destabilization (unstable modes) at strain ϵ_h = -0.035 (see 5.4b), close to strain at which elastic instability occurs, ϵ_h = -0.039. The corresponding pressure leading to instability is $\sim$ 1 GPa, which is slightly higher than the pressure $P_c \sim$ 0.3-0.4 GPa estimated with MD simulations at 300 K. With further increase in $|\epsilon_h|$,

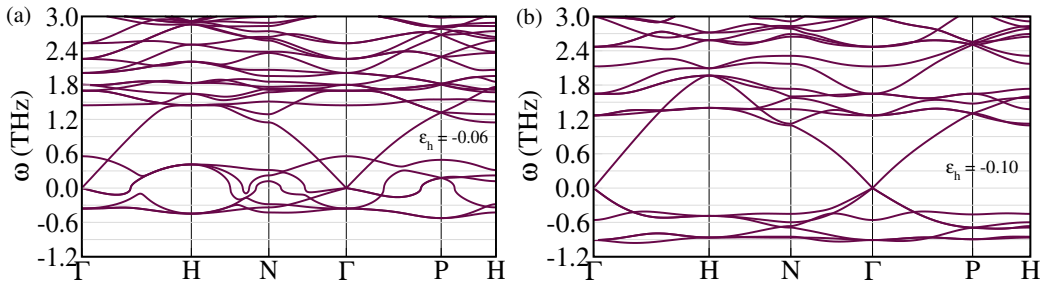

Figure 5.5: Change in phonon spectrum of ZIF-8 on large hydrostatic compression: Unstable phonons across the BZ, (a) dispersive at ϵ_h = -0.06 and (b) flat non-dispersive ϵ_h = -0.1. Transverse phonons with negative slopes signify shear elastic instability, and loss of rigidity along all directions.

the soft optical bands become increasingly unstable, until they form non-dispersive (flat) bands of unstable modes in a structure with $\epsilon_h \sim$ -0.1 (See Fig.5.5).

While the foregoing analysis establishes dynamical and shear-elastic instabilities of ZIF-8 crystal with ϵ_h, it is yet to determine if the ensuing soft modes drive its crystal-to amorphous transition on compression. To elucidate this, we distorted 2x2x2 strained (ϵ_h = -0.06 and -0.1) optimized supercells (2208 atoms) of ZIF-8, a random combination of eigenvectors of the unstable modes in their BZ (see Fig 5.5), and optimized them to their energy-minimum until the atomic forces were smaller than 10^{-5} Ha/Bohr. Quite clearly, both structures, with ϵ_h = -0.06 and -0.1, amorphize, as is evident from the featureless PDF of these structures (see Fig. 5.6a) beyond 6 $\mathring{A}$ [123], as well as significant framework-distortion (see Fig. 5.6b). The structurally disordered state retains the local coordination of ZnN_4 tetrahedra as well as IM-ring, but shows large deviation in the inter-tetrahedral structural parameters, that is, Zn-Zn distance and Zn-Im-Zn angle (see Fig. 5.6c), signifying folding or *crumpling* of the framework. Since the crystal-to amorphous transition with

compressive strains is the consequence of relaxation with respect to optical instabilities in crystalline ZIF-8, and is insensitive to pore volume, this corroborates the displacive nature of transition [124, 125], involving collective atomic rearrangements.

Ball-milling and nano-indentation of ZIFs have been associated with shear instability [53], as well as structural anisotropy [81]. Shear instability appears in ZIF-8 at ϵ_h = -0.035 (see Fig. 5.4). To understand relative contribution of hydrostatic and shear strains to amorphization during the ball-milling process, we first examined the structural features of the ball-milled a_m-ZIF-8 structure, modeled using Reverse Monte Carlo (RMC) method [50] with a box of 50.303 $\mathring{A}$ containing 512 ZIF-8 formula units (f.u.). Clearly, density of this structure corresponds to effective $\epsilon_h \approx$ -0.13 w.r.t pristine, p-ZIF-8 (12 f.u., a_o = 16.998 $\mathring{A}$), suggesting significant reduction in porosity during amorphization. Atomic structure of a-ZIF-8 involves large deviation in Zn-N bond lengths and N-Zn-N bond angles (Fig. 5.7) with respect to crystalline ZIF-8, indicating significant distortions of the ZnN_4 tetrahedra, in addition to large deviation in the network connectivity. Large asymmetry in distribution of Zn1-N-Zn2 angles indicates shear deformation during ball-milling, in addition to compressive strains. This prompted us to analyze the structural changes in the relaxed (2 x 2 x 2) ZIF-8 cell, compressed with varying rhombohedral shear strains (ϵ_r), and distorted with respect to *soft* unstable modes.

Since the modeled structure has significantly high density, we considered compressive strains ϵ_h = -0.06, -0.1 and -0.14, each deformed with ϵ_r = 0.06. Structural features of the distorted configurations (Zn-N bond lengths and

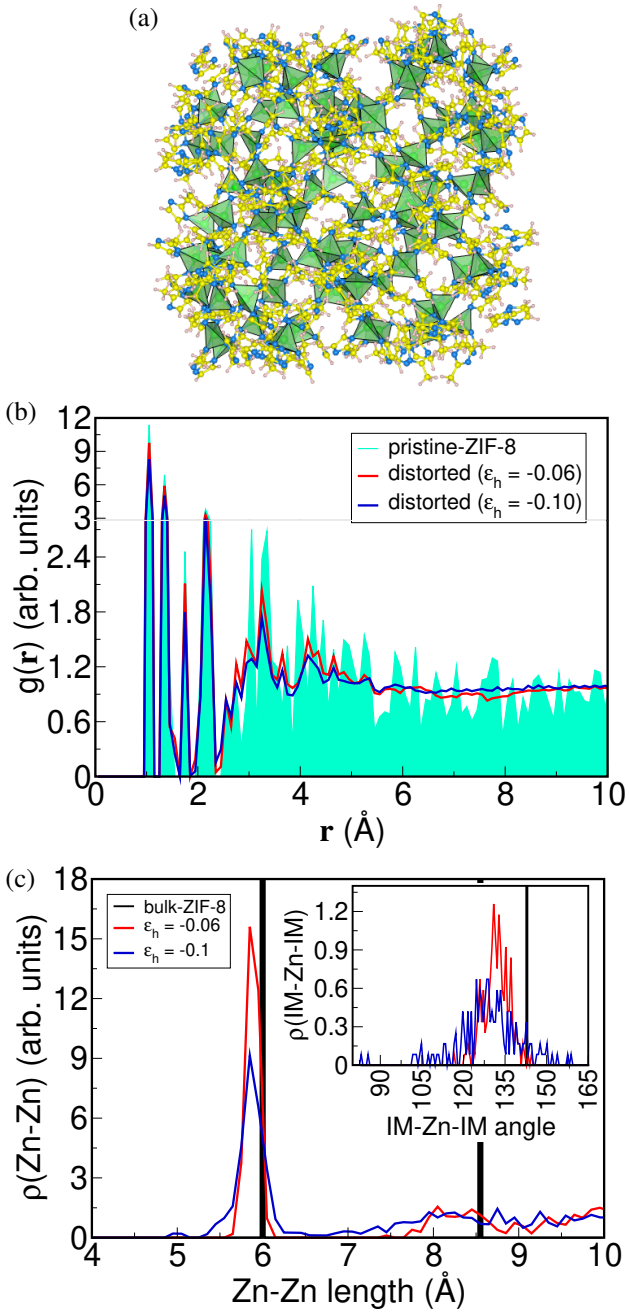

Figure 5.6: Structural signatures of amorphization of ZIF-8 on hydrostatic strains, ϵ_h =-0.06 and ϵ_h =-0.1: (a) structure of amorphous ZIF-8 with ϵ_h =-0.1, distorted (2 x 2 x 2) cell relaxed with respect to unstable phonons across the BZ, (b) PDF of amorphous structures exhibit short-ranged coordination environment of ZnN_4 tatrahedra and IM-rings, while loss of long-range order. Structurally, this is evident in large variations in Zn-Zn distances and Zn-Im-Zn framework angles, (c).

N-Zn-N angles) are obtained after their energy-optimization, and compared with the modeled *a*-ZIF-8 structure through RMC method (see Fig. 5.7). Interestingly, the compressed structures with large densities, ϵ_h = -0.1 and -0.14 show significant spread in Zn-N bond lengths and N-Zn-N angles, and are in better agreement with the *a*-ZIF-8 than the structures encasing a combination of hydrostatic and rhombohedral shear strains (Fig. 5.7). This indicates that destabilization of ZIF-8 is driven by spatially inhomogeneous shear deformation or sliding of different regions of the crystal with respect to each other, which originates from instability of transverse acoustic phonon bands at the zone boundaries (see Fig. 5.5b) [138,139]. Rhombohedral shear strains give rise to lower-symmetry distorted crystals at large $|\epsilon_h|$, as evident from sharp features in the distribution of Zn-N bond lengths in configuration with ϵ_h = -0.14 and ϵ_r = 0.06.

In conclusion, we have demonstrated the inherent *non-linear* elastic behavior of ZIF-8 due to higher-order moduli in its elastic strain-energy with respect to hydrostatic (ϵ_h) and rhombohedral shear (ϵ_r) strains, and coupling between long-wavelength TA and LA phonons. We show that ZIF-8 undergoes a shear instability (i.e. negative C_{44}) arising from higher-order mixed elastic moduli, and dynamical lattice instability emerging from negative slope of transverse phonon at hydrostatic strain $\epsilon_h \sim$ -0.04. Distortion of (2 x 2 x 2) supercells with randomized eigen-vectors of unstable phonons results in disruption of its long-range order leading to amorphization of ZIF-8 at large compressive strains. *Densified* *a*-ZIF-8 structure, modeled with RMC approach, shows good agreement with compressed distorted structure

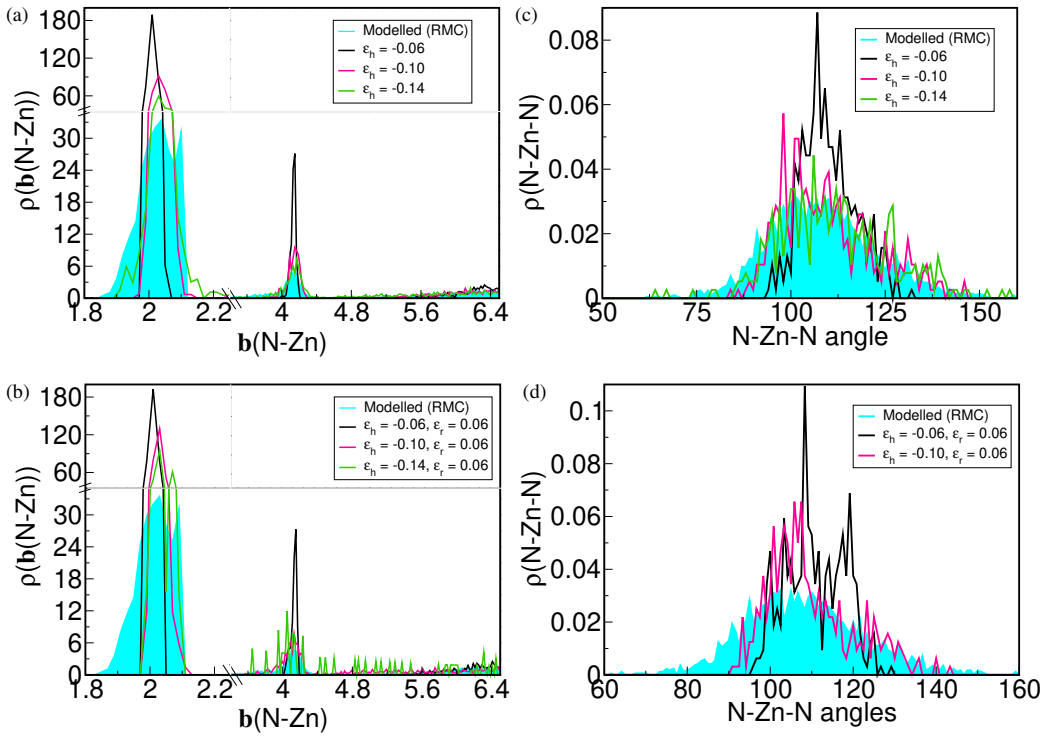

Figure 5.7: Distributions of structural parameters, Zn-N bond lengths (top panels) (a),(c) and N-Zn-N bond angles (bottom panels) (b),(d) of amorphized ZIF-8 upon ball-milling as modeled using RMC approach and comparisons with ZIF-8 structures simulated with (2 x 2 x 2) cells encasing varying degree of strains, and internal distortions

devoid of homogeneous shear strains ϵ_r, clearly indicating that spatially-heterogeneous, *cooperative* shear-sliding results in structural disorder, and eventually in amorphization of ZIF-8.

Chapter 6

Boson Peak in crystalline frameworks: A *not-so-peculiar* feature of glasses

6.1 Introduction

Deviation from T^3 dependence of specific heat capacity C(T) of insulators at very low temperatures (T $\sim$ 1 - 10 K) has been considered as a characteristic of amorphous (disordered) and glassy systems, with respect to their crystalline counterparts [140, 141]. In accordance to Debye model of specific heat, density of vibrational states $g(\omega) \propto \omega^2$ results in $C(T) \propto T^3$. Spectroscopic analysis of excess of low-energy excitations over Debye-type vibrations (i.e. collective modes reminiscent to sound waves in a medium) represents a peak in reduced density of states $g(\omega)/\omega^2$ at low ω, that manifests as a peak

in C(T)/T^3 at low-T in the calorimetric analysis. Boson Peak (BP) is a common reference to deviation from Debye law in glasses or amorphous systems. This *peculiar* feature was first observed as associated with a broad band ($\omega \in$ 30-120 cm^{-1}) in the Raman spectrum of fused quartz [142]. Crystals, however, exhibit acoustic excitations with linear dispersion $\omega \propto |\mathbf{k}|$ relation for $\omega <$ 1 THz and thus follow Debye model for thermal heat capacity (C $\propto T^3$). Unraveling the origin of excess vibrational modes at low frequencies that appear in glass and amorphous systems has been an active area of research for quite a long time. Earlier studies have attributed the low-energy modes in glasses to lattice disorder; positional or orientational [143–146], and librational or floppy modes [147–149]. Dynamics of glassy states has been associated with transition in the nature of transverse acoustic phonons from propagating to localized (or diffusive), that is, Ioffe-Regel limit [150], or anharmonic phonon-phonon interactions leading to acoustic damping [148,151].

Low-energy modes of disordered states (glass or amorphous) that dominate their thermodynamic properties at low-T (T $\sim$ 1 - 10 K) are largely associated with two distinct regimes of phonon spectrum of their crystalline forms: (a) localized nature of *soft* vibrational modes, for instance, liberations of rigid tetrahedra in SiO_2 glass at large wave-vectors $\vec{q}$ ($|\vec{q}|>$ 1.5-2 $\mathring{A}^{-1}$) [152], (b) scattering of acoustic modes of the crystal by structural inhomogeneities that appear beyond a coherence length in glasses [139,153]. The former are optical phonons with their *softness* originating from geometry and short-range order of the crystalline phase, the latter arises from structural disorder of the glass that couples with sound waves in the low-q region (or long wavelength limit).

Due to symmetry and periodicity of a crystal and an underlying Brillouin Zone (BZ), frequency dispersion ω *versus* $|\mathbf{q}|$ exhibits extrema or saddle points at BZ boundaries [154], that manifest as singularities in density of vibrational states $g(\omega)$ *versus* ω. Recently, signatures of BP in glasses were shown to be equivalent to van Hove singularity of the crystalline phase with the same chemical composition [58, 155]. This equivalence has been associated with lower packing-density of a glass [155] and is achieved by tuning the lattice dimension of the considered *poly-crystal*. While low-frequency phonons that constitute BP in glasses may resemble certain attributes of crystals, viz. van Hove singularity, elastic damping [156], broken inversion symmetries [157], we show here that the nature of atomic vibrations associated with BP is, by no means, universal [58, 150, 156].

6.2 Results and Discussion

We first present a rather *generic* appearance of Boson Peak, both in reduced density of vibrational states $g(\omega)/\omega^2$ *versus* ω and C/T^3 *versus* T at very low-T, in a class of ordered crystalline materials, metal-organic frameworks (MOFs). Through analysis of vibrational spectra of two model systems, MOF-5 and ZIF-8, within harmonic approximation, we show that BP is a characteristic vibrational feature of low-frequency vibrations at nanometer length scale, regardless of the degree (or nature) of disorder. Through analysis of phonons that contribute to BP in two crystals with distinct chemical and topological characteristics, our work provides evidence that disproves the notion that Boson peak is a *peculiar* feature of glasses or amorphous

systems. We highlight that coupling of acoustic phonons with low-frequency optical modes give rise to resonance and formation of *composite* vibrational modes at BZ boundaries, with $\frac{\partial\omega}{\partial q} \to 0$ and hence large contributions to BP. These modes exhibit both localized vibrations as well as cooperative rearrangements, depending on the structural topology. Further, mapping of the BP to van Hove singularity that corresponds to softest acoustic modes of the crystalline phase may be erroneous, since multiple soft-phonon bands may constitute the BP at low temperatures.

Structurally, MOFs consist of chemical polyhedra (tetrahedra or octahedra) centered at metal ions, connected by organic linkers, forming a relatively large unit cell, that hosts a multitude of internal degrees of freedom (optical phonons). With linear dimension of unit cell over 1 nm, the wave-vectors corresponding to the boundaries of their first BZ are about an order of magnitude lower than most simple systems, and is about 0.5 $\mathring{A}^{-1}$. This momentum vector $|\vec{q}|$ is comparable to magnitude of scattering vectors $\mathbf{Q}$ in inelastic X-ray or neutron scattering experiments on thermal properties of glasses, and correspond to acoustic attenuation (or scattering) by structural inhomogeneities [158]. Understanding the structural and dynamical features of glasses at the nano-metric length-scale pose a challenge since in this region wave-vector selection rules are not obeyed [159]. The vibrational modes of glasses with $q < q_c$ appear as a broad peak in $g(\omega)/\omega^2$ at low ω, thus masking their spectroscopic signatures. Therefore, study of vibrational properties of MOFs have a natural advantage in terms of wave-vectors quite relevant to the coherence length ζ_c (about a nano-meter) of glasses.

Atomic structures and crystal symmetries of MOF-5 and ZIF-8 are detailed in Chapter 1. Our calculations are based on density functional theory (DFT) and plane-wave pseudo-potential method as implemented in Quantum Espresso [160]. Electronic exchange-correlation energy is treated using generalized-gradient approximation as parameterized by Perdew-Burke-Ernzerhof [161], and the ionic core-valence electrons interactions are modeled with ultra-soft pseudopotentials. Kohn-Sham wave-functions are expanded in plane-wave basis truncated at energy cutoff of 580 eV. Integrations of Brillouin Zone are performed on a uniform 2 x 2 x 2 mesh of k-points. Variable-cell optimization of the two MOFs is carried out until the Hellman-Feynman forces on each atom are lower than 0.001 eV/Angstrom and normal components of stress becomes $\sim$ 0.01 kBar. Force-constant matrix, within harmonic approximation, is obtained with frozen-phonon method, while employing symmetry constraints to reduce the number of inequivalent atomic displacements in the cell. Normal-mode frequencies at arbitrary wave vectors, and the phonon dispersion are obtained using Phonopy code [101]. From the vibrational DoS g(ω), obtained by computing frequencies of modes on a fine q-mesh (21 x 21 x 21) in the first Brillouin Zone, we determine reduced DoS (g(ω)/ω^2) as well as temperature-dependent heat capacity C(T) of system of N atoms [162] within harmonic approximation, using:

$$C(T) = 3Nk_B\Delta\omega \sum_{\{w\}} \left[\left(\frac{h\omega}{2k_BT} \right)^2 sinh^{-2} \left(\frac{h\omega}{2k_BT} \right) g(\omega) \right] \tag{6.1}$$

Here the frequency interval $\Delta\omega = 0.0299$ THz (i.e. 1 cm^{-1}) and g(ω) follows the normalization condition $\sum_{\{w\}}$ g(ω)$\Delta\omega = 1$, $N_{MOF-5} = 106$ and N_{ZIF-8}

= 138.

Phonon dispersion of the MOFs viz. MOF-5 and ZIF-8 show multitude of modes at sub-THz frequency (Figure 6.1a,b) that manifest as peaks in $g(\omega)/\omega^2$ (Figure 6.1c), and result in a peak in $C(T)/T^3$ at low T (see inset of Figure 6.1c). While BP is generally absent in most crystalline solids, it is observed in framework materials like MOFs [163], for instance, $[(CH_3)_2NH_2]Zn(HCOO)_3$ at T $\sim 25K$. Its presence is typically associated with order-disorder structural transitions or inherent glassy behavior of MOFs [163]. In contrast to a single Lorentzian-type peak at low frequencies seen in the reduced density of states $g(\omega)/\omega^2$ of glasses at very low frequencies upto $\sim$1 THz (Fig.1 in Ref. [144]), $g(\omega)/\omega^2$ of MOFs exhibits several such peaks with reduced intensities at higher ω (Figure 6.1c). Indeed, $C(T)/T^3$ *vs.* T of MOF-5 obtained using TGA-DSC technique (Fig. 2 of Ref. [164]) provides an experimental evidence for excess heat capacity over that of Debye model, though at slightly higher temperatures, $T > 30K$. Interestingly, the intensity of strongest peak in $C(T)/T^3$ of MOFs is about an order of magnitude larger than in metallic glass or disordered high-entropy alloy [144].

In MOF-5, the first BP in $g(\omega)/\omega^2$ emerges from the saddle point of softest TA phonons at the BZ boundary, as well as flat optical branches (independent of $|q|$) that collectively give rise to a prominent van Hove singularity in $g(\omega)$ [154]. Couplings between the Γ-X TA branch and localized optical modes give rise to resonance and formation of *composite* modes at the BZ boundary with $\omega \sim 0.72$ THz. This is evident from the similar character of vibrations at X-point (edge of softest TA branch) and soft optical mode with $\omega \sim 0.75$ at the Γ-point, both with quasi-localized, non-propagating atomic displacements

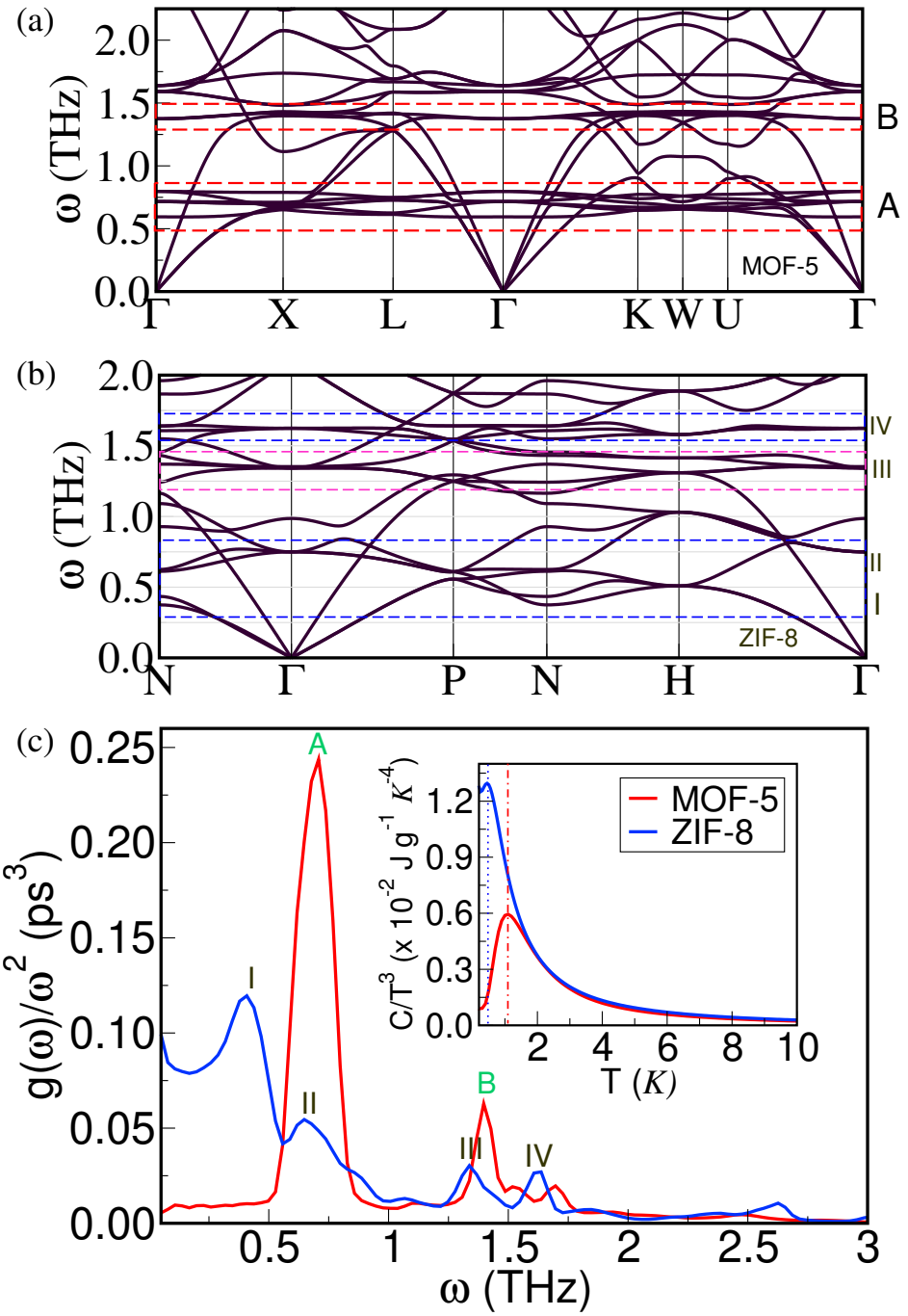

Figure 6.1: Low-ω vibrational spectra of MOF-5 and ZIF-8 and Boson peaks: (a) low-frequency phonon dispersion of MOF-5 exhibits flat non-dispersive phonon bands with $\omega < 1$ THz. Softest acoustic branch along Γ-X couples with optical branches leading to composite (or hybridized) modes at BZ boundary. (b) phonon spectrum of ZIF-8 shows very soft transverse acoustic branches with comparable slopes along different crystallographic directions. Longitudinal acoustic phonons in ZIF-8 couple strongly with dispersionless optical phonon bands at relatively higher frequency $\omega \sim 1.35$ THz. (c) Low-frequency bands in MOF-5 and ZIF8 manifest as peaks in $g(\omega)/\omega^2$ at very low-ω, as well as a peak in $C(T)/T^3$ at low-T (see inset), providing evidence for occurrence of BP in crystalline MOFs.

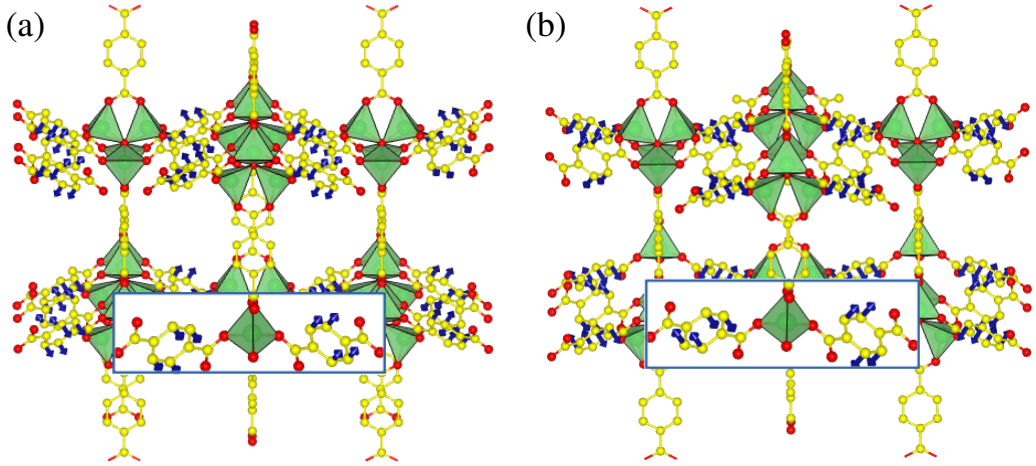

Figure 6.2: Low-frequency localized vibrations in MOF-5: (a) a *composite* mode at X-point arising from coupling of softest transverse acoustic modes along Γ-X with flat optical bands at the X-point, which exhibits buckling of benzene rings in the equatorial plane, (b) optical mode at Γ-point with $\omega \sim$ 0.72 THz, involving linker rotation.

(see Fig. 6.2). These modes exhibit buckling [165] and rotation, respectively, of benzene rings in the equatorial planes of carboxylate-octahedra, while the rings along the axial direction of the octahedra remain stationary. Similar rotational oscillations associated with low-energy intra-molecular modes have been reported in single crystal 2-bromobenzophenone (2-BrBP) [166], that exhibit deviations from T^3 dependence of C(T) at very low-T.

Higher-frequency modes, peak B in Fig. 6.1c, at $\omega \sim 1.4$ THz, represent asymmetric buckling or rotations of linkers (see Fig. 6.3), former being reminiscent to vibrations observed in network glasses [165]. This peak, significantly smaller in intensity, emerges primarily from the superimposition of acoustic branches at multiple zone boundaries (See Fig. 6.1a) with a *nearly*-flat optical band. To understand the relative contribution of each

peak in $g(\omega)/\omega^2$ of MOF-5 to the height of BP in $C(T)/T^3$ over the higher-frequency Debye modes, we computed $C(T)/T^3$ *versus* T *excluding* the acoustic branches below the van Hove singularity ($\omega > 0.55$ THz), the dominant peak ($\omega > 1.0$ THz), and the second peak ($\omega > 2.0$ THz) (see Fig. 6.4a). The acoustic branches with $\omega < 0.55$ THz have negligible contribution to BP in $C(T)/T^3$, as evident from the comparable values of $C(T)/T^3$ corresponding to $\omega > 0$ and $\omega > 0.5$ THz. While the most dominant peak in $g(\omega)/\omega^2$ (peak A in Fig. 6.1a) gives rise to a sharp peak in $C(T)/T^3$ at low-T, one-sixth of the height of $C(T)/T^3$ is contributed by high-frequency modes ($1.0< \omega < 2.0$ THz) (see Fig. 6.4a)! This clearly suggests that strong coupling of acoustic phonons with low-energy dispersion-less optical modes is responsible for a Boson Peak in $C(T)/T^3$ of certain crystals, like MOF-5 in the present case. Contribution of higher-frequency modes to the BP of MOF-5 reinforces that van Hove singularity, which is the discontinuity in $g(\omega)$ emerging from the softest acoustic phonons at a BZ boundary and *soft* flat dispersion-less phonons throughout the BZ [154], is inadequate in explaining the origin of BP in crystals. Moreover, correlation of BP with the van Hove singularity, as proposed in Ref. [58], arises primarily from the cell-dimension of the poly-crystal, about a nano-meter, that corresponds to relatively small wave vectors at the BZ boundary $|q|\sim$ 0.4-0.8 $\mathring{A}^{-1}$, quite relevant to thermodynamics of glassy and amorphous system at low-temperatures [158].

In ZIF-8 crystal, multiple peaks appear in $g(\omega)/\omega^2$, the strongest one occurring at vanishingly low $\omega \sim 0.4$ THz (see Fig. 6.1c). These excess low-frequency modes collectively give rise to a peak in C/T^3 at low-T (see

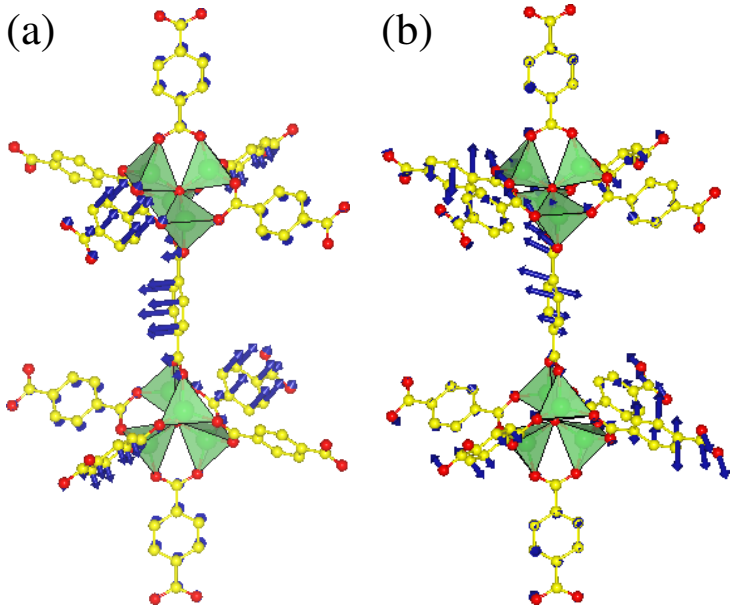

Figure 6.3: Relatively higher-frequency vibrations of MOF-5 ($1.25 < \omega < 1.5$ THz): (a) $\omega \sim 1.37$ THz involving asymmetric buckling, and (b) $\omega \sim 1.30$ THz involving asymmetric rotation of benzene linkers about the secondary building unit represented by the eigen-modes at the Γ- and L-point respectively.

Fig. 6.1c). The first two peaks (peak I and II in Fig. 6.1b) originate primarily from flattening of acoustic branches on the boundaries of BZ, the third peak (peak III) emerges from coupling of longitudinal acoustic branches with a dispersion-less optical branch, and the fourth peak (peak IV) represents relatively higher-frequency flat optical bands over the entire BZ. Acoustic phonons softer than the most dominant peak in $g(\omega)/\omega^2$ ($\omega < 0.32$ THz), exhibit a noticeable contribution to heat capacity, about half the height of $C(T)/T^3$ at low-T (see Fig. 6.4b). High-frequency peaks, however, contribute marginally to BP in $C(T)/T^3$, that is, less than one-tenth of the peak height arises from modes with $\omega > 1.1$ THz. This indicates that ZIF-8 derives its BP primarily from very low-frequency transverse acoustic (TA) phonons,

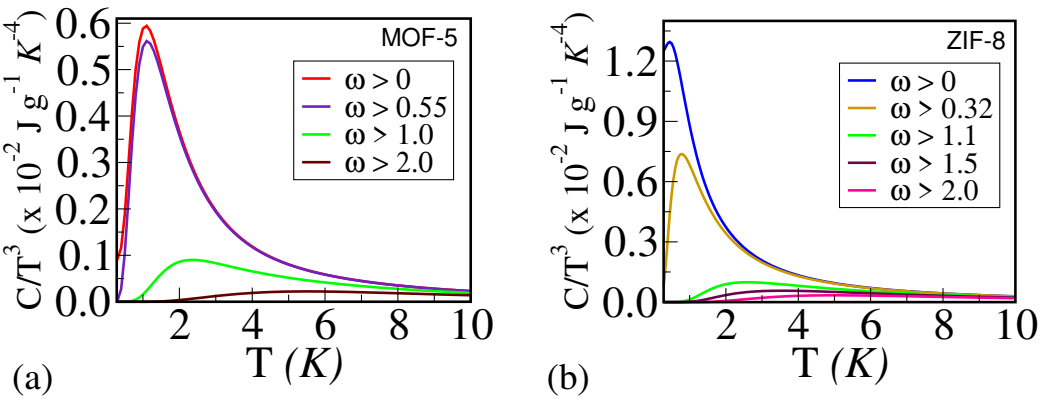

Figure 6.4: Contributions of low-energy acoustic and optical modes to BPs in: (a) MOF-5, where acoustic branches do not contribute to the peak in $C(T)/T^3$ at low-T, while modes that constitute first and the second peaks in $g(\omega)/\omega^2$ give rise to BP in $C(T)/T^3$, in the ratio of 5:1. (b) ZIF-8, where the acoustic branches with frequencies less than the van Hove singularity ($\omega <$ 0.32 THz) have a noticeable contribution to the peak in $C(T)/T^3$, as evident from the difference between the heights of peaks corresponding to $\omega > 0$ and $\omega > 0.32$ THz. In addition, soft modes with $0.32 < \omega < 1.0$ contribute to BP, while higher-energy modes of ZIF-8 ($\omega > 1.0$) essentially follow Debye model.

in contrast to MOF-5. Since acoustic phonons in different crystallographic directions at $|\vec{k}| \rightarrow 0$ and at the BZ boundaries collectively contribute to the peak in C/T^3 at low T, the Boson peak of ZIF-8 has a multi-scale origin: (a) from acoustic modes in the long-wavelength limit, and (b) structural inhomogeneities at length scales of the order of unit-cell dimensions.

The softest TA modes at N-point of the BZ of ZIF-8 (Fig. 6.1b) represents stratified chain-like atomic motions (see Fig. 6.5a) along the periphery of its square- and hexagonal-channels, separated by regions of very small atomic displacements. These resemble coherent atomic vibrations that constitute a BP in B_2O_3 glass [167], as well as shear bands in glasses that are responsible for their structural instability in response to external strains [168]. At

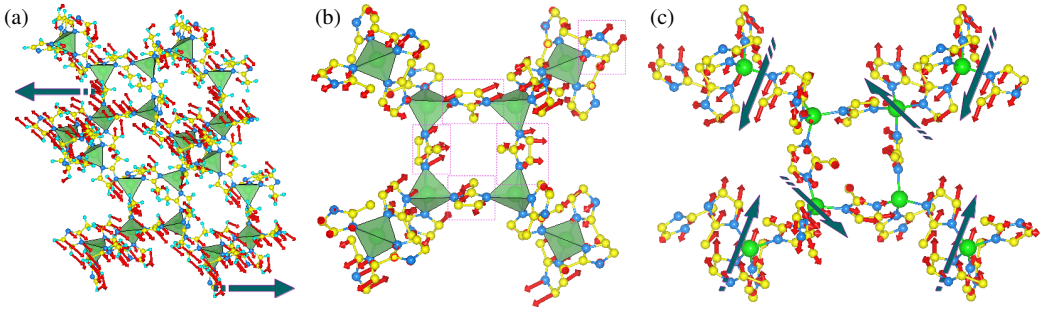

Figure 6.5: Nature of atomic vibrations of very low-frequency modes that constitute Boson peak of ZIF-8: (a) mode at N-point ($\omega \sim 0.37$ THz) shows shear bands, separated by atoms with very small atomic displacements, (b) mode at H-point ($\omega \sim 0.51$ THz) exhibits rippling, buckling, in-plane displacements and distortions of IM linkers about stationary metal centers, and (c) mode at H-point ($\omega \sim 0.75$ THz) exhibits cooperative motions of atoms in small regions of the crystal that slide with respect to each other.

H-point, the TA phonons exhibit rotations or rippling of organic linkers (IM rings) with respect to the stationary metal-ions (positioned at the center of Zn-N_4 tetrahedra) (see Fig. 6.5b). An optical-mode at the Γ-point with slightly higher frequency ($\omega = 0.75$ THz) (Fig. 6.1b) shows regions of cooperative atomic motion resulting in spatially-inhomogeneous shear deformation (see Fig. 6.5c) [139]. Nature of soft lattice vibrations of ZIF-8 suggests its tendency to undergo disordering through incoherent motion of IM-rings about the metal ions, or sliding of different regions of the crystal with respect to each other.

In conclusion, we demonstrate Boson peak(s) in crystalline metal-organic frameworks, (MOFs), that manifest as (a) a peak in $C(T)/T^3$ at very low-T, and (b) multiple peaks in reduced density of states $g(\omega)/\omega^2$ at low-ω through analysis of two model MOFs: MOF-5 and ZIF-8. Lattice vibrations associated with BP of MOF-5 represent *composite* modes resulting from strong

couplings between quasi-localized acoustic branches at the BZ boundary and localized *non-dispersive* optical phonons. In ZIF-8, however, BP emerges from shear modes, as well as buckling or rippling of IM-ring about the metal centers. This elucidates that vibrational modes that constitute the BP are not quite universal, and strongly depend upon the underlying topology and chemical interactions in the crystal. While BP was attributed to low-ω van Hove singularity in crystals in earlier studies, our work shows that it originates from soft acoustic modes, flat (non-dispersive) optical phonons, as well as relatively higher-frequency vibrations ($1 < \omega < 2$ THz), indicating that multiple strong discontinuities in the density of states g(ω) at low ω can, in principle, constitute BP, and give rise of deviations of C(T) from the Debye model.

Chapter 7

Ambient stable tetragonal and orthorhombic phases in penta-twinned bipyramidal Au microcrystals

7.1 Introduction

Noble metals, namely Ag, Pt and Au, exist in the *fcc* crystal structure. In recent years, they are increasingly being synthesized and stabilized in various morphologies, namely nano-ribbons, nano-wires, nano-sheets, nano-crystals or nano-tubes, for potential applications in catalysis, optics and plasmonics [169–172]. These morphologies belong to distinct symmetry classes, for instance, cubic, icosahedral [170], decahedral (or pentagonal bi-pyramidal)

[169], or do-decahedral [171], and exhibit significant differences in their surface area-to-volume ratios, degrees of *locked-in* stresses, and structural stability. With lateral dimensions in nano-scale, nano-wires or nano-sheets exhibit structural stresses [173], which tend to stabilize either through fragmentation or anisotropic growth into crystallites with larger sizes.

In particular, nano-particles with decahedral geometry are quite interesting [169]. While the cubic *fcc/hcp* structure has 6-fold symmetry of the (111) plane, the decahedron has planes with 5-fold symmetry representing spatially inhomogeneous atomic coordination at its base [174]. Stacking of these planes results in a configuration of *quin-tupled* twins intersecting along a single axis, giving rise to inherent stresses, that manifest as elastic strains in a structure with respect to the ground-state *fcc* configuration. The building unit of the decahedron crystallite is thus a body-centred orthorhombic (*bco*) phase [175], in contrast to body centred tetragonal (BCT) with $c/a = \sqrt{2}$ in the cubic *fcc* crystal.

Growth of decahedral nuclei along [011] into a nano-wire with lateral dimension in a few nano-meter and length about a few micro-meters stabilizes *non-fcc* phases, that appear as varying degree of strains in the core and surface region [176]. The spontaneity in deposition of subsequent shells of atoms in kinetically-driven growth is primarily to neutralize surface charges by accommodating addition atoms. In contrast to annealing of crystals, that results in enhanced ductility, nano-wires have been shown to exhibit fragmentation to nano-rods. This suggests that surface stresses in nano-sized nuclei act as *glue* for the layer-by-layer growth of penta-twinned crystallites.

In recent years, science and *art* of tuning the crystal-growth kinetics

relevant to unconventional morphologies and exploring the metastability of non-*fcc* phases of Au has fascinated our experimental collaborators, Prof. G. U. Kulkarni and group. A series of systematic studies on synthesis and characterization of pentagonal bipyramidal crystals of Au with length-scales in **micron** and lateral dimension ∼200-250 nm [177], have led to extraordinary stabilization of *bc(o,t)* phases of Au. This has extended the science of unconventional pseudo-symmetric crystals to a realm of length-scales where surface and elastic effects can co-exist, and allow structural strengthening while retaining the lucrative surface properties of the nano-crystals. In the present work[1], studies carried-out by Prof. Kulkarni's group demonstrated that the penta-twinned structure of the Au microcrystals [177] hosts *bc(o,t)* phases in the core, while being enveloped by high-index corrugated facets (hk0) (h or k > 2) along the length, and (111) closed-packed *fcc* at the tips. The non-*fcc* phases in Au bipyramids are highly stable in the ambient conditions. While they are stable under *e*-beam exposure, the strains in bipyramids could be released by annealing at elevated temperatures with minimal change in morphology. Stabilization of non-*fcc* phases in Au microcrystallites is sensitive to the kinetics of reaction, and favored within the temperature range 200-250^o. Within this range, the rate of thermal annealing is lower than the speedy growth of the microcrystallites resulting in strains locked in the form of non-*fcc* phases. Here, we present a *first-principles* theoretical analysis of the stability of non-*fcc* phases as indexed from the XRD-powder pattern

[1] **Ambient stable tetragonal and orthorhombic phases in penta-twinned bipyramidal Au microcrystals**,
Gangaiah Mettela, Meha Bhogra, Umesh V. Waghmare, and Giridhar U. Kulkarni
Journal of the American Chemical Society 2015 137 (8), 3024-3030

of Au-microcrystallites. From the estimation of temperature-dependent free energies of elastic distortions in the *fcc* structure, we confirm the presence of such phases and also present a *soft* mode-based model that captures the trends in the stability of non-*fcc* phases of noble metals, in general.

Our calculations are based on *first-principles* density functional theory (DFT) as implemented in Quantum Espresso (QE) package [160] with Perdew-Zunger functional [178] of the exchange-correlation energy approximated with a local density approximation (LDA). The interaction between ionic core and valence electron is represented with projector augmented wave (PAW) method [179]. Plane-wave basis set is truncated with an energy cutoff of 40 Ry in the expansion of KohnSham wave functions (and a corresponding cut-off of 400 Ry for charge density), and integrations over Brillouin Zone (BZ) are sampled with a uniform (24 x 24 x 16) k-mesh for the *bct* type of unit cell.

The elastic constants of *fcc* Au were calculated from strain-energy as:

$$C_{ij} = \frac{1}{V_o}\frac{\partial^2 E_{total}}{\partial \epsilon_i \epsilon_j} \tag{7.1}$$

where E_{total} is the total energy, V_o is the volume of unit cell and ϵ_i is a strain component in Voigt notation. For normal strains, the elastic compliance matrix with cubic symmetry is written as:

$$\mathbf{C} = \begin{pmatrix} C_{11} & C_{12} & C_{12} \\ C_{12} & C_{11} & C_{12} \\ C_{12} & C_{12} & C_{11} \end{pmatrix} \tag{7.2}$$

with C_{11} and C_{12} as independent constants. Dynamical matrices (DMs) and phonon frequencies are obtained using the DFT linear response method [102] on a uniform (4 x 4 x 2) mesh of q-points, which are Fourier-interpolated to wave vectors on a finer mesh used in determination of Helmholtz free energies as a function of temperature within a harmonic approximation:

$$F_{vib} = E_{total} + \frac{k_B T}{N_q} \sum_{q,i} \log \left[2 \sinh \left(\frac{\hbar w_{iq}}{2 k_B T} \right) \right], \tag{7.3}$$

where N_q is the number of **q**-points on (20 x 20 x 12) mesh in the BZ, and ω_{iq} is the frequency of i^{th} normal mode at a wave-vector **q**.

XRD peak analysis revealed the presence of non-*fcc* phases with compression along c-axis and expansion along a and b axes. In the *bct* form of *fcc* lattice, $a' = b' = a/\sqrt{2}$ and $c' = c$, where a, b, and c are the lattice parameters of *fct*. In *fcc* structure, $c'/a' = \sqrt{2}$. Experimentally obtained lattice parameters of the *bct* structure are, $a' = b' = 2.9062\mathring{A}$ and $c' = 4.0503\mathring{A}$ with $c'/a' = 1.394$ (deviation of -1.44% from the *fcc* structure). The indexed lattice parameters of *bco* structure are $a' = 2.9165\mathring{A}$, $b' = 2.8907\mathring{A}$, and $c' = 4.0337\mathring{A}$ with $c'/a' = 1.383$ and $c'/b' = 1.395$, with strain along the a-axis slightly higher than that along b. The *bct* volume is ∼0.62% higher, while that of *bco* is higher by only 0.03% with reference to the unstrained *bct* ($c'/a' = \sqrt{2}$) structure.

7.2 Theroretical Analysis

We analyzed the non-*fcc* (*bct* and *bco*) phases of Au-microcrystallites treating them as strained forms of the *fcc* structure. The structural response governing these small strains (within 2%) is determined by elastic moduli (see Table 1) of *fcc* Au. Our calculated estimates of C_{11} and C_{12} for Au are 210 and 177 GPa respectively, which are in good agreement with the corresponding observed values of 202 and 170 GPa [180]. The value of $\frac{C_{11}-C_{12}}{C_{11}+2C_{12}}$, which measures the propensity to undergo tetragonal distortion over uniform compression is very small (= 0.058) for Au, suggesting that Au has a tendency to exhibit *fcc* to *bct* transformation in the presence of normal strains. A higher value of C_{44} (45 GPa) as compared to $C_{11} - C_{12}$ (also referred to as C') further suggests the preference for deformation through tetragonal strains (ϵ_{xx}, ϵ_{yy}, ϵ_{zz}) over shear strains (ϵ_{xy} or ϵ_{yz}). For Au, the eigenvalues of elastic constant matrix $\mathbf{C}$ (Equation 7.2) are $\lambda = \{542, 32, 32\}$ GPa, and the eigenvectors of $\lambda = 32$ GPa give two soft modes of deformation of the *fcc* Au: $\vec{d_1} = \epsilon_{xx} = \epsilon_{yy} = -(\frac{\epsilon_{zz}}{2})$ and $\vec{d_2} = \epsilon_{xx} = -\epsilon_{yy}, \epsilon_{zz} = 0$. The former results in a *bct*, while the latter (or a linear combination of the two) results in a *bco* structure.

We determined the energy landscape of *bct* and *bco* structures obtained by imposing normal strains ϵ_{xx}, ϵ_{yy} and $\epsilon_{zz} \in$ [-0.01, 0.01]. The *bct* structure with strain along the *soft* mode $\vec{d_1}$ is a local minimum of energy as a function of ϵ_{xx} and ϵ_{yy} at a given ϵ_{zz}, and is within 0.5 meV/atom relative to *fcc* Au ($c'/a' = \sqrt{2}$) (See Fig. 7.1). Such a small energy difference suggests that certain *bct* configurations can become energetically favorable in the presence

of internal *geometric* strains emerging from constrained morphology of the particle. Further, the energy landscape for strains $\epsilon_{xx} = \epsilon_{yy}$ at $\epsilon_{zz} = 0$ is rather shallow and exhibits local minima near ϵ_{xx} = -ϵ_{yy} with ΔE $\leq$ 1.0 meV/atom. For $\epsilon_{zz} \neq 0.0$, the *bco* configurations resulting from deformation $\vec{d_3} = p\vec{d_1} + q\vec{d_2}$; $p, q \in Z$ (Z being an integer) have lower energies than the other *bco* structures, such as the *bco* structures with $\epsilon_{xx} = 0.006$, $\epsilon_{yy} = 0.002$, ϵ_{zz} = -0.008 and ϵ_{xx} = -0.008, ϵ_{yy} = -0.002, $\epsilon_{zz} = 0.01$ (See Fig. 7.1). The aforementioned analysis shows that the structures resulting from imposed strains along $\vec{d_1}$, $\vec{d_2}$ or $\vec{d_3}$ have lower energies at $0K$ than the other strained bct and bco configurations (including the ones observed in Au microcrystallites).

Analysis of vibrational spectra of the strained configurations supports the observation of non-*fcc* (*bct* and *bco*) phases with $c'/a' < \sqrt{2}$ in Au microcrystals (See Fig. 7.2). Configurations with strains along $\vec{d_1}$, *bct* I ($\epsilon_{xx} = 0.006$, $\epsilon_{yy} = 0.006$, ϵ_{zz} = -0.012) and *bct* II (ϵ_{xx} = -0.006, ϵ_{yy} = -0.006, $\epsilon_{zz} = 0.012$), show softening of the longitudinal acoustic (LA) modes (Mode I in Figure 7.2b) along Γ-S (1/2,1/2,0) in bct I and hardening in bct II, suggesting possible stabilization of bct I (with negative ϵ_{zz}) through thermal fluctuations in the $a' - b'$ plane. Deformation $\vec{d_2}$ present in bco I ($\epsilon_{xx} = 0.005$, ϵ_{yy} = -0.005, $\epsilon_{zz} = 0.0$) preserves the volume of fcc structure and thus shows negligible changes in the vibrational spectra.

The observed non-*fcc* phases, *bct* III ($\epsilon_{xx} = 0.007$, $\epsilon_{yy} = 0.007$, ϵ_{zz} = -0.008) and *bco* II ($\epsilon_{xx} = 0.011$, $\epsilon_{yy} = 0.002$, ϵ_{zz} = -0.012) with $c'/a' < \sqrt{2}$ exhibit significant softening of LA mode along Γ-S and transverse acoustic (TA) modes along Γ-T (1/2,0,1/2) and Γ-U (0,1/2,1/2) directions (Figure 7.2d), indicating their stabilization through shear strain (ϵ_{xz}) fluctuations.

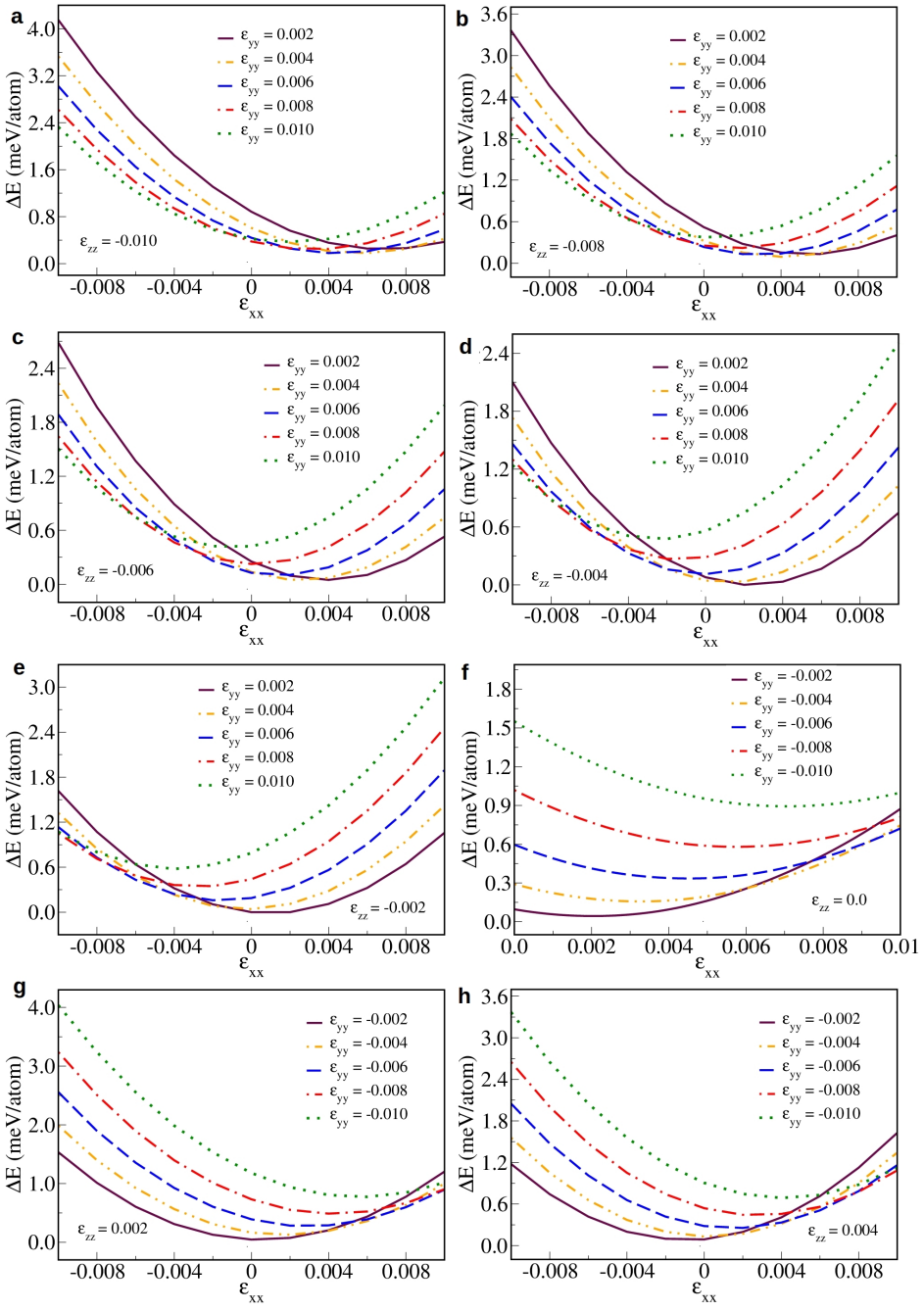
a
b
c
d
e
f
g
h
ΔE (meV/atom)
ε_xx
ε_yy = 0.002
ε_yy = 0.004
ε_yy = 0.006
ε_yy = 0.008
ε_yy = 0.010
ε_yy = -0.002
ε_yy = -0.004
ε_yy = -0.006
ε_yy = -0.008
ε_yy = -0.010
ε_zz = -0.010
ε_zz = -0.008
ε_zz = -0.006
ε_zz = -0.004
ε_zz = -0.002
ε_zz = 0.0
ε_zz = 0.002
ε_zz = 0.004

Figure 7.1

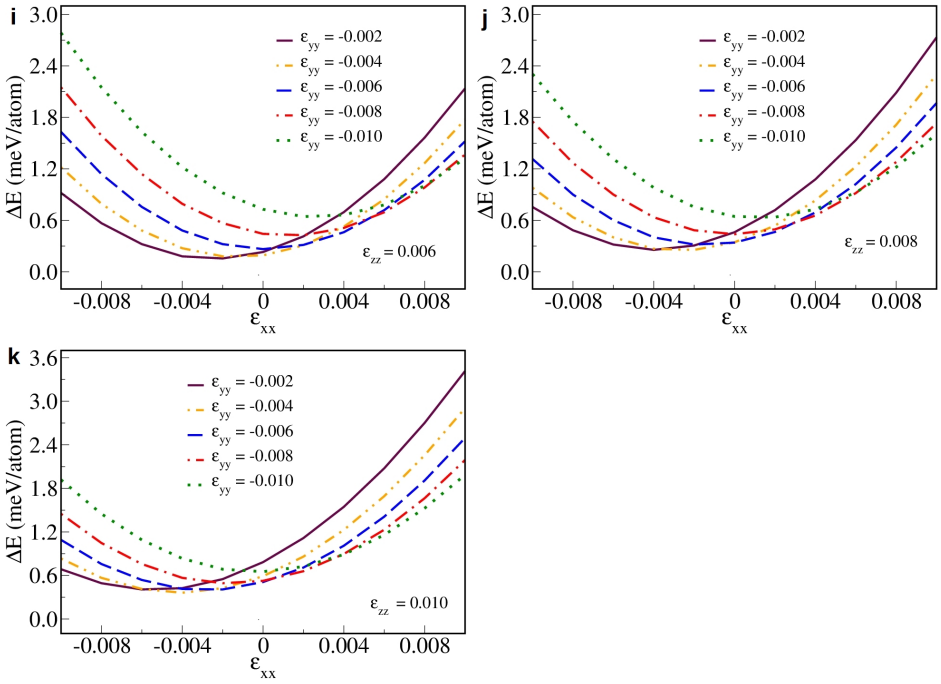

Figure 7.1: (*contd*) Energy landscapes of strained non-fcc ($bc(o,t)$) configurations at different ϵ_{zz} values: (a)-(e) $\epsilon_{zz} < 0.0$, (f) $\epsilon_{zz} = 0.0$ and (g)-(k) $\epsilon_{zz} > 0.0$

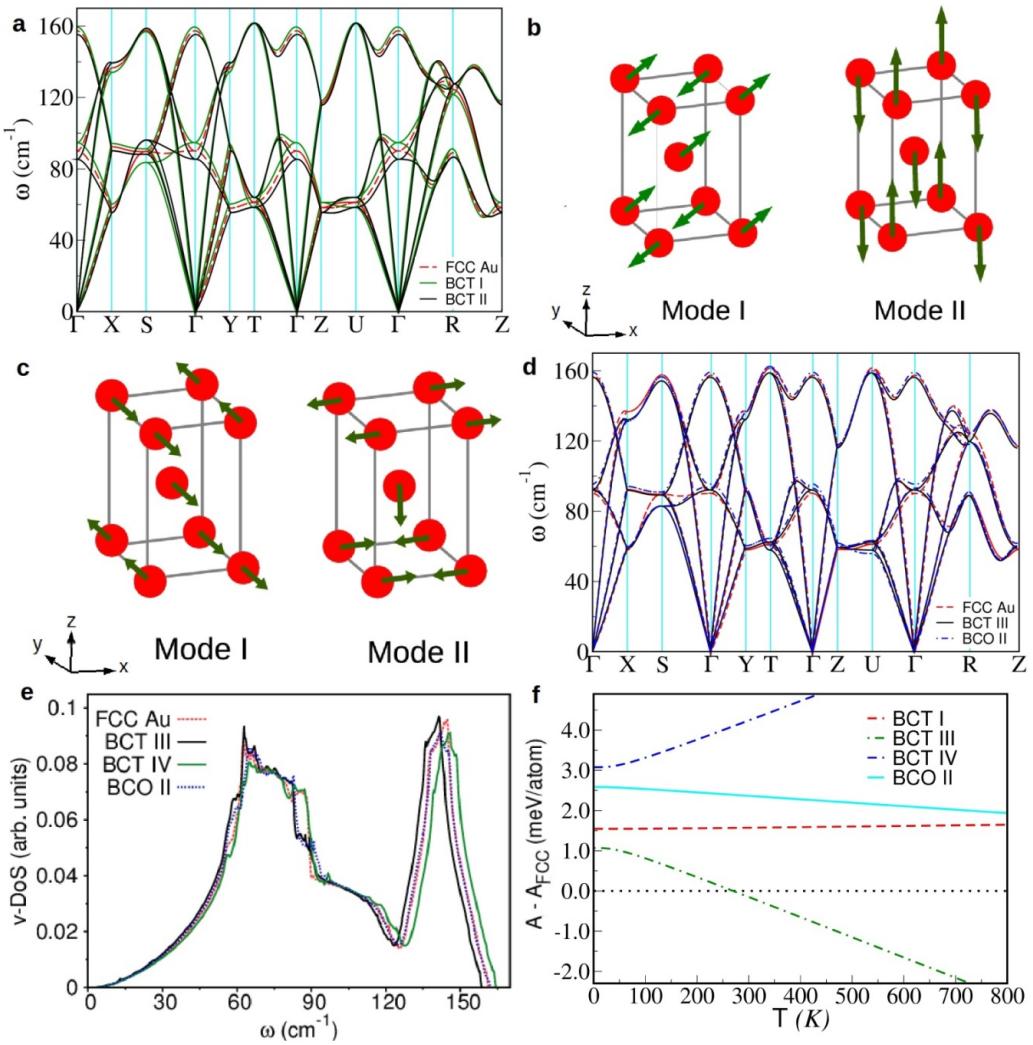

Figure 7.2: Phonon spectra of *fcc*, *bct* I and *bct* II configurations, (b) eigenvectors of low-energy acoustic modes at S($\frac{1}{2}$,$\frac{1}{2}$,0) point (mode I softens in *bct* I and hardens in *bct* II), (c) eigenvectors of low-energy transverse acoustic modes at T($\frac{1}{2}$,0,$\frac{1}{2}$) point, (d) phonon spectra of *bct* III and *bco* II, (e) phonon density of states (v-DoS) of non-*fcc* configurations compared with that of *fcc* Au, and (f) vibrational contribution to free energies of non-*fcc* configurations with reference to the *fcc* structure of Au at finite temperatures.

In addition, *bct* III shows softening of high-energy optical modes (120-160

cm^{-1}). An increase in the number of low-frequency modes of non-*fcc* configurations with $c'/a' < \sqrt{2}$ (*bct* I, *bct* III and *bco* II) and decrease for $c'/a' > \sqrt{2}$ (*bct* IV: ϵ_{xx} = -0.007, ϵ_{yy} = -0.007, ϵ_{zz} = 0.008) are evident in density of vibrational states.

The contribution of soft vibrational modes (Figure 7.2d) to free energies of the non-*fcc* configurations is significant and stabilizes them at finite temperatures (T > 300 K), supporting the occurrence of certain *bct* and *bco* phases (*bct* III and *bco* II) in geometrically strained Au microcrystallites through thermal activation (see Figure 7.2f). This is in contrast to the *bct* IV configuration ($c'/a' > \sqrt{2}$) which destabilizes with temperature, clearly showing a strong effect of c'/a' ratio on the stability of strained phases. The free energies of configurations with strains along $\vec{d_1}$ and $\vec{d_2}$ remain essentially unchanged by thermal effects. This can be traced to significantly smaller stresses in the configurations obtained with $\vec{d_1}$ and $\vec{d_2}$ modes of deformation, but higher induced stresses in *bct* III, *bct* IV and *bco* II structures (σ_{xx} of -1.3, 1.5, and -0.8 GPa respectively). Thus, the induced deviatoric stresses are relevant to thermal stabilization of non-*fcc* phases of Au with ($c'/a' < \sqrt{2}$).

Annealing at elevated temperatures releases the internal stresses in Au bipyramids through relaxation of strains associated with the *bct* and *bco* structures. Within the elastic range, the smaller the induced stresses, the slower is the rate of relaxation of strains [181]. Thus, reduction of non-*fcc* phases to *fcc* Au on annealing occurs at relatively high temperatures ($\sim 500^o$C).

The relevance of vibrations to non-*fcc* phases of Au was noticed earlier.

Table 7.1: Coefficients of terms relevant to time-temperature relationship

Metal	C_{11} (GPa)	C_{12} (GPa)	C_{44} (GPa)	C_{11}-C_{12} (C') (GPa)	$\frac{C_{11}-C_{12}}{C_{11}+2C_{12}}$
Au	**210**	**177**	**45**	**33**	**0.058**
Ag	132	97	51	35	0.107
Pd	234	176	72	58	0.098
Pt	358	254	77	104	0.120

Note: The values in **bold** are determined in the present work.

Soft vibrational modes identified here constitute elastic signatures relevant to *fcc* to non-*fcc* phase transition, which capture the trends in the stability of non-*fcc* phases in other noble metals. The lowest value of $\frac{C_{11}-C_{12}}{C_{11}+2C_{12}}$ for Au (0.058) indicates its stronger tendency to undergo tetragonal (or orthogonal) distortion over uniform compression, when compared with other noble metals, namely, Ag, Pd, and Pt (see Table 1) [180]. Comparable values of $C_{11} - C_{12}$ or C' for Au and Ag suggest a feasibility of tetragonal phase in both these metals for small structures, consistent with the occurrence of *bct* phase in Ag nanowires observed at ambient pressure. Lastly, higher shear elastic constant C_{44} of Ag, Pd, and Pt as compared to Au further suppresses the thermal stabilization of their non-*fcc* phases due to weaker contribution of the transverse (or shear) acoustic modes to free energy.

In conclusion, theoretical calculations elucidate temperature dependence of the free energies of certain non-*fcc* (*bct* and *bco*) structures and highlight the role of internal stresses and relevance of soft modes in their stabilization. The analysis of elastic compliances reveals how $\frac{C_{11}-C_{12}}{C_{11}+2C_{12}}$ singles Au out from the noble metals in its propensity to form *bct* and *bco* structures when subjected to strains inherent to the pentagonal-bipyramidal morphology.

Chapter 8

Ion-irradiation induced thermal *electronic* wave and homogeneous structural transformations of non-*fcc* phases of Au microcrystallites

8.1 Introduction

Our experimental collaborators, Professor G.U. Kulkarni and group have been involved in tuning the synthesis of unconventional non-*fcc* phases of Au at the micro-scale. This has led them to achieve as high as 92% mole fraction of non-*fcc* phases in pentagonal bipyramidal Au microcrystallites. The penta-twinned structure hosts *bc(o,t)* phases [177] in its core [182], while

being enveloped by high-index corrugated facets (hk0) (h or k > 2) along the length, and (111) planes of closed-packed *fcc* at the tips. The appearance of these metastable phases, as characterized by varying degrees of elastic strains with respect to *fcc* Au has been attributed to the kinetic arrest of residual stresses in the microcrystallites [183] during their growth in the intermediate temperature range (∼200-250^{o}C), essentially due to sluggish rate of thermal diffusion. Stability of *bc(o,t)* phases in the microcrystallites at ambient conditions is quite remarkable, with their unscathed existence even after 6 years of their synthesis!

Recently, Prof. Kulkarni's group has been exploring processes/perturbations that may induce variations in the *locked-in* stresses, and either destabilize the non-*fcc* phases transforming to native *fcc* Au or stabilize other non-*fcc* configurational states in its wake. This would enable them to tailor the phase structure opening up prospects of wider applications of Au microcrystallites. In the present work, they have carried out a systematic study of time-dependent irradiation of Au microcrystallites with low-energy Ar^+ ions. With ion energies (1-5 keV) typically used for cleaning surfaces in high vacuum, they showed that the prolonged exposure results in a controlled transformation of one metastable phase to another at the core of the crystallites, from *bco* → *bct* → *bct1*, which differ primarily in the magnitude of *locked-in* strains along the [001]-direction. In contrast to thermal annealing that gives rise to spatially non-homogeneous elastic strains as observed from significant XRD peak broadening (see Fig. 8.2), structural changes induced by Ar^+ irradiation emerge as uniform characteristic strains *locked* across the entire microcrystallites with a thickness of ∼200-250 nm. XRD patterns of

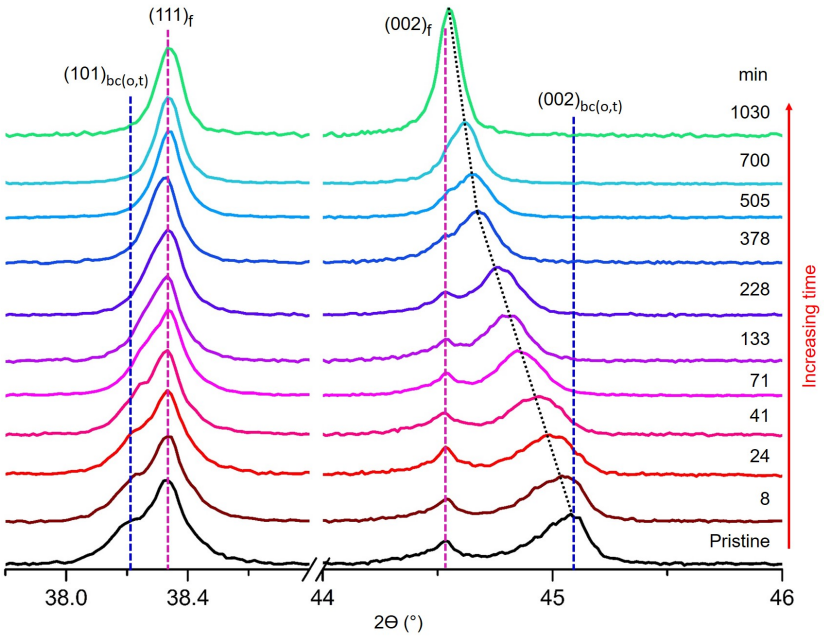

Figure 8.1: XRD patterns collected after Ar^+ bombardment at 1.2 keV energy with emission current of 10 mA with irradiation-time. The magenta lines show the length and at different positions width of the bipyramid. Black line shows new shifted peaks [5].

the irradiated samples with varied time of exposure show contiguous shifts in the (002) peak and lowering of FWHM values, indicating enhanced degree of order in irradiated microcrystallites on prolonged ion exposure (see Fig. 8.1).

8.2 Results and Discussion

Here, we present a plausible mechanism that elucidates the ramifications of low-energy ion irradiation on targets with dimensions larger than nano-scale, and percolation of ion-energy beyond a few nanometers from the surface. We propose that the transient thermodynamic state at the cascade-core interface

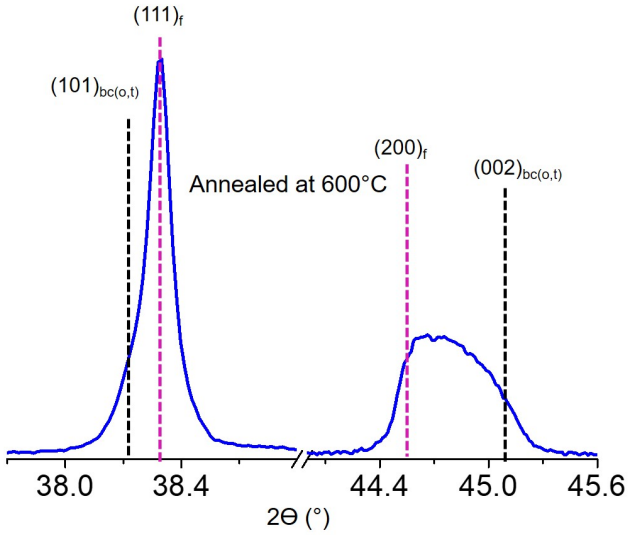

Figure 8.2: (Evolution of XRD-peak widths on annealing of Au microcrystallites. The peaks broaden with increase in annealing temperature, in contrast to narrow peaks observed on prolonged ion-exposure [5].

manifests as a time-lag between heat flux and temperature-gradient, invoking the non-Fourier mechanism of heat conduction by electrons on ion-irradiation of Au microcrystallites. Electrons in *non-equilibrium* penetrate into the core as a *thermal wave* at a finite speed, which is determined by the time-lag at the cascade-core interface. Longer is the time-lag, slower is the wave. This *slow* thermal wave of electrons can travel undeterred to ∼200-250 nm into the particle, a distance significantly larger than the mean-free path of electrons (∼40 nm) in Au. Through first-principles theoretical analysis, we show that the *hot* excited electrons in the *core* of microcrystallites tune the elastic strains of non-*fcc* phases, and explain structural changes from *bct* → *bct-I* → *fcc*, as obtained from indexing of XRD powder-diffraction pattern.

Metastable *bct-I* structures that emerge on varied durations of ion-irradiation

show a systematic deviation primarily in c, with minimal changes in a' and b' parameters, and manifest as monotonous shifts in (002) XRD-peak positions with respect to those of un-irradiated (pristine) Au microcrystallites. This indicates a correlation between *metastable* elastic strains (along [001] in present case) and consecutive irradiation intervals, with insignificant degree of random structural distortions or stochasticity in the process. Further, shifts in (002) XRD-peaks towards lower 2θ values, with no signs of peak-broadening suggest penetration of thermal energy into the entire microcrystallite (thickness ∼200 - 250 nm) (see Figure 8.1), and minimal fraction of energy dissipation due to phonon-phonon interactions. The effect is further evident from the additive nature of irradiation-induced structural transitions observed in Au microcrystallites, wherein a continuous exposure to Ar^+ beam (3 keV, 1 mA) for 65 min brings in a similar transformation as the three intermittent exposures at t = 10, 25 and 65 min, each separated in time by ∼8 hours [5]. "Quenching" of internal structure at each interval of Ar^+ irradiation, insensitive to changes at the surface due to vacuum transfer, suggests a separation of the "core" of the microcrystallite from its corrugated surface. This is in contrast to structural changes observed on thermal annealing, which give rise to a broadened XRD peak (see Fig. 8.2), suggesting a rather non-homogeneous spatial distributions of elastic strains. Disparate nature of structural transformations in Au microcrystallites on ion-irradiation and annealing is quite puzzling and requires a deeper understanding of the mechanism of heat-transfer active at very short times (of the order of 10^{-12} sec, or at time-scales of electron-electron relaxation times (10^{-10}-10^{-9} sec).

Thermal conductivity of metals has a contribution from heat transfer

by its conduction electrons. Annealing at high temperatures gives rise to enhanced activity of lattice vibrations, due to higher rate of electron-ion collisions and reduction of mean-free path of electrons in the medium [184], thus limiting the thermal conductivity. Heat dissipation from electrons to lattice involves strong electron-phonon [185] interactions, resulting in greater degree of lattice disorder in the annealed samples. This spatial disorder appears as broad XRD peaks, with respect to as-synthesized particles.

While the understanding of structural transformations upon thermal annealing is relatively straightforward, absence of peak-broadening and enhanced spatial homogeneity in ion-irradiated samples, with thickness exceeding the mean-free path of electrons in Au by about an order of magnitude, is quite intriguing. Further, the evolution of elastic strains along the [001] direction of *bc(o,t)* phases, with minimal structural randomness, cannot be explained by heat-transport mechanism based on *macroscopic* continuum-based Fourier diffusion model, hence a compelling need for alternative explanation. Ion-irradiation of microcrystallites, that exhibit a corrugated surface [177] with relatively low atomic density, would initially tend to reduce the size of voids to recover the atomic density of Au at the surface, and subsequently lead to rise in the number density of recoil atoms. Sluggish changes in the core structure during the initial few minutes ($\sim$8 min for 1.2 keV, which is significantly shorter for higher energy ions, E $>$ 1.2 KeV) of ion-exposure affirm the initial *preconditioning* of non-closed packed surface layers. Resulting distortions of the lattice or displacement cascade with high defect density near the surface (i.e. vacancies, interstitials, residual stresses) [186] leads to diminished mean free path of electrons λ and sharp decline in their thermal

diffusivity, by about two orders of magnitude, as seen in MD simulation of ion-irradiation of Ag [6]. High rate of inelastic ion-target collisions [187] results in *heating-up* of this locally inhomogeneous region, l_{ion} $\sim 10^{-7}$ cm, to very high temperatures [188].

With the core essentially in the ambient state beneath the collision cascade, large temperature-gradient across the cascade-core interface results in a thermal discontinuity. This characterizes a *transient* non-equilibrium state [189], at small time scales, wherein heat flux ($\mathbf{q}$) across the interface *lags* the temperature-gradient (∇T) between the cascade and the core by time τ. Introduction of τ in the Fourier model of heat conduction appears as: $q(r, t+\tau) = -K\nabla T(r, t)$ [190], where r and t are space and time variables, and K is the thermal conductivity of Au in the crystallite-core.

For small τ, the resulting spatio-temporal heat flux *q(r,t)* and temperature *T(r,t)* are:

$$q(r, t) + \tau \frac{\partial q(r, t)}{\partial t} = -K \bigtriangledown T(r, t) \tag{8.1}$$

From continuity equation $-\nabla.q(r, t) = c_p \frac{\partial T(r,t)}{\partial t}$, heat response $q(r, t)$ in non-equilibrium state can be expressed in terms of temperature-gradient as:

$$\bigtriangledown^2 T(r, t) = \frac{1}{D}\left[\frac{\partial T(r, t)}{\partial t} + \tau \frac{\partial T^2(r, t)}{\partial^2 t}\right] \tag{8.2}$$

where, D is the thermal diffusivity of the medium, $D = K/c_p$. Equation 8.2 has a $\frac{\tau}{D}\frac{\partial^2 T(r,t)}{\partial t^2}$ term added to the Fourier-diffusion equation, which signifies transmission of waves of temperature with a speed $C^2 = \frac{D}{\tau}$. If the phase-time lag τ is finite, that is, heat flux response to a thermal discontinuity is insufficient, the speed C of the wave is bound to decrease. Thus, *hot* excited

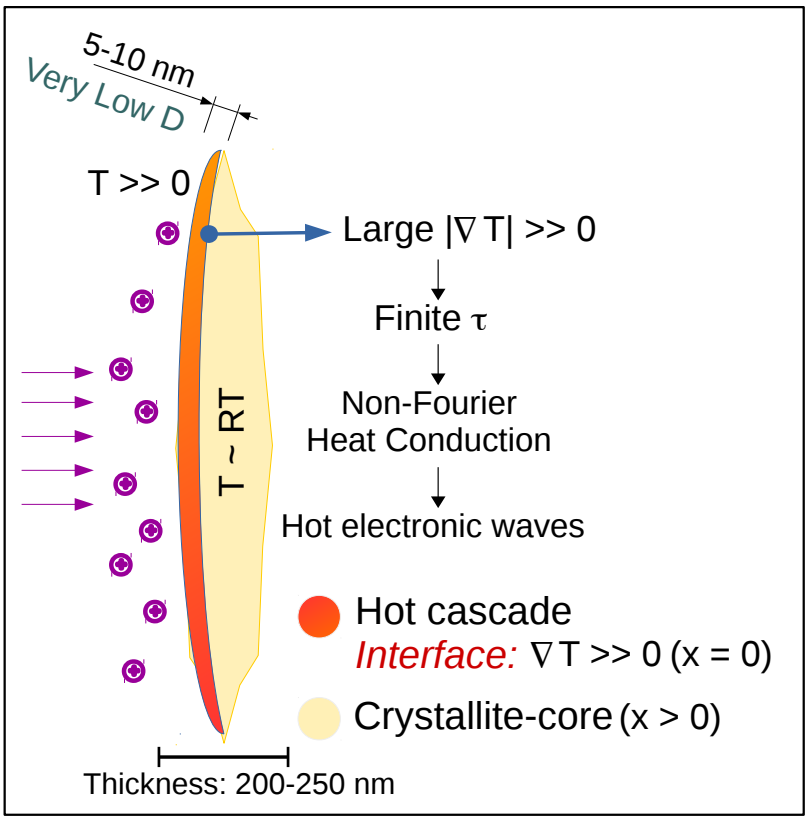

Figure 8.3: Genesis of *wave-like* heat-transfer on ion-irradiation of Au microcrystallites

electrons, heated to temperature in the order of 10^5 K within the cascade due to increased electron-ion coupling strength [185], travel across the interface and permeate into the core [191] as a *thermal-wave*.

Heat-transfer mechanism described by the hyperbolic equation (Equation 8.2) has been shown to arise from electron-ion non-equilibrium during short-pulse laser heating [192]. While finite velocity of heat propagation has been observed in response to non-equilibrium state of electron-lattice system at short-times, its genesis in non-Fourier heat transfer and wave-nature has hitherto not been highlighted. For instance, Brorson *et. al.* [193] showed

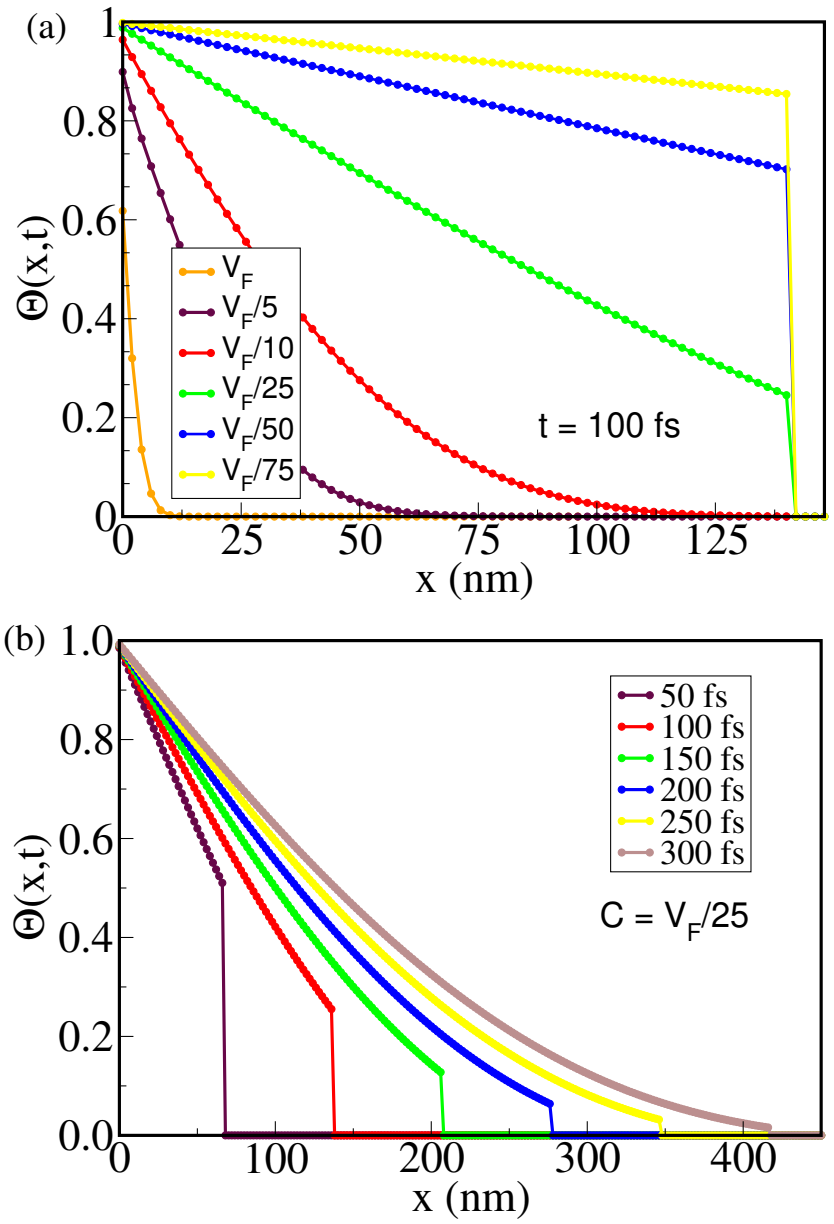

Figure 8.4: Explanation of penetration of electronic excitations farther into the crystallites than the mean free path of electrons in Au by hyperbolic wave-theory of heat transfer. Here, $\Theta(x,t) = \frac{T_{El}(x,t) - T^0_{El}}{T^I_{El} - T^0_{El}}$, where T^0_{El} is temperature of the core electrons, and T^I_{El} is temperature within the *hot* cascade, $T_0 = 0$ K and $T_C = 10^4 K$, as observed in MD simulations [6]. (a) Decay of thermal excitations at the cascade-core interface (x = 0) by varying speeds of wave-propagation C_{El}. Here, $C_{El} = v_F$, v_F being the Fermi velocity of electrons in Au. The penetration to farther depths is quite evident at values of C_{El} that are an order of magnitude lower than v_{Fermi}. (b) For $C_{El} = v_F/25$, the time-dependence (in sub-picosecond range) of $\Theta(x,t)$, which results in wave-fronts with decreasing magnitudes at $x > 0$. Non-zero height of discontinuity up to 300 nm show the penetration of electronic excitations to this depth.

that in an Au-film of thickness up to 300 nm, electronic excitation induced by femto-second lasers travel at $C_{El} \sim v_{Fermi}$ (∼1.4 x 10^8 cm/s). In the sub-surface of Au microcrystallites, however, very low D value of the *trapped* electrons within the cascade is expected to increase the time-lag τ of the heat flux across the interface, hence lowering the speed of emergent thermal-wave constituting *hot* electrons, or $C_{El} < v_{Fermi}$ (see Fig. 8.3).

Here, we first understand the evolution of electronic excitations away from the interface (at x = 0) for varying velocities of propagation of hot electronic wave, and obtain the penetration depth of thermal energy (Figure 8.4). Electronic heating at the surface due to ion-impact and electron-lattice interactions has been shown to result in local T_{El} of about 10^4-$10^5 K$ [6, 194], while the lattice away from the surface remains essentially at ambient temperatures. Here, we consider the distribution of fractional change in T_{El}, i.e. $\Theta(x,t) = \frac{T_{El}(x,t)-T^0_{El}}{T^I_{El}-T^0_{El}}$, where T^I_{El} and T^0_{El} are electronic temperatures at the interface (x = 0) and ground-state T_{El} (x >> 0) respectively: $T^I_{El} = 10^4$ K and $T^0_{El} = 0$ K. Distribution of $\Theta(r,t)$ is computed for varying speeds of heat transfer at time t = 100 fs, using the analytical solution of Equation 8.2 obtained by Baumeister [195] *et. al.* (Figure 8.4a).

To further probe the spatio-temporal nature of thermal disturbance traveling at finite speed, we obtain the spatial-range as well as the limiting time of the thermal-wave to decay in an Au crystal with $D_{Au} \sim 1.12$ cm^2/s (Figure 8.4b). While speeds $C_{El} \sim v_{Fermi}$ allow penetration depth ∼75 nm [193] in ∼100 fs, the wave decays beyond this thickness, that is, $T_{El} \sim T_L$. For lower speeds, $C_{El} \sim 5$ x 10^6 cm/s (or $v_{Fermi}/25$) for instance, the wave travels to larger depths (∼ 300 nm) within 200 fs (Figure 8.4b). These results indeed

indicate that heat transfer by *hot* electronic wave, which primarily arises from a finite time-lag τ between the onset of heat propagation and temperature gradient ∇T at the interface, allows electronic excitations to penetrate to significantly larger depths, as compared to the mean-free path of the electrons in crystalline *fcc*-Au (∼38 nm in crystalline gold at low T_L [196]) [190, 197]. Lower the speed of wave C_{El}, farther the penetration depth. Formation of its wave-front or temperature discontinuity for low C_{El} at a finite time $t > 0$ gives the magnitude of thermal disturbance *felt* at a distance x.

Additive nature of structural transformations [5], and anisotropic elastic-strain response on ion-irradiation of Au microcrystallites provide strong evidence for *wave-like* heat transfer and correlations between elastic strains of *bc(o,t)* phases at consecutive durations, and hence the applicability of hyperbolic equation of heat-flux (Equation 8.1). Enhanced homogeneity of elastic strains on irradiation over the particle dimension (∼200-250 nm) cannot be explained by Fourier-diffusion equation, $q(r,t) = -K \bigtriangledown T(r,t)$.

We now examine the nature of structural transformations that result from electronic excitations in the core of the crystallites. Prolonged ion-irradiation results in a cumulative increase in the average volume of the particle by ∼0.9% at 1030 min. Considering lattice heating due to electron-phonon and phonon-phonon interactions, with coefficient of volumetric expansion of 42 x $10^{-6}K^{-1}$, this corresponds to ΔT ∼$210K$. Since temperature of thermolysis during the synthesis of particles is ∼(200-250^{o}C), this thermal energy is inadequate to change the mole fraction of non-*fcc* phases, as has been observed on ion-irradiation of crystallites (See Fig. 8.1d). Nonetheless, the volume-expansion corresponds to an increment in electronic energy, expressed as an

increase in the width of Fermi-Dirac distribution by $\sim$ 0.54 eV (or $\Delta T_{El} \sim$ 6250 K) [198]. This indicates the dominant role of electron-electron thermalization and subsequent ion-electron interactions in time-dependent stabilization of varying elastic strains in the non-*fcc* phases upon ion irradiation.

With the particle *core* essentially at low temperatures, $T_L \sim$ 300 K, and weak *el-ph* coupling strength of Au (of the order of 2.2 x 10^{16} W/m^3/K [199], excited electrons thermalize primarily through *el-el* interactions [200]. Since Au has fully filled 4d-orbitals below E_F and an s-band at the Fermi level, its relatively low density of states (e-DoS) at E_F would result in an efficient energy transport from electrons at high T_{El} to the lattice, as reported in Cu, unlike structural disordering in Ni having high density of 3d-states at E_F [201, 202]. Thus, low-energy ion irradiation of metals and resulting structural transformations are essentially an electronic-structure-dependent process, and is significantly influenced by electronic excitations [194], and electron-phonon coupling.

Equilibrated electrons follow Fermi-Dirac (FD) quantum statistics at a low electronic temperature ($T_{El} \sim 10^3$-10^4) and high electron density (ρ_E) of a material. Since the longitudinal dimension of the crystallites is $\sim 10^{-3}$ cm (>> a $\sim$4 $\mathring{A}$), across which energy-transfer from electronic subsystem to the lattice occurs, it is justified to consider the non-*fcc* phase within the core of the particle as a periodic crystal to study the evolution of non-*fcc* phases with ion-irradiation. To understand the variations in elastic strains with electronic temperature, we carried-out structural-optimization of *bc(o,t)* structures with varied width of FD-distribution.

In the *fcc* structure, (111) plane subtends an angle $\delta = 54.74^o$ with

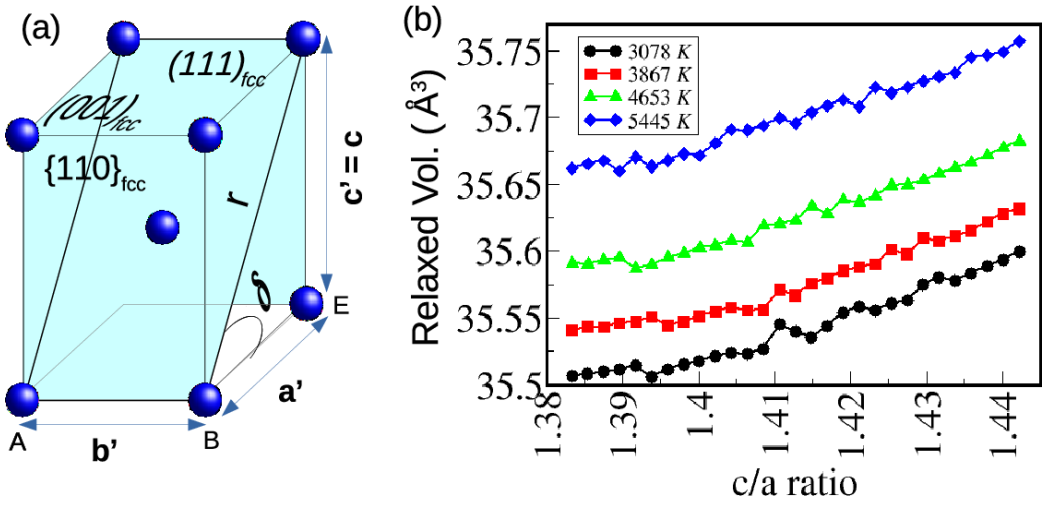

Figure 8.5: (a) Schematic of *bct* cell used in the simulations, and (b) volumes of relaxed configurations for a fixed T_{El} and across varying T_{El} values.

(001) plane. Geometrically, *bc(o,t)* phases indexed in the experiments have the following relations with *fcc* Au: $(001)_{fcc} = (001)_{bc(o,t)}$ and $(111)_{fcc} = (110)_{bc(t,o)}$ [183]. Also, $c_{fcc} = c_{bc(t,o)}$ and $a_{fcc}/\sqrt{2} = a'_{bct}$. Since the non-*fcc* metastable structures vary only in the length of cell-vectors with ion-irradiation, while maintaining their orthogonality, it signifies that δ is a free-parameter which allows corresponding changes in a' and c, while leaving the angles $\alpha, \beta, \gamma = 90^o$ (Figure 8.5a). Therefore, starting with variable cell-optimized *bct*-form of *fcc* Au ($a' = b' = 2.927$ $\AA$ and $c = 4.139$ $\AA$; c/a = $\sqrt{2}$), the angle δ (between $(101)_{bct}$ and $(001)_{bct}$) was changed from 53^o-56^o in the interval of 0.125^o, and a' and c ($a' = r\ \cos(\delta)$, $c = r\ \sin(\delta)$) values were obtained (see Figure 8.5a), to keep b' constant. This gives a general *bco* structure as the starting configuration (with unequal strains along the crystal axes). All the experimentally obtained c values with varying duration of ion-irradiation fall well within the c values corresponding to δ in 53^o - 56^o.

An unconstrained relaxation of these configurations invariably results in

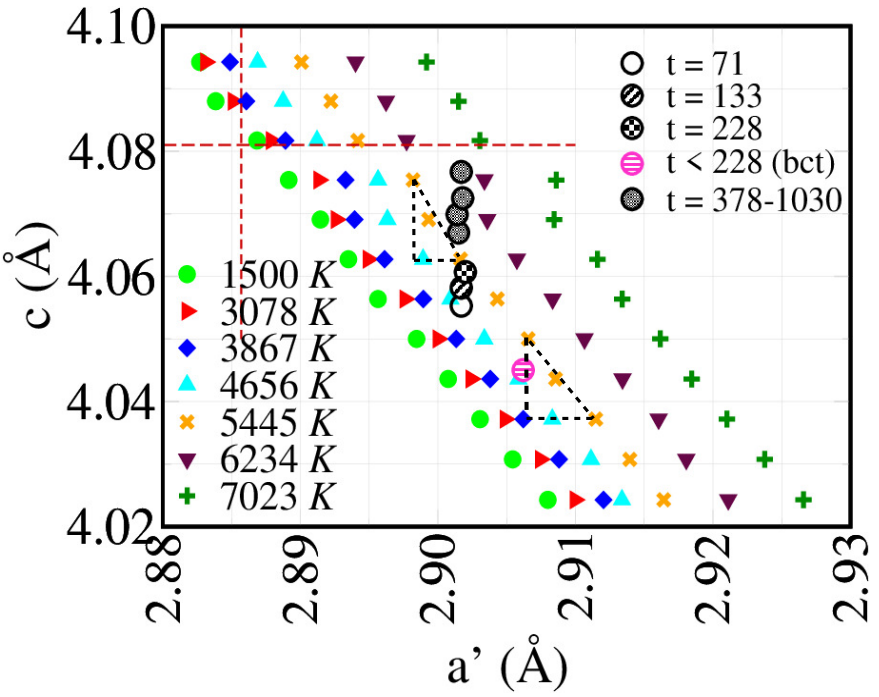

Figure 8.6: Lattice parameters of the minimum-energy structures obtained on constrained-optimization of *bco* phase with varying electronic temperatures. To superimpose the bc(o,t) structures obtained with an increase in irradiation time t (Figure 8.1d) to the cells relaxed with increase in T_{El}, we scale the cell-dimensions a, b and c with the observed lattice constant (a = 4.081 $\AA$). The dashed red lines show dimensions of bulk *fcc* Au. The two triangular regions with dashed lines show that as c/a$'$ increases, the changes in a' (and b') become smaller, for a fixed change in c-parameter.

stabilization of *fcc* structure ($c/a' = \sqrt{2}$) in each case. This confirms the kinetic, and not thermodynamic origin of the non-*fcc* phases in Au microcrystallites [183]. Hence, we performed constrained energy-optimization for a range of electronic temperatures T_{El} by fixing the c values of derived configurations, and variable a' and b' until the stress components (σ_{aa} and σ_{bb}) reduce to ∼0 GPa. At a particular T_{El}, energies of all the strained structures considered show very small variation (within ± 5 meV/atom). This primarily stems from small changes in volume at a fixed T_{El} (Figure 8.5b), that is, as the c-parameter increases towards $\sqrt{2}$, the a' (and b') values tend toward 1 (as shown by the arrow in Figure 8.6).

With increase in electronic excitations, the volume of a phase is bound to increase. However, the a' and c of optimized parameters show that as $c_{bc(o,t)} \rightarrow c_{fcc}$ (horizontal red dashed line), variation in a' (and b') becomes significantly smaller than that in c (shown by comparison of two dashed triangles for $T_{El} = 5445\ K$). This indicates a rather unimpeded structural change along c-direction, in response to electronic excitations, while constrained variations in the $a'b'$ plane of *bct*-Au. Interestingly, the computed minimum-energy structures at different T_{El} show good agreement with the *bct-I* structures observed in XRD-powder patterns, confirming the pertinence of elevated electronic temperature in varying c/a' ratio with ion irradiation-dosage.

Since changes in a' (and b') are significantly slower than that in c with T_{El}, in agreement with *bct*-I structures, we gather the c-values at each T_{El} that fall within the range of a' of indexed structures (in {1.0054-1.0055}). The resulting c-values are then fitted against T_{El} (see Fig. 8.7). T_{El} has a

quadratic dependence on c as:

$$T_{El} = a_0 + a_1 c + a_2 c^2 \tag{8.3}$$

The c-values corresponding to *bct*-I observed with prolonged irradiation time t (in min) also show a quadratic dependence as:

$$c = b_0 + b_1 t + b_2 t^2 \tag{8.4}$$

$a_i's$ and $b_i's$ are tabulated in Table 8.1. Thus, T_{El} has a higher-order dependence on t, given as:

$$T_{El} = (a_0+a_1b_0+a_2b_0^2)+(a_1b_1+2a_2b_0b_1)t+(a_1b_2+a_2b_1^2+2a_2b_0b_2)t2+2a_2b_1b_2t^3+a_2b_2^2t^4 \tag{8.5}$$

As the coefficient b_2 is very small, fourth-order term in t can be ignored (See Table 8.1). The curve T_{El} versus t shows a rather rapid growth of T_{El} at short times, leading to its saturation at prolonged durations of ion-irradiation. With high-rate of sputtering on ion-irradiation and concomitant reduction in the lateral thickness of the crystallites, the height of wave-front of thermal electronic wave will continuously increase (Figure 8.4a), resulting in higher values of T_{El} at large t. This further corroborates the *wave-like* transfer of electronic energy into the core Au microcrystallites upon ion-irradiation.

In conclusion, we have presented a non-Fourier mechanism of heat transfer by electrons on ion-irradiation of Au microcrystallites, with its genesis in

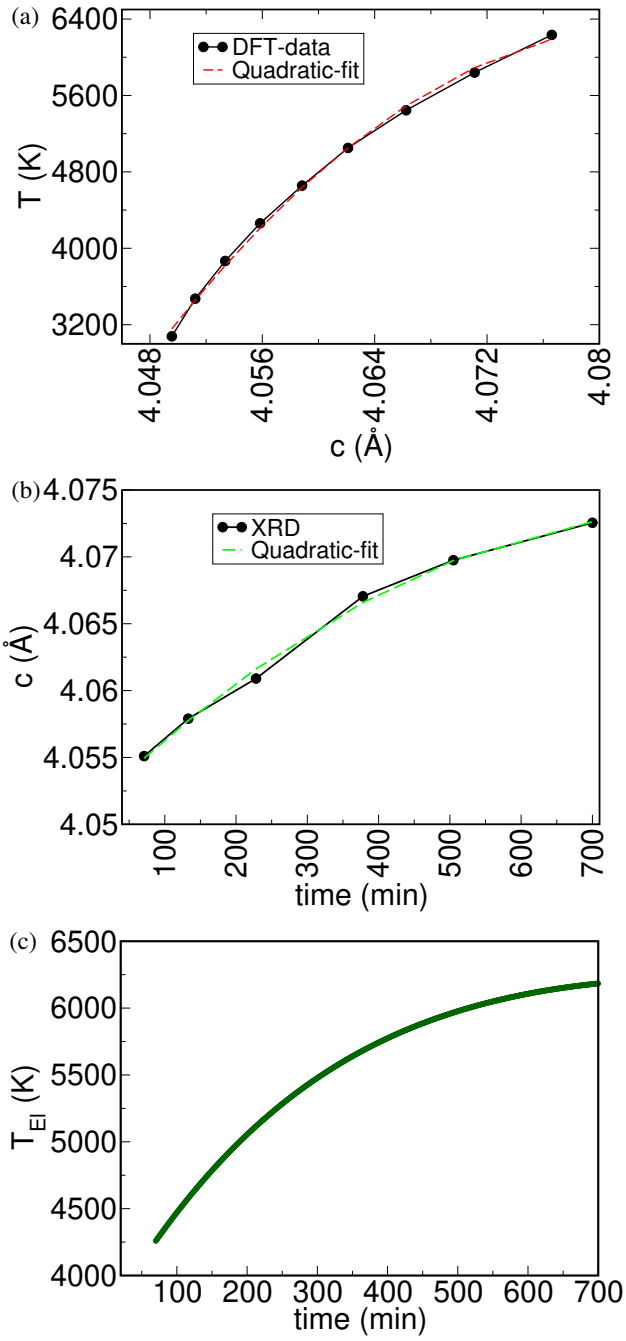

Figure 8.7: Empirical relation between irradiation-time t and electronic temperature T_{El} within the core of Au microcrystallites: (a) Dependence of c-parameter on T_{El}, (b) Dependence of c-parameter on irradiation time, and (c) relationship between T_{El} and t. T_{El} increases steeply at low-dosage but saturates on prolonged irradiation.

Table 8.1: Coefficients of terms relevant to time-temperature relationship

a_0	-4.48e^{+7} K
a_1	2.20e^{+7} $K/\mathring{A}$
a_2	-2.69e^{+6} $K/\mathring{A}^2$
b_0	4.051 $\mathring{A}$
b_1	5.16e^{-5} $\mathring{A}/min$
b_2	-3.05e^{-8} $\mathring{A}/min^2$

the transient thermodynamic state at the cascade-core interface that manifests as a time-lag between heat flux ($\mathbf{q}$) and temperature-gradient (∇). We demonstrate that the *thermal wave* of electrons traveling at a speed about an order of magnitude lower than the Fermi velocity of Au can propagate undeterred to ∼200-250 nm into the particle within ∼ 100 fs, a distance significantly larger than the mean-free path of electrons (∼ 40 nm) in Au. Emergent *hot* excited electrons in the *core* of the microcrystallites tune the elastic strains of non-*fcc* phases, with significant changes along the [001] direction, as obtained by optimization of strained *bc(o,t)* structures at varying widths of Fermi-Dirac distribution of electrons. The computed structures show a good agreement with the bct-I structures obtained by indexing the XRD powder-diffraction patterns.

Chapter 9

Summary and future directions

In this thesis, we have presented a quantitative measure of mechanical flexibility $\bar{F}^s \in [0,1]$ of a crystalline solid and demonstrated that flexibility results in reduction of elastic rigidity of a crystal associated with its Nambu-Goldstone bosons (acoustic phonons) through their coupling with *continuous* internal structural degrees of freedom. The concept is outlined in Figure 9.1.

Through phonon-spectral analysis, we understand the mechanisms of crystal-to-amorphous transition, and origin of Boson Peak(s) in two chemically and topologically distinct metal organic frameworks, *porous* crystalline

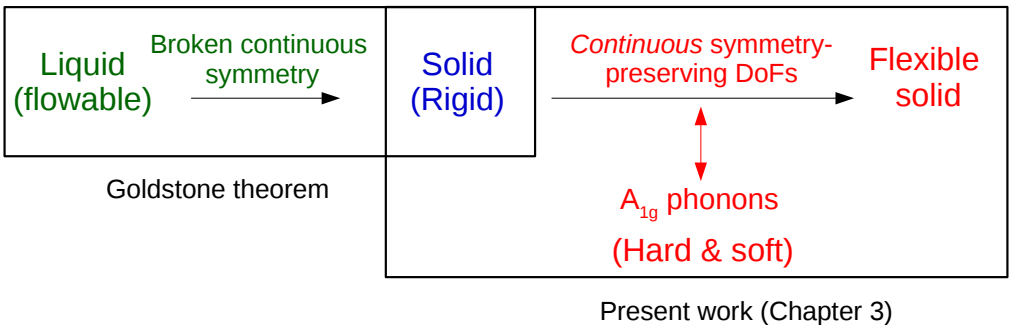

Figure 9.1: Origin of the structural flexibility of a crystal.

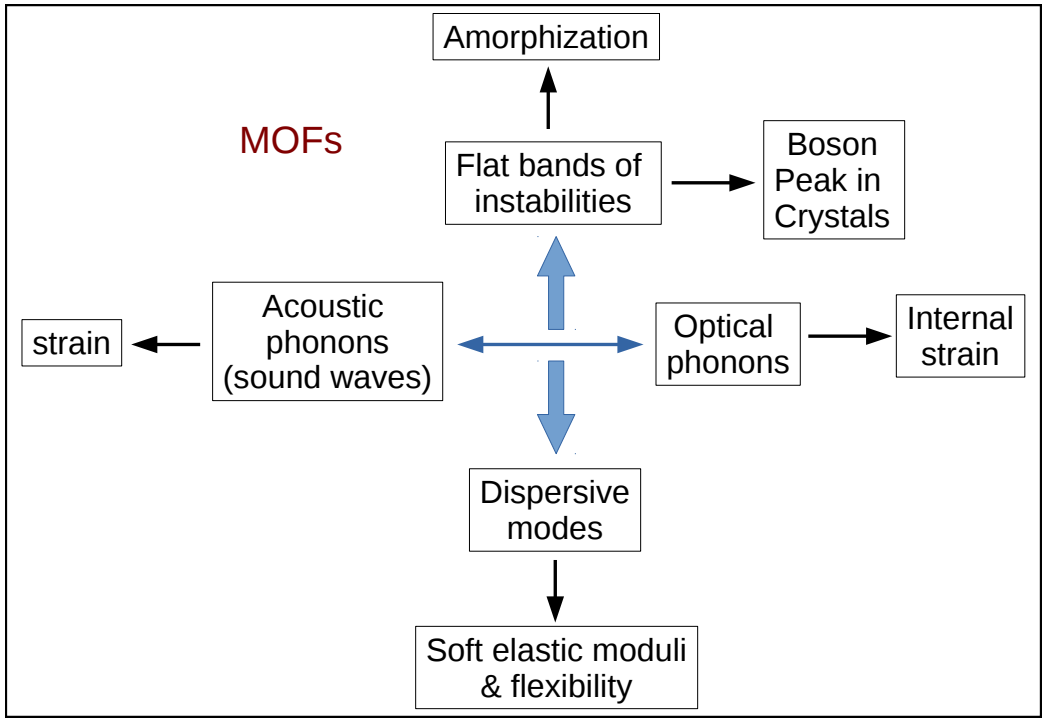

Figure 9.2: A picture of Flexibility, Amorphization and Boson Peak in crystalline materials in terms of interacting phonons.

materials, MOF-5 and ZIF-8. Fundamentally, the three phenomena, (a) flexibility, (b) amorphization, and (c) Boson Peak share a common feature in the *coupling* between long-wavelength acoustic phonons (homogeneous strains) and optical phonons. Distinct character of optical modes responsible for these emergent phenonomena can be seen in Figure 9.2.

In Part B, we have presented a *soft* phonon-based analysis of stability of non-*fcc* phases in Au microcrystallites with a penta-twinned geometry. We further uncovered the fundamental differences between the mechanisms of heat-transfer through annealing and prolonged ion-irradiation in terms of distribution of strains along the thickness of the microcrystallite. We have

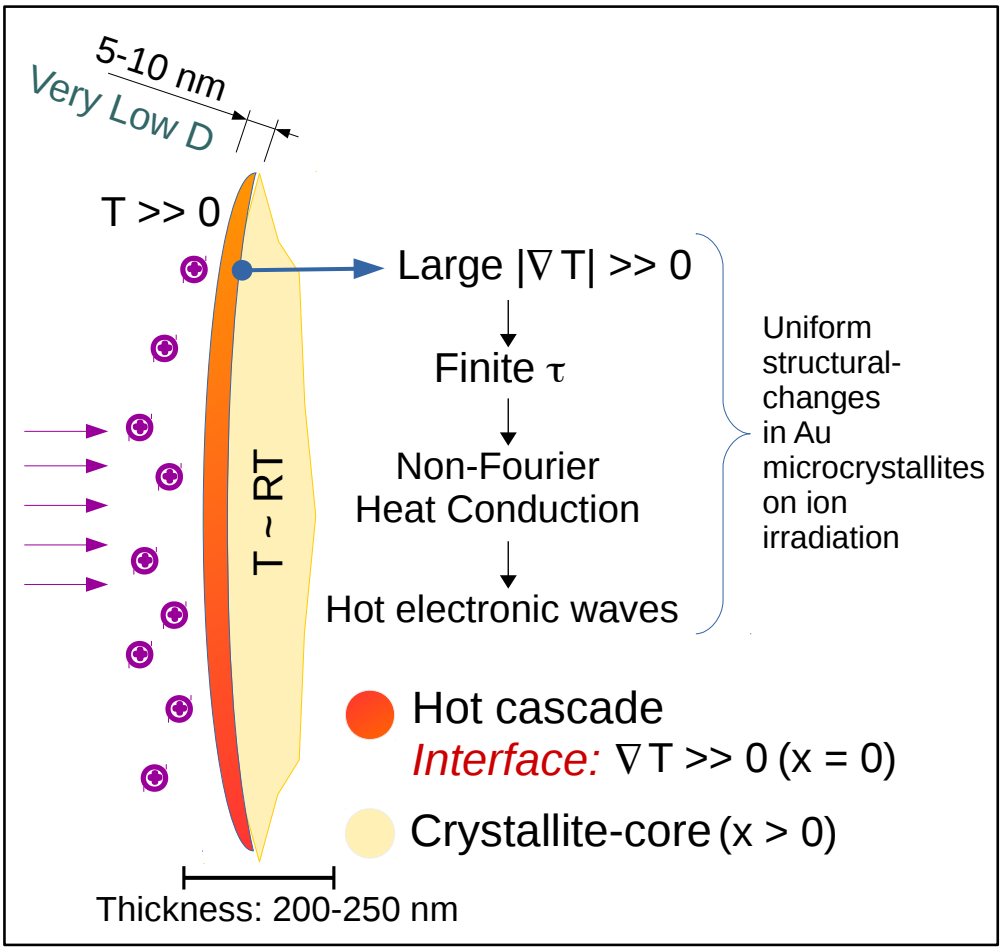

Figure 9.3: *Non-Fourier* mode of heat conduction in a metal-microcrystallite upon ion-irradiation.

presented a plausible mechanism of *non-Fourier* heat conduction by electrons in ion-irradiated Au microcrystallites which is responsible for a rather atypical narrowing of XRD-peaks on prolonged exposures to low-energy Ar^+ irradiation. The mechanism is outlined in Figure 9.3:

On the basis of ideas developed in this thesis, it would be interesting to explore:

- General "flexibility" measure; LR order, for example, chemical, electrical, magnetic etc.
- Crystal-to-amorphous transitions in other complex crystals that exhibit inherent *non-linear* elasticity.
- Crystals other than MOFs that show a Boson Peak in $C(T)/T^3$ at low-T.
- Pressure-induced changes in Boson Peak(s) of crystalline materials.

Bibliography

[1] H. Li, M. Eddaoudi, M. O'Keeffe, and O. M. Yaghi, "Design and synthesis of an exceptionally stable and highly porous metal-organic framework," *Nature*, vol. 402, pp. 276–279, 1999.

[2] D. J. Tranchemontagne, J. R. Hunt, and O. M. Yaghi, "Room temperature synthesis of metal-organic frameworks: Mof-5, mof-74, mof-177, mof-199, and irmof-0," *Tetrahedron*, vol. 64, pp. 8553 – 8557, 2008.

[3] M. Erkartal and M. Durandurdu, "Pressure-induced amorphization of mof-5: A first principles study," *ChemistrySelect*, vol. 3, pp. 8056–8063, 2018.

[4] Y. Hinuma, G. Pizzi, Y. Kumagai, F. Oba, and I. Tanaka, "Band structure diagram paths based on crystallography," *Computational Materials Science*, vol. 128, pp. 140–184, 2017.

[5] C. Sow, "Penta-twinned bipyramidal au microcrystallites: Unraveling non-cubic phases and investigating phase transformations," *Ph.D. Thesis, JNCASR, Bangalore*, 2020.

[6] A. Duvenbeck, Z. Sroubek, and A. Wucher, "Electronic excitation in atomic collision cascades," *Nuclear Instruments and Methods in Physics Research Section B: Beam Interactions with Materials and Atoms*, vol. 228, pp. 325 – 329, 2005.

[7] A. E. H. Love, "The Propagation of Wave-Motion in an Isotropic Elastic Solid Medium," *Proceedings of the London Mathematical Society*, vol. s2-1, pp. 291–344, 1904.

[8] E. Lewis, "The pressure of sound waves," *Science*, vol. 43, pp. 646–648, 1916.

[9] D. Bourgin, "Xcvii. the propagation of sound in gases," *The London, Edinburgh, and Dublin Philosophical Magazine and Journal of Science*, vol. 7, pp. 821–841, 1929.

[10] C. Morris, "The matter of space," *Nature*, vol. 28, pp. 148–150, 1883.

[11] C. Kittel, P. McEuen, and P. McEuen, *Introduction to solid state physics*, vol. 8. Wiley New York, 1996.

[12] C. Raman and C. Venkateswaran, "Rigidity of liquids," *Nature*, vol. 143, pp. 798–799, 1939.

[13] R. Bosworth, "An interpretation of the viscosity of liquids," *Transactions of the Faraday Society*, vol. 44, pp. 308–317, 1948.

[14] J. Goldstone, A. Salam, and S. Weinberg, "Broken symmetries," *Physical Review*, vol. 127, p. 965, 1962.

[15] H. Watanabe and H. Murayama, "Unified description of nambu-goldstone bosons without lorentz invariance," *Physical review letters*, vol. 108, p. 251602, 2012.

[16] C. Kittel, "Ultrasonics research and the properties of matter," *Reports on Progress in Physics*, vol. 11, p. 205, 1947.

[17] W. Fateley, N. T. McDevitt, and F. F. Bentley, "Infrared and raman selection rules for lattice vibrations: the correlation method," *Applied Spectroscopy*, vol. 25, pp. 155–173, 1971.

[18] S. J. Gardiner, *Harmonic approximation*, vol. 221. Cambridge university press, 1995.

[19] C. Hammond and C. Hammond, *The basics of cristallography and diffraction*, vol. 214. Oxford, 2001.

[20] J. R. Barber, *Elasticity*. Springer, 2002.

[21] L. Van Hove, "The occurrence of singularities in the elastic frequency distribution of a crystal," *Physical Review*, vol. 89, p. 1189, 1953.

[22] A. Bruce, R. A. Cowley, B. Dorner, A. Muller, H. Thomas, and T. in Current Physics; 23, *Structural phase transitions*, vol. 29. Taylor & Francis London, 1981.

[23] P. Ghosez, E. Cockayne, U. Waghmare, and K. Rabe, "Lattice dynamics of batio$_3$, pbtio$_3$, and pbzro$_3$: A comparative first-principles study," *Physical Review B*, vol. 60, p. 836, 1999.

[24] L. Morellon, P. Algarabel, M. Ibarra, J. Blasco, B. Garcia-Landa, Z. Arnold, and F. Albertini, "Magnetic-field-induced structural phase transition in gd5(si1.8ge2.2)," *Physical Review B*, vol. 58, p. R14721, 1998.

[25] T. Chattopadhyay, J. Boucherle, *et al.*, "Neutron diffraction study on the structural phase transition in gete," *Journal of Physics C: Solid State Physics*, vol. 20, p. 1431, 1987.

[26] K. Umemoto and R. M. Wentzcovitch, "Potential ultrahigh pressure polymorphs of ab x 3-type compounds," *Physical Review B*, vol. 74, p. 224105, 2006.

[27] D. M. Hanson, "Direct observation of a soft phonon associated with a structural phase transition in a molecular crystal," *The Journal of Chemical Physics*, vol. 63, pp. 5046–5047, 1975.

[28] H.-J. Lee, M. Lee, K. Lee, J. Jo, H. Yang, Y. Kim, S. C. Chae, U. Waghmare, and J. H. Lee, "Scale-free ferroelectricity induced by flat phonon bands in hfo2," *Science*, vol. 369, pp. 1343–1347, 2020.

[29] W. R. Mondal, N. S. Vidhyadhiraja, T. Berlijn, J. Moreno, and M. Jarrell, "Localization of phonons in mass-disordered alloys: A typical medium dynamical cluster approach," *Phys. Rev. B*, vol. 96, p. 014203, 2017.

[30] S. L. James, "Metal-organic frameworks," *Chemical Society Reviews*, vol. 32, pp. 276–288, 2003.

[31] A. K. Cheetham and C. Rao, "There's room in the middle," *Science*, vol. 318, no. 5847, pp. 58–59, 2007.

[32] H. Furukawa, N. Ko, Y. B. Go, N. Aratani, S. B. Choi, E. Choi, A. Ö. Yazaydin, R. Q. Snurr, M. OKeeffe, J. Kim, *et al.*, "Ultrahigh porosity in metal-organic frameworks," *Science*, vol. 329, pp. 424–428, 2010.

[33] O. M. Yaghi, M. O'Keeffe, N. W. Ockwig, H. K. Chae, M. Eddaoudi, and J. Kim, "Reticular synthesis and the design of new materials," *Nature*, vol. 423, pp. 705–714, 2003.

[34] D. J. Tranchemontagne, J. L. Mendoza-Cortés, M. OKeeffe, and O. M. Yaghi, "Secondary building units, nets and bonding in the chemistry of metal–organic frameworks," *Chemical Society Reviews*, vol. 38, pp. 1257–1283, 2009.

[35] L. J. Murray, M. Dincă, and J. R. Long, "Hydrogen storage in metal–organic frameworks," *Chemical Society Reviews*, vol. 38, pp. 1294–1314, 2009.

[36] R.-B. Lin, S. Xiang, H. Xing, W. Zhou, and B. Chen, "Exploration of porous metal–organic frameworks for gas separation and purification," *Coordination Chemistry Reviews*, vol. 378, pp. 87–103, 2019.

[37] L. Zhu, X.-Q. Liu, H.-L. Jiang, and L.-B. Sun, "Metal–organic frameworks for heterogeneous basic catalysis," *Chemical reviews*, vol. 117, no. 12, pp. 8129–8176, 2017.

[38] M. Yoon, K. Suh, S. Natarajan, and K. Kim, "Proton conduction in metal–organic frameworks and related modularly built porous solids," *Angewandte Chemie International Edition*, vol. 52, pp. 2688–2700, 2013.

[39] I. A. Lazaro and R. S. Forgan, "Application of zirconium mofs in drug delivery and biomedicine," *Coordination Chemistry Reviews*, vol. 380, pp. 230–259, 2019.

[40] D. Dubbeldam, K. S. Walton, D. E. Ellis, and R. Q. Snurr, "Exceptional negative thermal expansion in isoreticular metal–organic frameworks," *Angewandte Chemie*, vol. 119, no. 24, pp. 4580–4583, 2007.

[41] C. M. Simon, E. Braun, C. Carraro, and B. Smit, "Statistical mechanical model of gas adsorption in porous crystals with dynamic moieties," *Proceedings of the National Academy of Sciences*, vol. 114, no. 3, pp. E287–E296, 2017.

[42] T. A. Mary, J. S. O. Evans, T. Vogt, and A. W. Sleight, "Negative Thermal Expansion from 0.3 to 1050 Kelvin in ZrW_2O_8," *Science*, vol. 272, pp. 90–92, 1996.

[43] J. S. Evans, W. David, and A. Sleight, "Structural investigation of the negative-thermal-expansion material zrw2o8," *Acta Crystallographica Section B: Structural Science*, vol. 55, no. 3, pp. 333–340, 1999.

[44] A. Schneemann, V. Bon, I. Schwedler, I. Senkovska, S. Kaskel, and R. A. Fischer, "Flexible metal-organic frameworks," *Chem. Soc. Rev.*, vol. 43, pp. 6062–6096, 2014.

[45] Z. Chang, D.-H. Yang, J. Xu, T.-L. Hu, and X.-H. Bu, "Flexible metal–organic frameworks: recent advances and potential applications," *Advanced Materials*, vol. 27, no. 36, pp. 5432–5441, 2015.

[46] S. K. Elsaidi, M. H. Mohamed, D. Banerjee, and P. K. Thallapally, "Flexibility in metalorganic frameworks: A fundamental understanding," *Coordination Chemistry Reviews*, vol. 358, pp. 125 – 152, 2018.

[47] L. Sarkisov, R. L. Martin, M. Haranczyk, and B. Smit, "On the flexibility of metal–organic frameworks," *Journal of the American Chemical Society*, vol. 136, no. 6, pp. 2228–2231, 2014.

[48] Y. H. Hu and L. Zhang, "Amorphization of metal-organic framework mof-5 at unusually low applied pressure," *Phys. Rev. B*, vol. 81, p. 174103, 2010.

[49] K. S. Park, Z. Ni, A. P. Côté, J. Y. Choi, R. Huang, F. J. Uribe-Romo, H. K. Chae, M. OKeeffe, and O. M. Yaghi, "Exceptional chemical and thermal stability of zeolitic imidazolate frameworks," *Proceedings of the National Academy of Sciences*, vol. 103, pp. 10186–10191, 2006.

[50] S. Cao, T. D. Bennett, D. A. Keen, A. L. Goodwin, and A. K. Cheetham, "Amorphization of the prototypical zeolitic imidazolate framework zif-8 by ball-milling," *Chemical Communications*, vol. 48, pp. 7805–7807, 2012.

[51] K. W. Chapman, G. J. Halder, and P. J. Chupas, "Pressure-induced amorphization and porosity modification in a metal- organic framework," *Journal of the American Chemical Society*, vol. 131, pp. 17546–17547, 2009.

[52] J.-C. Tan, B. Civalleri, C.-C. Lin, L. Valenzano, R. Galvelis, P.-F. Chen, T. D. Bennett, C. Mellot-Draznieks, C. M. Zicovich-Wilson, and A. K. Cheetham, "Exceptionally low shear modulus in a prototypical imidazole-based metal-organic framework," *Phys. Rev. Lett.*, vol. 108, p. 095502, 2012.

[53] A. U. Ortiz, A. Boutin, A. H. Fuchs, and F.-X. Coudert, "Investigating the pressure-induced amorphization of zeolitic imidazolate framework zif-8: mechanical instability due to shear mode softening," *The journal of physical chemistry letters*, vol. 4, pp. 1861–1865, 2013.

[54] T. D. Bennett, P. J. Saines, D. A. Keen, J.-C. Tan, and A. K. Cheetham, "Ball-milling-induced amorphization of zeolitic imidazolate

frameworks (zifs) for the irreversible trapping of iodine," *Chemistry–A European Journal*, vol. 19, pp. 7049–7055, 2013.

[55] K. W. Chapman, D. F. Sava, G. J. Halder, P. J. Chupas, and T. M. Nenoff, "Trapping guests within a nanoporous metal–organic framework through pressure-induced amorphization," *Journal of the American Chemical Society*, vol. 133, pp. 18583–18585, 2011.

[56] S. H. Park and S. J. Lee, "Versatile amorphous structures of phosphonate metal- organic framework/alginate composite for tunable sieving of ions," *Advanced Functional Materials*, vol. 29, p. 1904016, 2019.

[57] F. Yang, W. Li, and B. Tang, "Facile synthesis of amorphous uio-66 (zr-mof) for supercapacitor application," *Journal of Alloys and Compounds*, vol. 733, pp. 8–14, 2018.

[58] A. I. Chumakov, G. Monaco, A. Monaco, W. A. Crichton, A. Bosak, R. Rüffer, A. Meyer, F. Kargl, L. Comez, D. Fioretto, H. Giefers, S. Roitsch, G. Wortmann, M. H. Manghnani, A. Hushur, Q. Williams, J. Balogh, K. Parliński, P. Jochym, and P. Piekarz, "Equivalence of the Boson peak in glasses to the transverse acoustic van Hove singularity in crystals," *Phys. Rev. Lett.*, vol. 106, p. 225501, 2011.

[59] A. I. Chumakov, G. Monaco, X. Han, L. Xi, A. Bosak, L. Paolasini, D. Chernyshov, and V. Dyadkin, "Relation between the boson peak in glasses and van hove singularity in crystals," *Philosophical Magazine*, vol. 96, pp. 743–753, 2016.

[60] G. Mettela, M. Bhogra, U. V. Waghmare, and G. U. Kulkarni, "Ambient stable tetragonal and orthorhombic phases in penta-twinned bipyramidal au microcrystals," *Journal of the American Chemical Society*, vol. 137, pp. 3024–3030, 2015.

[61] M. O¨ zis¸ik and D. Tzou, "On the wave theory in heat conduction," *J. Heat Transfer*, vol. 116, pp. 526–535, 1994.

[62] R. M. Martin. Cambridge University Press, 2004.

[63] P. Koskinen and V. Mäkinen, "Density-functional tight-binding for beginners," *Computational Materials Science*, vol. 47, pp. 237–253, 2009.

[64] F. Spiegelman, N. Tarrat, J. Cuny, L. Dontot, E. Posenitskiy, C. Martí, A. Simon, and M. Rapacioli, "Density-functional tight-binding: basic concepts and applications to molecules and clusters," *Advances in Physics: X*, vol. 5, p. 1710252, 2020.

[65] M. Elstner, D. Porezag, G. Jungnickel, J. Elsner, M. Haugk, T. Frauenheim, S. Suhai, and G. Seifert, "Self-consistent-charge density-functional tight-binding method for simulations of complex materials properties," *Phys. Rev. B*, vol. 58, pp. 7260–7268, 1998.

[66] T. Frauenheim, G. Seifert, M. Elstner, T. Niehaus, C. Köhler, M. Amkreutz, M. Sternberg, Z. Hajnal, A. Di Carlo, and S. Suhai, "Atomistic simulations of complex materials: ground-state and excited-state properties," *Journal of Physics: Condensed Matter*, vol. 14, p. 3015, 2002.

[67] J. C. Slater and G. F. Koster, "Simplified lcao method for the periodic potential problem," *Phys. Rev.*, vol. 94, pp. 1498–1524, 1954.

[68] K. Teilum, J. G. Olsen, and B. B. Kragelund, "Protein stability, flexibility and function," *Biochimica et Biophysica Acta (BBA)-Proteins and Proteomics*, vol. 1814, pp. 969–976, 2011.

[69] B. Schulze, A. Sljoka, and W. Whiteley, "How does symmetry impact the flexibility of proteins?," *Philosophical Transactions of the Royal Society A: Mathematical, Physical and Engineering Sciences*, vol. 372, p. 20120041, 2014.

[70] J. Janin and M. J. Sternberg, "Protein flexibility, not disorder, is intrinsic to molecular recognition," *F1000 biology reports*, vol. 5, 2013.

[71] A. Sartbaeva, S. A. Wells, M. M. J. Treacy, and M. F. Thorpe, "The flexibility window in zeolites," *Nature Materials*, vol. 5, pp. 962–965, 2006.

[72] S. A. Wells and A. Sartbaeva, "Gasp: software for geometric simulations of flexibility in polyhedral and molecular framework structures," *Molecular Simulation*, vol. 41, pp. 1409–1421, 2015.

[73] M. T. Dove, "Flexibility of network materials and the rigid unit mode model: a personal perspective," *Philosophical Transactions of the Royal Society A*, vol. 377, p. 20180222, 2019.

[74] M. T. Wharmby, S. Henke, T. D. Bennett, S. R. Bajpe, I. Schwedler, S. P. Thompson, F. Gozzo, P. Simoncic, C. Mellot-Draznieks, H. Tao, *et al.*, "Extreme flexibility in a zeolitic imidazolate framework: Porous to dense phase transition in desolvated zif-4," *Angewandte Chemie*, vol. 127, pp. 6547–6551, 2015.

[75] T. D. Bennett, A. K. Cheetham, A. H. Fuchs, and F.-X. Coudert, "Interplay between defects, disorder and flexibility in metal–organic frameworks," *Nature Chemistry*, vol. 9, pp. 11–16, 2016.

[76] L. Bocquet, A. Colin, and A. Ajdari, "Kinetic theory of plastic flow in soft glassy materials," *Physical review letters*, vol. 103, p. 036001, 2009.

[77] A. Widmer-Cooper, H. Perry, P. Harrowell, and D. R. Reichman, "Irreversible reorganization in a supercooled liquid originates from localized soft modes," *Nature Physics*, vol. 4, pp. 711–715, 2008.

[78] C. P. Goodrich, A. J. Liu, and S. R. Nagel, "Solids between the mechanical extremes of order and disorder," *Nature Physics*, vol. 10, pp. 578–581, 2014.

[79] A. Marmier and K. E. Evans, "Flexibility in mofs: do scalar and group-theoretical counting rules work?," *Dalton Transactions*, vol. 45, pp. 4360–4369, 2016.

[80] C. V. Raman, K. S. Viswanathan, and D. Krishnamurti, "The elasticity of crystals," *Current Science*, vol. 24, pp. 325–328, 1955.

[81] A. U. Ortiz, A. Boutin, A. H. Fuchs, and F. m. c.-X. Coudert, "Anisotropic elastic properties of flexible metal-organic frameworks: How soft are soft porous crystals?," *Phys. Rev. Lett.*, vol. 109, p. 195502, 2012.

[82] D. Fairen-Jimenez, S. Moggach, M. Wharmby, P. Wright, S. Parsons, and T. Duren, "Opening the gate: framework flexibility in zif-8 explored by experiments and simulations," *Journal of the American Chemical Society*, vol. 133, pp. 8900–8902, 2011.

[83] J. Eckert, "High energy phonons: overview," 1984.

[84] S. Natarajan and P. Mahata, "Metalorganic framework structures how closely are they related to classical inorganic structures?," *Chem. Soc. Rev.*, vol. 38, pp. 2304–2318, 2009.

[85] O. M. Yaghi, M. O'Keeffe, N. W. Ockwig, H. K. Chae, M. Eddaoudi, and J. Kim, "Reticular synthesis and the design of new materials," *Nature*, vol. 423, pp. 705–714, 2003.

[86] D. Dubbeldam, K. Walton, D. Ellis, and S. Q. Randall, "Exceptional Negative Thermal Expansion in Isoreticular Metal–Organic Frameworks," *Angewandte Chemie International Edition*, vol. 46, pp. 4496–4499, 2007.

[87] C. M. Simon, E. Braun, C. Carraro, and B. Smit, "Statistical mechanical model of gas adsorption in porous crystals with dynamic moieties," *Proceedings of the National Academy of Sciences*, vol. 114, pp. 287–296, 2017.

[88] A. K. Cheetham, G. Kieslich, and H. H.-M. Yeung, "Thermodynamic and Kinetic Effects in the Crystallization of Metal–Organic Frameworks," *Accounts of Chemical Research*, vol. 51, pp. 659–667, 2018.

[89] M. R. Ryder, B. Civalleri, T. D. Bennett, S. Henke, S. Rudić, G. Cinque, F. Fernandez-Alonso, and J.-C. Tan, "Identifying the Role

of Terahertz Vibrations in Metal–Organic Frameworks: From Gate–Opening Phenomenon to Shear–Driven Structural Destabilization," *Phys. Rev. Lett.*, vol. 113, pp. 215502–215507, 2014.

[90] J. C. Tan and A. K. Cheetham, "Mechanical properties of hybrid inorganicorganic framework materials: establishing fundamental structureproperty relationships," *Chem. Soc. Rev.*, vol. 40, pp. 1059–1080, 2011.

[91] I. E. Collings and A. L. Goodwin, "Metal–organic frameworks under pressure," *Journal of Applied Physics*, vol. 126, p. 181101, 2019.

[92] T. D. Bennett, P. Simoncic, S. A. Moggach, F. Gozzo, P. Macchi, D. A. Keen, J.-C. Tan, and A. K. Cheetham, "Reversible pressure-induced amorphization of a zeolitic imidazolate framework (zif-4)," *Chem. Commun.*, vol. 47, pp. 7983–7985, 2011.

[93] S. Cao, T. D. Bennett, D. A. Keen, A. L. Goodwin, and A. K. Cheetham, "Amorphization of the prototypical zeolitic imidazolate framework zif-8 by ball-milling," *Chem. Commun.*, vol. 48, pp. 7805–7807, 2012.

[94] Z. Su, Y.-R. Miao, G. Zhang, J. T. Miller, and K. S. Suslick, "Bond breakage under pressure in a metal organic framework," *Chem. Sci.*, vol. 8, pp. 8004–8011, 2017.

[95] Y. Zhou and C.-j. Liu, "Amorphization of metal–organic framework mof-5 by electrical discharge," *Plasma Chemistry and Plasma Processing*, vol. 31, pp. 499–506, 2011.

[96] M. H. Cohen, J. iguez, and J. B. Neaton, "Flat branches and pressure amorphization," *Journal of Non-Crystalline Solids*, vol. 307-310, pp. 602 – 612, 2002.

[97] H.-J. Lee, M. Lee, K. Lee, J. Jo, H. Yang, Y. Kim, S. C. Chae, U. Waghmare, and J. H. Lee, "Scale-free ferroelectricity induced by flat phonon bands in hfo2," *Science*, vol. 369, pp. 1343–1347, 2020.

[98] G. Kresse and J. Furthmüller, "Efficient iterative schemes for ab initio total-energy calculations using a plane-wave basis set," *Physical review B*, vol. 54, p. 11169, 1996.

[99] D. Vanderbilt, "Soft self-consistent pseudopotentials in a generalized eigenvalue formalism," *Physical review B*, vol. 41, p. 7892, 1990.

[100] J. P. Perdew, K. Burke, and M. Ernzerhof, "Generalized gradient approximation made simple," *Physical review letters*, vol. 77, p. 3865, 1996.

[101] A. Togo and I. Tanaka, "First principles phonon calculations in materials science," *Scr. Mater.*, vol. 108, pp. 1–5, 2015.

[102] B. Aradi, B. Hourahine, and T. Frauenheim, "DFTB+, a Sparse Matrix-Based Implementation of the DFTB Method," *The Journal of Physical Chemistry A*, vol. 111, pp. 5678–5684, 2007.

[103] M. Gaus, A. Goez, and M. Elstner, "Parametrization and benchmark of dftb3 for organic molecules," *Journal of Chemical Theory and Computation*, vol. 9, pp. 338–354, 2013.

[104] X. Lu, M. Gaus, M. Elstner, and Q. Cui, "Parametrization of dftb3/3ob for magnesium and zinc for chemical and biological applications," *The Journal of Physical Chemistry B*, vol. 119, pp. 1062–1082, 2015.

[105] W. Zhou and T. Yildirim, "Lattice dynamics of metal-organic frameworks: Neutron inelastic scattering and first-principles calculations," *Phys. Rev. B*, vol. 74, p. 180301, 2006.

[106] C.-S. Tsao, M.-S. Yu, T.-Y. Chung, H.-C. Wu, C.-Y. Wang, K.-S. Chang, and H.-L. Chen, "Characterization of pore structure in metal-organic framework by small-angle x-ray scattering," *Journal of the American Chemical Society*, vol. 129, pp. 15997–16004, 2007.

[107] L. R. Redfern and O. K. Farha, "Mechanical properties of metal–organic frameworks," *Chemical Science*, vol. 10, pp. 10666–10679, 2019.

[108] M. Andrzejewski, N. Casati, and A. Katrusiak, "Reversible pressure pre-amorphization of a piezochromic metal–organic framework," *Dalton Transactions*, vol. 46, pp. 14795–14803, 2017.

[109] J. Krumhansl and R. Gooding, "Structural phase transitions with little phonon softening and first-order character," *Physical Review B*, vol. 39, p. 3047, 1989.

[110] F. De Wette, "On the theory of transitions in some molecular crystals ii," *Physica*, vol. 22, pp. 644–646, 1956.

[111] J. W. Richardson, D. L. Price, and M.-L. Saboungi, "Crystal symmetry lowering at an order-disorder transition," *Physical review letters*, vol. 76, p. 1852, 1996.

[112] R. E. Morris and P. S. Wheatley, "Gas storage in nanoporous materials," *Angewandte Chemie International Edition*, vol. 47, pp. 4966–4981, 2008.

[113] J.-R. Li, R. J. Kuppler, and H.-C. Zhou, "Selective gas adsorption and separation in metal–organic frameworks," *Chemical Society Reviews*, vol. 38, pp. 1477–1504, 2009.

[114] J. Lee, O. K. Farha, J. Roberts, K. A. Scheidt, S. T. Nguyen, and J. T. Hupp, "Metal–organic framework materials as catalysts," *Chemical Society Reviews*, vol. 38, pp. 1450–1459, 2009.

[115] R. C. Huxford, J. Della Rocca, and W. Lin, "Metal–organic frameworks as potential drug carriers," *Current opinion in chemical biology*, vol. 14, pp. 262–268, 2010.

[116] J. C. Tan, T. D. Bennett, and A. K. Cheetham, "Chemical structure, network topology, and porosity effects on the mechanical properties of zeolitic imidazolate frameworks," *Proceedings of the National Academy of Sciences*, vol. 107, pp. 9938–9943, 2010.

[117] S. Yuan, L. Feng, K. Wang, J. Pang, M. Bosch, C. Lollar, Y. Sun, J. Qin, X. Yang, P. Zhang, *et al.*, "Stable metal–organic frameworks: design, synthesis, and applications," *Advanced Materials*, vol. 30, p. 1704303, 2018.

[118] N. C. Burtch, J. Heinen, T. D. Bennett, D. Dubbeldam, and M. D. Allendorf, "Mechanical properties in metal–organic frameworks: emerging opportunities and challenges for device functionality and technological applications," *Advanced materials*, vol. 30, p. 1704124, 2018.

[119] T. D. Bennett, P. Simoncic, S. A. Moggach, F. Gozzo, P. Macchi, D. A. Keen, J.-C. Tan, and A. K. Cheetham, "Reversible pressure-induced amorphization of a zeolitic imidazolate framework (zif-4)," *Chemical communications*, vol. 47, pp. 7983–7985, 2011.

[120] T. D. Bennett, T. K. Todorova, E. F. Baxter, D. G. Reid, C. Gervais, B. Bueken, B. Van de Voorde, D. De Vos, D. A. Keen, and C. Mellot-Draznieks, "Connecting defects and amorphization in uio-66 and mil-140 metal–organic frameworks: a combined experimental and computational study," *Physical Chemistry Chemical Physics*, vol. 18, pp. 2192–2201, 2016.

[121] Y. Hu, H. Kazemian, S. Rohani, Y. Huang, and Y. Song, "In situ high pressure study of zif-8 by ftir spectroscopy," *Chemical communications*, vol. 47, pp. 12694–12696, 2011.

[122] S. Henke, M. T. Wharmby, G. Kieslich, I. Hante, A. Schneemann, Y. Wu, D. Daisenberger, and A. K. Cheetham, "Pore closure in zeolitic imidazolate frameworks under mechanical pressure," *Chemical science*, vol. 9, pp. 1654–1660, 2018.

[123] T. D. Bennett, A. L. Goodwin, M. T. Dove, D. A. Keen, M. G. Tucker, E. R. Barney, A. K. Soper, E. G. Bithell, J.-C. Tan, and A. K. Cheetham, "Structure and properties of an amorphous metal-organic framework," *Physical review letters*, vol. 104, p. 115503, 2010.

[124] T. D. Bennett and A. K. Cheetham, "Amorphous metal–organic frameworks," *Accounts of chemical research*, vol. 47, pp. 1555–1562, 2014.

[125] E. C. Spencer, R. J. Angel, N. L. Ross, B. E. Hanson, and J. A. Howard, "Pressure-induced cooperative bond rearrangement in a zinc imidazolate framework: A high-pressure single-crystal x-ray diffraction study," *Journal of the American Chemical Society*, vol. 131, pp. 4022–4026, 2009.

[126] J. Maul, M. R. Ryder, M. T. Ruggiero, and A. Erba, "Pressure-driven mechanical anisotropy and destabilization in zeolitic imidazolate frameworks," *Physical Review B*, vol. 99, p. 014102, 2019.

[127] M. Erkartal and M. Durandurdu, "Pressure-induced amorphization, mechanical and electronic properties of zeolitic imidazolate framework (zif-8)," *Materials Chemistry and Physics*, vol. 240, p. 122222, 2020.

[128] W. Depmeier, "The sodalite family–a simple but versatile framework structure," *Reviews in mineralogy and geochemistry*, vol. 57, pp. 203–240, 2005.

[129] M. Gaus, A. Goez, and M. Elstner, "Parametrization and benchmark of dftb3 for organic molecules," *Journal of Chemical Theory and Computation*, vol. 9, no. 1, pp. 338–354, 2013.

[130] X. Lu, M. Gaus, M. Elstner, and Q. Cui, "Parametrization of dftb3/3ob for magnesium and zinc for chemical and biological applications," *The Journal of Physical Chemistry B*, vol. 119, no. 3, pp. 1062–1082, 2015.

[131] A. K. Rappe, C. J. Casewit, K. S. Colwell, W. A. Goddard, and W. M. Skiff, "Uff, a full periodic table force field for molecular mechanics and molecular dynamics simulations," *Journal of the American Chemical Society*, vol. 114, pp. 10024–10035, 1992.

[132] J. C. Tan and A. K. Cheetham, "Mechanical properties of hybrid inorganic–organic framework materials: establishing fundamental

structure–property relationships," *Chemical Society Reviews*, vol. 40, pp. 1059–1080, 2011.

[133] Z. Abiza, M. Destrade, and R. W. Ogden, "Large acoustoelastic effect," *Wave Motion*, vol. 49, pp. 364–374, 2012.

[134] A. V. Osetrov, H.-J. Fröhlich, R. Koch, and E. Chilla, "Acoustoelastic effect in anisotropic layered structures," *Phys. Rev. B*, vol. 62, pp. 13963–13969, 2000.

[135] C. L. Nogueira, "Ultrasonic evaluation of acoustoelastic parameters in aluminum," *Journal of Materials in Civil Engineering*, vol. 29, p. 04017158, 2017.

[136] B. Zheng, Y. Zhu, F. Fu, L. L. Wang, J. Wang, and H. Du, "Theoretical prediction of the mechanical properties of zeolitic imidazolate frameworks (zifs)," *RSC advances*, vol. 7, pp. 41499–41503, 2017.

[137] N. Ogiwara, D. I. Kolokolov, M. Donoshita, H. Kobayashi, S. Horike, A. G. Stepanov, and H. Kitagawa, "The effect of amorphization on the molecular motion of the 2-methylimidazolate linkers in zif-8," *Chemical Communications*, vol. 55, pp. 5906–5909, 2019.

[138] C. P. Goodrich, A. J. Liu, and S. R. Nagel, "Solids between the mechanical extremes of order and disorder," *Nature Physics*, vol. 10, pp. 578–581, 2014.

[139] Z. Zhang, P. J. Yunker, P. Habdas, and A. G. Yodh, "Cooperative rearrangement regions and dynamical heterogeneities in colloidal glasses with attractive versus repulsive interactions," *Phys. Rev. Lett.*, vol. 107, p. 208303, 2011.

[140] W. A. Phillips and A. Anderson, *Amorphous solids: low-temperature properties*, vol. 24. Springer, 1981.

[141] A. J. Liu and S. R. Nagel, "The jamming transition and the marginally jammed solid," *Annual Review of Condensed Matter Physics*, vol. 1, pp. 347–369, 2010.

[142] R. Krishnan, "The scattering of light in fused quartz and its Raman spectrum," in *Proceedings of the Indian Academy of Sciences-Section A*, vol. 37, pp. 377–384, Springer, 1953.

[143] S. N. Taraskin, Y. L. Loh, G. Natarajan, and S. R. Elliott, "Origin of the Boson peak in systems with lattice disorder," *Phys. Rev. Lett.*, vol. 86, pp. 1255–1258, 2001.

[144] T. Brink, L. Koch, and K. Albe, "Structural origins of the boson peak in metals: From high-entropy alloys to metallic glasses," *Phys. Rev. B*, vol. 94, p. 224203, 2016.

[145] M. A. Ramos, S. Vieira, F. J. Bermejo, J. Dawidowski, H. E. Fischer, H. Schober, M. A. González, C. K. Loong, and D. L. Price, "Quantitative assessment of the effects of orientational and positional disorder on glassy dynamics," *Phys. Rev. Lett.*, vol. 78, pp. 82–85, 1997.

[146] J. Yang, Y.-J. Wang, E. Ma, A. Zaccone, L. H. Dai, and M. Q. Jiang, "Structural parameter of orientational order to predict the Boson vibrational anomaly in glasses," *Phys. Rev. Lett.*, vol. 122, p. 015501, 2019.

[147] U. Buchenau, N. Nücker, and A. J. Dianoux, "Neutron scattering study of the low-frequency vibrations in vitreous silica," *Phys. Rev. Lett.*, vol. 53, pp. 2316–2319, 1984.

[148] G. N. Greaves, F. Meneau, O. Majérus, D. G. Jones, and J. Taylor, "Identifying vibrations that destabilize crystals and characterize the glassy state," *Science*, vol. 308, pp. 1299–1302, 2005.

[149] M. T. Dove, M. J. Harris, A. C. Hannon, J. M. Parker, I. P. Swainson, and M. Gambhir, "Floppy modes in crystalline and amorphous silicates," *Phys. Rev. Lett.*, vol. 78, pp. 1070–1073, 1997.

[150] H. Shintani and H. Tanaka, "Universal link between the boson peak and transverse phonons in glass," *Nature Materials*, vol. 7, pp. 870–877, 2008.

[151] V. L. Gurevich, D. A. Parshin, and H. R. Schober, "Anharmonicity, vibrational instability, and the boson peak in glasses," *Phys. Rev. B*, vol. 67, p. 094203, 2003.

[152] U. Buchenau, M. Prager, N. Nücker, A. Dianoux, N. Ahmad, and W. Phillips, "Low-frequency modes in vitreous silica," *Physical Review B*, vol. 34, p. 5665, 1986.

[153] P. J. Lu and D. A. Weitz, "Colloidal particles: Crystals, glasses, and gels," *Annual Review of Condensed Matter Physics*, vol. 4, pp. 217–233, 2013.

[154] L. Van Hove, "The occurrence of singularities in the elastic frequency distribution of a crystal," *Phys. Rev.*, vol. 89, pp. 1189–1193, 1953.

[155] A. I. Chumakov, G. Monaco, A. Fontana, A. Bosak, R. P. Hermann, D. Bessas, B. Wehinger, W. A. Crichton, M. Krisch, R. Rüffer, G. Baldi, G. Carini Jr., G. Carini, G. D'Angelo, E. Gilioli, G. Tripodo, M. Zanatta, B. Winkler, V. Milman, K. Refson, M. T. Dove, N. Dubrovinskaia, L. Dubrovinsky, R. Keding, and Y. Z. Yue, "Role of disorder in the thermodynamics and atomic dynamics of glasses," *Phys. Rev. Lett.*, vol. 112, p. 025502, 2014.

[156] M. Baggioli and A. Zaccone, "Universal origin of boson peak vibrational anomalies in ordered crystals and in amorphous materials," *Phys. Rev. Lett.*, vol. 122, p. 145501, 2019.

[157] R. Milkus and A. Zaccone, "Local inversion-symmetry breaking controls the boson peak in glasses and crystals," *Phys. Rev. B*, vol. 93, p. 094204, 2016.

[158] E. Rat, M. Foret, E. Courtens, R. Vacher, and M. Arai, "Observation of the crossover to strong scattering of acoustic phonons in densified silica," *Phys. Rev. Lett.*, vol. 83, pp. 1355–1358, 1999.

[159] R. Shuker and R. W. Gammon, "Raman-scattering selection-rule breaking and the density of states in amorphous materials," *Phys. Rev. Lett.*, vol. 25, pp. 222–225, 1970.

[160] P. Giannozzi, S. Baroni, N. Bonini, M. Calandra, R. Car, C. Cavazzoni, D. Ceresoli, G. L. Chiarotti, M. Cococcioni, I. Dabo, *et al.*, "Quantum espresso: a modular and open-source software project for quantum simulations of materials," *Journal of physics: Condensed matter*, vol. 21, p. 395502, 2009.

[161] J. P. Perdew, K. Burke, and M. Ernzerhof, "Generalized gradient approximation made simple," *Phys. Rev. Lett.*, vol. 77, pp. 3865–3868, 1996.

[162] R. Pathria and P. D. Beale, *Statistical mechanics*, vol. 2. 1996.

[163] T. Besara, P. Jain, N. S. Dalal, P. L. Kuhns, A. P. Reyes, H. W. Kroto, and A. K. Cheetham, "Mechanism of the order–disorder phase transition, and glassy behavior in the metal-organic framework [(ch3)2nh2]zn(hcoo)3," *Proceedings of the National Academy of Sciences*, vol. 108, pp. 6828–6832, 2011.

[164] F. Kloutse, R. Zacharia, D. Cossement, and R. Chahine, "Specific heat capacities of mof-5, cu-btc, fe-btc, mof-177 and mil-53 (al) over wide temperature ranges: Measurements and application of empirical group contribution method," *Microporous and Mesoporous Materials*, vol. 217, pp. 1 – 5, 2015.

[165] T. Nakayama, "Microscopic buckling as an origin of the boson peak in network glasses," *Physica B: Condensed Matter*, vol. 316-317, pp. 497 – 499, 2002.

[166] A. Jeżowski, M. A. Strzhemechny, A. I. Krivchikov, N. A. Davydova, D. Szewczyk, S. G. Stepanian, L. M. Buravtseva, and O. O. Romantsova, "Glassy anomalies in the heat capacity of an ordered 2-bromobenzophenone single crystal," *Phys. Rev. B*, vol. 97, p. 201201, 2018.

[167] D. Engberg, A. Wischnewski, U. Buchenau, L. Börjesson, A. Dianoux, A. Sokolov, and L. Torell, "Origin of the boson peak in a network glass b 2 o 3," *Physical Review B*, vol. 59, p. 4053, 1999.

[168] A. Wisitsorasak and P. G. Wolynes, "Dynamical theory of shear bands in structural glasses," *Proceedings of the National Academy of Sciences*, vol. 114, pp. 1287–1292, 2017.

[169] H. Hofmeister, "Fivefold twinned nanoparticles," in *Encyclopedia of nanoscience and nanotechnology*, vol. 3, pp. 431–452, American Scientific Publishers Stevenson Ranch, 2004.

[170] K. Kwon, K. Y. Lee, Y. W. Lee, M. Kim, J. Heo, S. J. Ahn, and S. W. Han, "Controlled synthesis of icosahedral gold nanoparticles and their surface-enhanced raman scattering property," *The Journal of Physical Chemistry C*, vol. 111, pp. 1161–1165, 2007.

[171] W. Niu, W. Zhang, S. Firdoz, and X. Lu, "Dodecahedral gold nanocrystals: the missing platonic shape," *Journal of the American Chemical Society*, vol. 136, pp. 3010–3012, 2014.

[172] Y. Wang, D. Wan, S. Xie, X. Xia, C. Z. Huang, and Y. Xia, "Synthesis of silver octahedra with controlled sizes and optical properties via seed-mediated growth," *ACS nano*, vol. 7, pp. 4586–4594, 2013.

[173] Y. Zhou and K. A. Fichthorn, "Internal stress-induced orthorhombic phase in 5-fold-twinned noble metal nanowires," *The Journal of Physical Chemistry C*, vol. 118, pp. 18746–18755, 2014.

[174] V. Gryaznov, J. Heydenreich, A. Kaprelov, S. A. Nepijko, A. Romanov, and J. Urban, "Pentagonal symmetry and disclinations in small particles," *Crystal Research and Technology: Journal of Experimental and Industrial Crystallography*, vol. 34, pp. 1091–1119, 1999.

[175] B. Bagley, "A dense packing of hard spheres with five-fold symmetry," *Nature*, vol. 208, pp. 674–675, 1965.

[176] J. Diao, K. Gall, and M. L. Dunn, "Surface-stress-induced phase transformation in metal nanowires," *Nature materials*, vol. 2, no. 10, pp. 656–660, 2003.

[177] G. Mettela, R. Boya, D. Singh, G. P. Kumar, and G. Kulkarni, "Highly tapered pentagonal bipyramidal au microcrystals with high index faceted corrugation: Synthesis and optical properties," *Scientific reports*, vol. 3, pp. 1–8, 2013.

[178] J. P. Perdew and A. Zunger, "Self-interaction correction to density-functional approximations for many-electron systems," *Phys. Rev. B*, vol. 23, pp. 5048–5079, 1981.

[179] P. E. Blöchl, "Projector augmented-wave method," *Phys. Rev. B*, vol. 50, pp. 17953–17979, 1994.

[180] P. Söderlind, O. Eriksson, J. M. Wills, and A. M. Boring, "Theory of elastic constants of cubic transition metals and alloys," *Phys. Rev. B*, vol. 48, pp. 5844–5851, 1993.

[181] J. Morris Jr and C. Krenn, "The internal stability of an elastic solid," *Philosophical Magazine A*, vol. 80, pp. 2827–2840, 2000.

[182] C. Sow, A. Sarma, A. Schropp, D. Dzhigaev, T. F. Keller, C. G. Schroer, M. K. Sanyal, and G. U. Kulkarni, "Unraveling the spatial distribution of catalytic non-cubic au phases in a bipyramidal microcrystallite by x-ray diffraction microscopy," *ACS Nano*, vol. 14, 2020.

[183] G. Mettela, M. Bhogra, U. V. Waghmare, and G. U. Kulkarni, "Ambient stable tetragonal and orthorhombic phases in penta-twinned bipyramidal au microcrystals," *Journal of the American Chemical Society*, vol. 137, pp. 3024–3030, 2015.

[184] H. M. Rosenberg, "The thermal conductivity of metals at low temperatures," *Philosophical Transactions of the Royal Society of London. Series A, Mathematical and Physical Sciences*, vol. 247, pp. 441–497, 1955.

[185] X. Zhou, L. Li, H. Dong, A. Giri, P. E. Hopkins, and O. V. Prezhdo, "Temperature dependence of electronphonon interactions in gold films rationalized by time-domain ab initio analysis," *The Journal of Physical Chemistry C*, vol. 121, pp. 17488–17497, 2017.

[186] V. Vishnyakov, S. E. Donnelly, and G. Carter, "Scanning tunnelling microscopy observations of the evolution of small-scale topography on gold surfaces following irradiation with low-energy argon ions," *Philosophical Magazine B*, vol. 70, pp. 151–157, 1994.

[187] W. Huang, W. Qian, M. A. El-Sayed, Y. Ding, and Z. L. Wang, "Effect of the lattice crystallinity on the electron- phonon relaxation rates in gold nanoparticles," *The Journal of Physical Chemistry C*, vol. 111, no. 29, pp. 10751–10757, 2007.

[188] K. Nordlund, M. Ghaly, R. Averback, M. Caturla, T. D. de La Rubia, and J. Tarus, "Defect production in collision cascades in elemental semiconductors and fcc metals," *Physical Review B*, vol. 57, p. 7556, 1998.

[189] T. Qiu and C. Tien, "Short-pulse laser heating on metals," *International Journal of Heat and Mass Transfer*, vol. 35, pp. 719–726, 1992.

[190] M. N. Ozisik and D. Y. Tzou, "On the Wave Theory in Heat Conduction," *Journal of Heat Transfer*, vol. 116, pp. 526–535, 1994.

[191] D. D. Kulkarni, D. A. Field, D. B. Cutshall, J. E. Harriss, W. R. Harrell, and C. E. Sosolik, "Probing kinetically excited hot electrons using schottky diodes," *Journal of Vacuum Science & Technology B*, vol. 35, p. 03D103, 2017.

[192] T. Q. Qiu and C. L. Tien, "Heat Transfer Mechanisms During Short-Pulse Laser Heating of Metals," *Journal of Heat Transfer*, vol. 115, pp. 835–841, 1993.

[193] S. Brorson, J. Fujimoto, and E. Ippen, "Femtosecond electronic heat-transport dynamics in thin gold films," *Physical Review Letters*, vol. 59, p. 1962, 1987.

[194] D. Duffy, S. Khakshouri, and A. Rutherford, "Electronic effects in radiation damage simulations," *Nuclear Instruments and Methods in Physics Research Section B: Beam Interactions with Materials and Atoms*, vol. 267, pp. 3050 – 3054, 2009.

[195] K. Baumeister and T. Hamill, "Hyperbolic heat-conduction equationa solution for the semi-infinite body problem," *Journal of Heat Transfer*, vol. 91, pp. 543–548, 1969.

[196] D. Gall, "Electron mean free path in elemental metals," *Journal of Applied Physics*, vol. 119, p. 085101, 2016.

[197] J. Li, Y. Gu, and Z. Guo, "Decreasing the core loss of grain-oriented silicon steel by laser processing," *Journal of Materials Processing Technology*, vol. 69, pp. 180 – 185, 1997.

[198] N. D. Mermin, "Thermal properties of the inhomogeneous electron gas," *Physical Review*, vol. 137, p. A1441, 1965.

[199] J. Hohlfeld, S.-S. Wellershoff, J. Güdde, U. Conrad, V. Jähnke, and E. Matthias, "Electron and lattice dynamics following optical excitation of metals," *Chemical Physics*, vol. 251, pp. 237–258, 2000.

[200] N. Del Fatti, C. Voisin, M. Achermann, S. Tzortzakis, D. Christofilos, and F. Vallée, "Nonequilibrium electron dynamics in noble metals," *Phys. Rev. B*, vol. 61, pp. 16956–16966, 2000.

[201] A. Stoneham, "Energy transfer between electrons and ions in collision cascades in solids," *Nuclear Instruments and Methods in Physics Research Section B: Beam Interactions with Materials and Atoms*, vol. 48, pp. 389–398, 1990.

[202] Z. Lin, L. V. Zhigilei, and V. Celli, "Electron-phonon coupling and electron heat capacity of metals under conditions of strong electron-phonon nonequilibrium," *Physical Review B*, vol. 77, p. 075133, 2008.